Drift Ratchets as Biomimetic Filters

James William Herringer

School of Engineering

RMIT University

A thesis submitted in fulfilment of the requirements for the degree of

Doctor of Philosophy

College of Science, Engineering and Health

October 2017

I would like to dedicate this thesis to my loving family.

Declaration

I certify that except where due acknowledgement has been made, the work is that of the author alone; the work has not been submitted previously, in whole or in part, to qualify for any other academic award; the content of the thesis is the result of work which has been carried out since the official commencement date of the approved research program; any editorial work, paid or unpaid, carried out by a third party is acknowledged; and, ethics procedures and guidelines have been followed. I acknowledge the support I have received for my research through the provision of an Australian Government Research Training Program Scholarship.

James William Herringer
October 2017

Acknowledgements

While a PhD is a lonely road one chooses to wander, there is a solid network of supporters ensuring you have everything you need to finish!
Firstly, I would like to acknowledge the endless support and critical advice from my supervisors, Prof. Gary Rosengarten, Prof. Jim Mitchell, Dr Daniel Lester and Dr Graham Dorrington. Thank you for your encouragement, leadership and patience. Particularly Prof. Rosengarten for the enthusiasm to help me whenever required.
I would like to extend a big thank you to Dr Vijay Sivan for his tireless work in training me and helping me in the cleanroom fabricating the microfluidic chips. Your dedication and unwavering help was much appreciated.
A big thank you to Dr Cameron Stanley and Dr Ahmad Mojiri as well as all of Prof. Rosengarten's PhD students. Thank you for all your help and allowing me to vent whenever needed.
I would like to thank my Dad for always supporting me and my endeavours. You have always encouraged me to do my best and following my dreams.
I would like to say a special thank you to my Mum and sister for their unconditional love and support. Both of you have motivated me through this time in my life and have been role models for me to develop myself as an individual. I appreciate the sacrifices you have made to allow me to follow my aspirations and will always love you.
Finally, I would like to say thank you to Megan. You have supported me throughout my PhD and I can't thank you enough for encouraging me through this process. You have been there through the ups and downs and you are someone who I look up to for inspiration and motivation. I can't wait to start the next chapter of our lives together... after our PhDs!
I know I will always have you guys to call on when times are tough and could not have done it without you...

Abstract

Diatoms are microscopic, phototrophic, unicellular algae encased in a porous, rigid, siliceous, cell wall known as a frustule and they inhabit the euphotic zones in bodies of seawater and freshwater globally. It is not yet fully understood how diatoms compete with swimming microorganisms for nutrients in their environment. It is believed that the frustule does play a role in giving them a competitive advantage, however, the function of the diatoms' frustule is not yet fully understood. Among other functions it has been proposed that the frustule acts like a filter for the diatom, sorting nutrients from harmful entities such as pathogens, poisons, colloids and pollutants, from their natural environment. As a result of the micro- and nanoscopic nature of the frustule and its features, diffusion is thought to play an important role in the frustules filtering capabilities. It has been proposed that specific centric species of diatom employ the drift ratchet mechanism to sort and control mass transport towards and away from the diatom cell. This research has determined that this is unlikely due to the size and configuration of the diatom girdle band pores. Instead, a new theory is presented herein, termed "Hydrodynamic Immunity", in which diatoms use diffusiophoresis to separate nutrients from harmful entities. In conjunction with this work the dimensionless numbers critical for dynamic similarity analysis of a drift ratchet are determined to allow for easy comparison between dynamically similar experiments. Finally, a novel hydrodynamic drift ratchet microfluidic device was designed and fabricated as a proof-of-concept to prove definitively whether the drift ratchet mechanism can be generated in an experimental environment, following inconclusive findings from past research experiments. This remains unresolved due to experimental complications; however improvements are suggested to ensure future work is successful at recreating a drift ratchet in experiments.

Publications

- Herringer, J. W., Lester, D. R., Dorrington, G. E., Rosengarten, G. and Mitchell, J. G. (2017), Hydrodynamic drift ratchet scalability. AIChE J., 63: 2358–2366. doi:10.1002/aic.15569 (Submitted / Accepted) (Refers to Chapter 3 in this thesis)
- Rosengarten, G. & Herringer, J. (2017) Fluid Interactions of Diatoms. In Diatom Nanotechnology (ed. D. Losic), The Royal Society of Chemistry. (Submitted / Accepted – to be published) (Refers to Chapter 2 in this thesis)
- Herringer, J.W., Lester, D.R., Dorrington, G.E., Rosengarten, G. & Mitchell, J.G. (2017), Diatom pores as particle separators. Journal of the Royal Society Interface. (Soon to be submitted) (Refers to Chapter 4 in this thesis)

Table of contents

List of figures

List of tables

Chapter 1

Introduction

Particle separation is an intrinsic process in a myriad of industries and applications. These industries include; environment (Chen et al. (2014); Ngomsik et al. (2005)), water purification (Balasubramanian et al. (2007); Jimenez and Bridle (2015); Jimenez et al. (2017)), cosmetics (Chen et al. (2014); Zarzar et al. (2015)), food production (Grenvall et al. (2008)), biomedical (Jubery et al. (2014); Khashan et al. (2017)), chemical synthesis (Zhang et al. (2013)) and mineral processing (Bhardwaj et al. (2011); CHEN et al. (2010)). The breadth of these industries highlights the importance of nano- / microparticle separation and control. Moreover, the world market for separation devices is estimated at over $50 billion annually (MRS, Research 2016). These particle separation techniques are usually bundled into a platform called a microfluidic device. The focus of this research is to look at improving the efficiency and performance of microfluidic devices used to separate nanoparticles / microparticles. Generally, separation techniques take advantage of a specific property of the nano- / microparticles being processed. As such, the techniques employed to achieve separation of nano- / microparticles can be split into two categories; sieving and force-based separation. The former exploits the size difference between individual microparticles, whereas the latter uses other properties i.e. magnetic susceptibility, electric charge, density etc. to ensure separation. These categories can be further divided into continuous or processed in steps that are discrete.

Size exclusion particle separation involves filters with a critical pore size which excludes above a critical size. Filtration techniques consist of either cross-flow or dead-end filtration which describe the flow of the particle-fluid mixture relative to the filter membrane, illustrated in Figure 1.1. These techniques are often associated with membrane fouling and require large pressures to push the particle-fluid mixture through the porous membrane (Sajeesh and Sen (2014); Salafi et al. (2017)).

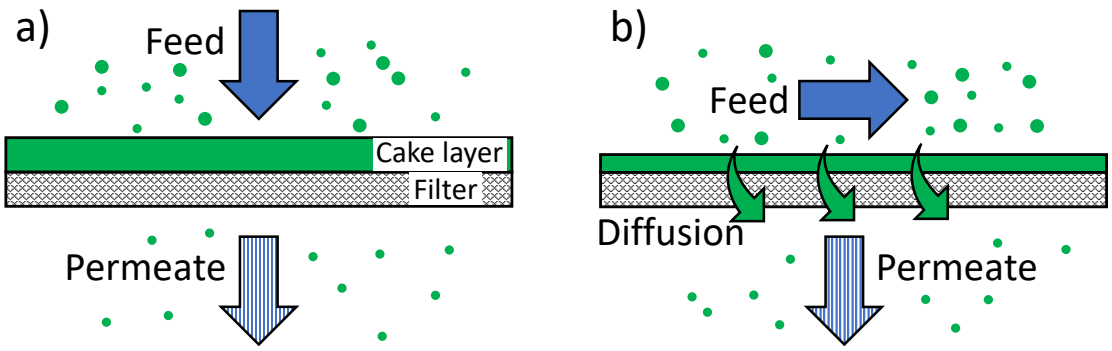

Figure 1.1 Schematic diagram of a) Dead-end filtration and b) Cross-flow filtration.

The remaining forced-based separation methods use the unique response of microparticles to specific forces such as hydrodynamic, electrokinetic and magnetic forces to separate them from fluid systems (Çetin et al. (2014); Sajeesh and Sen (2014); Salafi et al. (2017)). The various techniques developed over the years include; electrophoresis / dielectrophoresis (Cheri et al. (2014); Choi et al. (2009); Iranifam (2013); Jubery et al. (2014); Jung and Kwak (2007); Salafi et al. (2017); Zhang et al. (2010)), magnetophoresis (Çetin et al. (2014); Khashan et al. (2017); Liu et al. (2009); Ngomsik et al. (2005); Salafi et al. (2017)), centrifuge (Salafi et al. (2017)), inertial effects (Jimenez et al. (2017); Nam et al. (2012); Sajeesh and Sen (2014); Salafi et al. (2017)), deterministic lateral displacement (Çetin et al. (2014); Sajeesh and Sen (2014)), acoustophoresis (Çetin et al. (2014)), flow-field fractionation (Sajeesh and Sen (2014); Salafi et al. (2017)), and gravity assisted separation (Nejad et al. (2015)). These systems generally suffer from inefficiencies and separation performance issues such as microparticle selectivity, throughput and control. Additionally, the driving forces associated with separation techniques based on external fields such as magnetic and electrical fields tend to vary linearly with particle volume. Therefore, as we try to respond to the growing requirement to separate smaller nanoparticles, these conventional approaches become less effective. The difficulty to separate smaller particles using external forces is compounded by random Brownian motion becoming increasingly dominant at smaller particle sizes.

There is a growing need to improve the performance and efficiency of these separation techniques whilst being able to incorporate separation of smaller nanoparticles. Some researchers are looking to nature to inspire a potential solution to improve separation techniques in a biomimetic way; learning from processes in nature to improve man-made nano- / microparticle separation devices. In particular, Losic et al. (2006), Yang et al. (2011), Rosengarten (2009), Losic et al. (2007a), Mitchell et al. (2013) and Losic et al. (2009) have highlighted a microscopic, single-celled, water based algae, known as a diatom as a

biomimetic case study. Diatoms are a class of phytoplankton that live in ocean and freshwater ecosystems globally. Intriguingly, they encase their cell inside a porous rigid shell known as a frustule. It is not yet fully understood how diatoms compete with swimming microorganisms for nutrients in their environment (Mitchell et al. (2013)). However, as the unique aspect of diatoms is their porous silica frustule, the aforementioned authors propose it could act as a filter. This would involve selectively transporting inorganic nutrients towards the cell, and possibly also of waste away from the cell, while preventing the uptake of harmful entities through the frustule such as pathogens, poisons and pollutants (Mitchell et al. (2013)).

To better understand the filtering capability of a diatom frustule, there is a need to accurately map its structure. Consequently, there have been many studies imaging diatom frustules micro- and nanoscopic features using Atomic Force Microscopy (AFM) (Losic et al. (2007a,b); Round et al. (1990)), Transmission Electron Microscopy (TEM) (Pascual García et al. (2014); Round et al. (1990); Yang et al. (2011)) and Scanning Electron Microscopy (SEM) (Hale and Mitchell (2001a); Losic et al. (2009, 2006); Pascual García et al. (2014); Round et al. (1990); Yang et al. (2011)). From these imaging studies, there have been two primary structures observed for a centric diatoms' frustule. It is composed of two halves (valves) which fit together analogous to a petri dish, with the girdle bands (the mid-sections) connecting the top and bottom valve, similar to the illustration in Figure 1.2 (Armbrust (2009); Yang et al. (2011)).

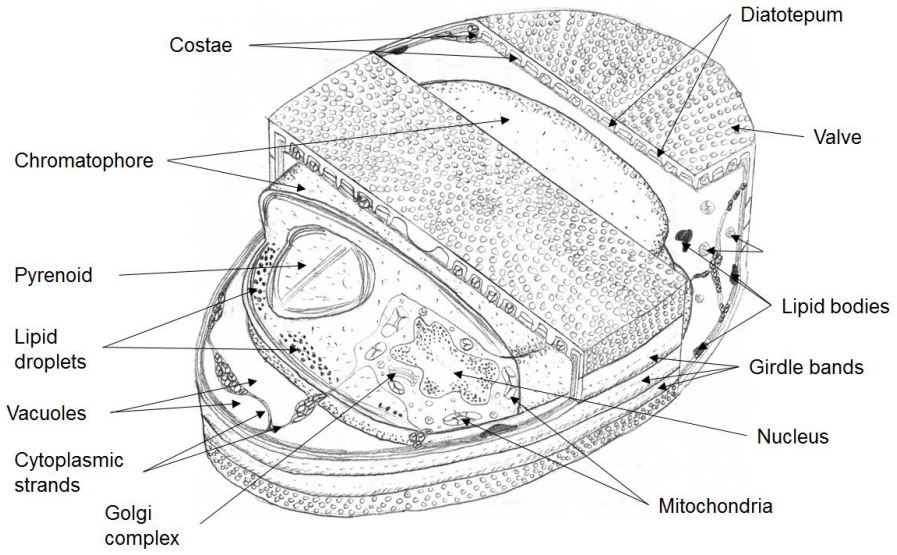

Figure 1.2 Schematic diagram of the cell structure of a generic centric diatom (Yang et al. (2011)). Reproduction from Yang et al. (2011) with permission from the Royal Society of Chemistry.

These two regions have distinct porosity and are characterised by differently shaped pores. What is driving these particular shaped pores and why the shape of the pores are different between the two regions is not understood.

In the girdle band specifically, Losic et al. (2009) identified geometric similarities between a drift ratchet pore investigated by Kettner et al. (2000) and Matthias and Muller (2003), and the pores of the girdle bands of the diatom *Coscinodiscus sp.*, shown in Figure 1.3.

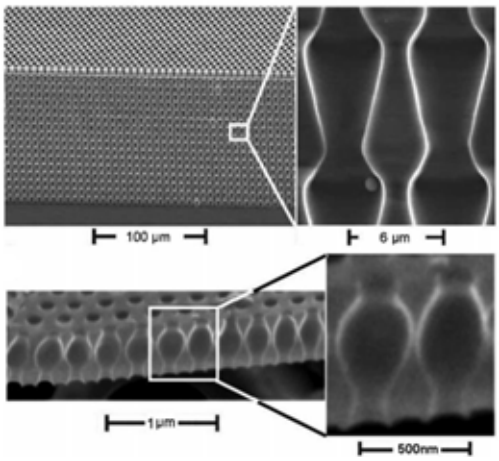

Figure 1.3 (Top) Scanning Electron Microscopy (SEM) micrograph of a massively parallel silica membrane with asymmetric drift ratchet pores (Matthias and Muller (2003)). (Bottom) SEM of girdle band pores of the diatom, *Coscinodiscus sp.* (Losic et al. (2009)). Losic D, Mitchell JG, Voelcker NH. Diatomaceous Lessons in Nanotechnology and Advanced Materials. Advanced Materials 2009;21:2947-58. Copyright Wiley-VCH Verlag GmbH & Co. KGaA. Reproduced with permission.

Drift ratcheting is a microfluidic phenomenon where microparticles drift unidirectionally along an asymmetrically repeating axisymmetric pore (Kettner et al. (2000); Matthias and Muller (2003)). The counter-intuitive nature of this drift is that the fluid that contains these microparticles is pumped sinusoidally through the pore structure, so there is no net displacement of the fluid through the pore (Kettner et al. (2000); Matthias and Muller (2003)). The direction and magnitude of microparticle drift are dependent on the amplitude and frequency of fluid pumping, and size and shape of both particles and pore wall (Kettner et al. (2000); Matthias and Muller (2003)). Therefore, different sized and shaped particles could effectively be driven in opposite directions at the same time through a drift ratchet pore improving selectivity and separation times. Furthermore, this separation mechanism is more suited to separation of nanoparticles because the hydrodynamic force scales linearly with particle radius.

Losic et al. (2009) suggested the drift ratchet mechanism is used by the diatom for either or both the selective transport of matter to and from the cell. If these diatoms employ the drift ratchet mechanism, this will be the first example of its kind in nature and will contribute to our understanding of how these microorganisms survive in their respective environment. Furthermore, there is the potential to use this knowledge to improve the performance and efficiency of man-made separation and sorting devices (Yang et al. (2011)). General issues associated with microfiltration such as; large back pressure, low flow rates, fouling due to the small pore sizes, and large volumes of pre-processed particle-fluid mixture required for processing could be minimised by using knowledge of how diatoms filter inorganic nutrients (Yang et al. (2011)). These improvements could start in microfluidic devices, with the possibility of expanding to macro-filtration systems. This leads to the main focus of this work, which is to assess whether the diatom girdle band pores have the ability to function as a drift ratchet. Although this work mainly focuses on whether the centric marine diatom species, *Coscinodiscus sp.*, employs the drift ratchet mechanism as a filtration technique, many aspects are transferable to freshwater settings and to pelagic pennate diatoms as well.

To address the core intention of this research, Chapter 2 delivers a comprehensive review of past mass transfer studies through diatom frustules. To narrow and simplify this study it will focus on centric marine species of diatom, however the capability exists to read across results or methods to other species of diatom in the future. Chapter 3 and 4 detail numerical simulations, leading with a discussion on the state of the art in the drift ratchet field in Chapter 3. A dynamic similarity study conducted on a drift ratchet to improve the ease in which drift ratchet experiments are designed is then explained.
Using a numerical model developed and demonstrated in the previous chapter, Chapter 4 presents evidence against the girdle band pores using the drift ratchet separation mechanism. Consequently the latter sections of this chapter do detail a proposal of a new theory on how diatoms filter, termed “Hydrodynamic Immunity”.
Finally, due to the lack of experimental results in the field of drift ratchets, determined from the literature review, the performance of a novel adaptation of a drift ratchet membrane is experimentally assessed in Chapter 5. This work is complimented by detailing a potential design for a microfluidic device using the drift ratchet mechanism to easily separate particles based on size.

Chapter 2

Critical Literature Review on Diatom Transport Processes

A diatoms' surrounding aquatic environment is responsible for providing them access to nutrients, dictating the movement of their cells and controlling the ability of the frustule to filter. As such, it is critical to understand the environment diatoms survive in as this has a significant effect on their uptake of inorganic nutrients. Accordingly, the following sections outline the natural hydrodynamic forces that diatoms experience, and the effect that these forces have on the distribution and supply of separated nutrients to the diatom in their environment, including self-imposed forces such as buoyancy changes to aid in sinking.

Diatoms are photosynthesising, microscopic, single-celled phytoplankton found in the upper layers of aquatic environments globally, at depths rich in nutrients and at which light penetrates (Armbrust (2009)). This layer of penetrating sunlight in the upper ocean is known as the euphotic zone and can reach depths of $100-200m$ (Martínez-García and Karl (2015)). The euphotic zone also overlaps the upper mixed layer, which is an oceanic layer characterised by intense mixing events such as turbulence as illustrated in Figure 2.1.
During the winter months, the depth of the upper mixed layer of the ocean increases to beyond the depth of the euphotic zone (Gregg (1973)). Upwelling, propagating planetary waves (Uz et al. (2001)) and turbulence (Armbrust (2009)) associated with this event recharges the upper ocean with nutrients from the deeper nutrient–rich waters. These winter months result in a low diatom population due to nutrient exhaustion and grazing from zooplankton from the previous bloom and the lack of available photosynthetically active radiation (PAR: $\lambda = 400-700nm$) to facilitate photosynthesis (Denman and Gargett (1995)). With the advent of higher air temperatures in spring and early summer comes stronger thermal stratification of the ocean which decreases the depth of the now nutrient charged mixed layer, bringing the diatoms to a shallower region in the euphotic zone where nutrients and light are abundant

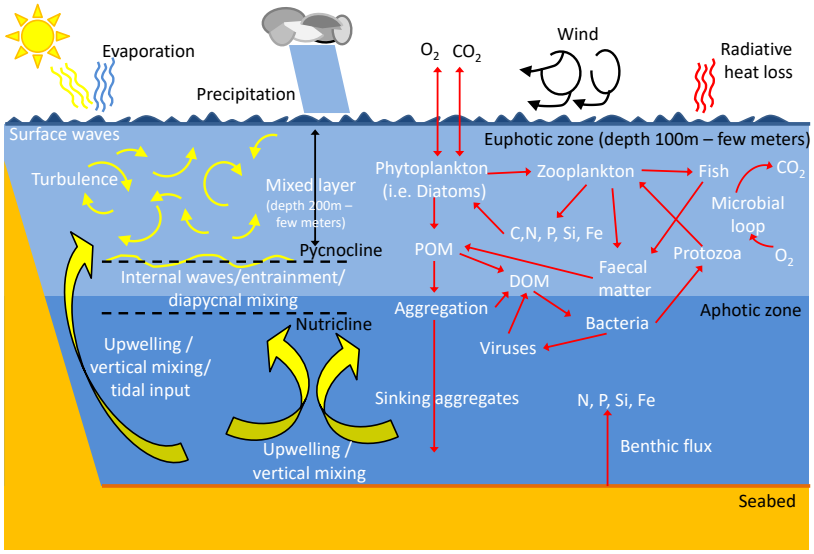

Figure 2.1 Schematic of the food web and geophysical forces the diatom experiences in its marine environment. Adapted from Ban et al. (1999), Azam and Malfatti (2007) and Cermeño et al. (2008).

(Alvain et al. (2008)). These favourable environmental conditions generate massive diatom population growth from a seemingly passive uptake of inorganic nutrients and trace elements from their surrounding aquatic environment (Mitchell et al. (2013)). Diatoms are considered passive eaters because they are a non-motile species of phytoplankton, having no active propulsion system. Instead, they rely on the motion of water to influence their movement in their environment, with some species also forming chains between individual cells and/or ballasting their cell to change their buoyancy within the water column for vertical migration. Intriguingly, the cell of a diatom is encased in a rigid, porous, transparent, glass shell – known as the frustule, illustrated in Figure 1.2 (Armbrust (2009); Round et al. (1990)). There are over 10 000 species of diatom based on their distinguishing frustule morphologies (Armbrust (2009); Kooistra et al. (2007); Schmid (1994)), ranging from a few micrometers to a few millimetres in size (Round et al. (1990)). They are classified as either centric (disk/cylindrical frustules – Figure 1.2) or pennate (elongated/folded frustules), and there are even annular and triangular shaped frustules (Round et al. (1990)). Besides the diatom frustule acting as a filter, there are many other proposed functions. Some of its wider accepted roles include: increasing or decreasing sinking rates through the water column (Fisher (1995); Raven and Waite (2004)); providing defence against predators, parasites and pathogens (Hamm (2005); Raven and Waite (2004)); providing an acid-base buffer site for the catalysis of carbonic anhydrase (Milligan and Morel (2002); Morant-Manceau et al. (2007)); protecting sensitive organelles against damage from UV-A and UV-B exposure and scattering photosynthetically

active radiation (PAR: $\lambda = 400 - 700nm$) (De Tommasi et al. (2008); Fuhrmann et al. (2004); Hsu et al. (2012); Ingalls et al. (2010); Losic et al. (2009); Noyes et al. (2008); Yamanaka et al. (2008)). Other less familiar proposed functions include: countering the turgor pressure generated by the cell (Schmid (1994)); helping to facilitate reproduction processes (Round et al. (1990)) and acting as a passive barrier, controlling, sorting and separating matter like a filter (Losic et al. (2009)), which will be the main role studied herein.

As previously mentioned, diatoms live in the euphotic zone of marine environments to facilitate energy production and cell growth via photosynthesis. Figure 2.2 illustrates the size exclusion filtering capacity of diatom frustules based on their pore size compared to other filtering techniques. Diatoms correspond to the ultra- / nanofiltration regimes in the realm of filtering bacteria, viruses and organic molecules while allowing ionic species to pass through.

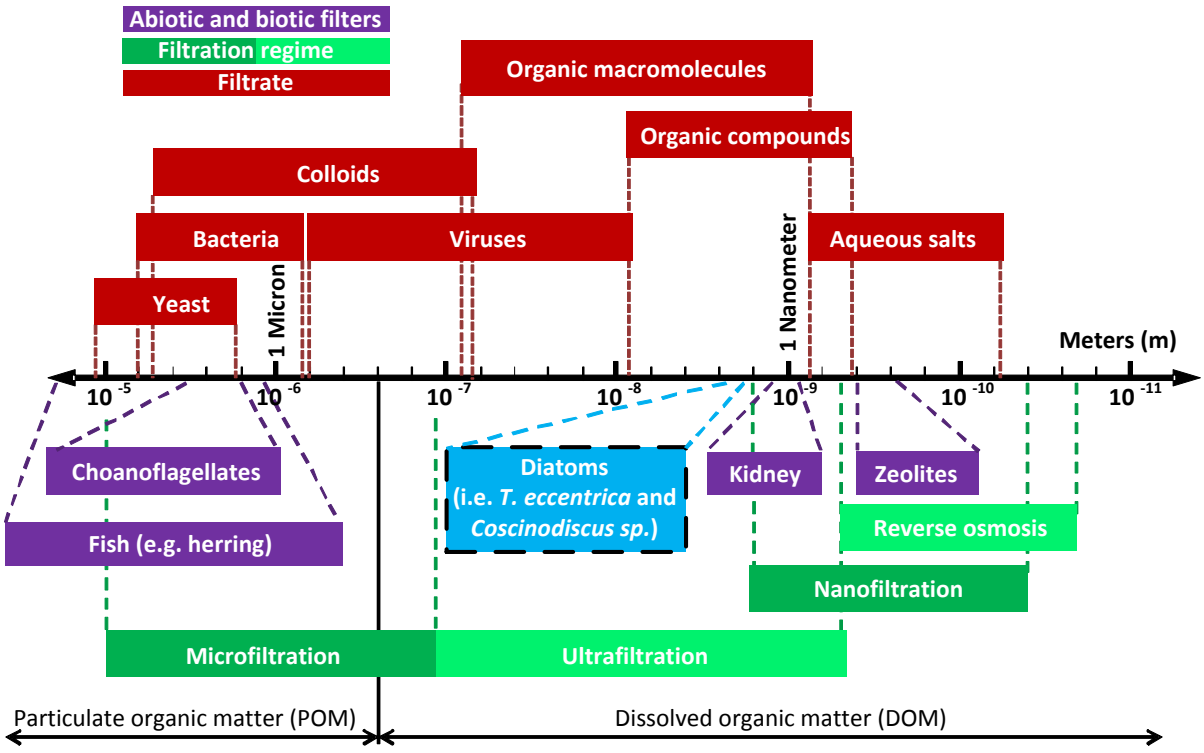

Figure 2.2 Size domain of filtrate (Red) and abiotic/biotic filters (Purple) of interest in the field of small-scale filtration (Green). The centric diatoms at the focus in this review are in the ultrafiltration regime. Adapted from Azam and Malfatti (2007); Brenner et al. (1978); Goodrich et al. (2000); Losic et al. (2006); Prakash et al. (2008); Yu et al. (2008).

179 They uptake and process inorganic nutrients and trace elements used for a variety of differing
180 cell functions, including;

181 • Fe^{3+} and Fe^{2+}: used for fixing nitrogen and maintenance of photosynthetic organelles
182 (Sunda and Huntaman (1997))

183 • H^{+}, Cl^{-}, K^{+} and Na^{+}: used to control ionic cell content and control transmembrane
184 pores (Taylor (2009))

185 • $NH_4{}^{+}$, $NO_3{}^{-}$ and $PO_4{}^{3-}$: used as inorganic nutrients in protoplasm growth (Boyd and
186 Gradmann (1999b); Round et al. (1990))

187 • $Si(OH)_4$: used to build the rigid silica frustule (Kamykowski and Zentara (1985);
188 Melkikh and Bessarab (2010); Wischmeyer et al. (2003))

189 • $HCO_3{}^{-}$ and pCO_2: used as a source of carbon dioxide in photosynthesis to produce
190 sugars, energy and oxygen (Tortell et al. (1997))

191 • Trace metals (Cu, Cd and Zn) for catalysing reactions (Morel et al. (1991)).

192 These chemical species are transported through the pores of the silica frustule, in dissolved
193 ionic form, before being taken up by the cell membrane (Hochella Jr. et al. (2008)). However,
194 the influence of the frustule in sorting, separating and controlling these chemical species
195 during the uptake and excretion of matter is not yet fully understood.

196 Transport of matter to the diatom cell can be broken down into three events; 1. Uptake
197 by the cell, 2. Transport through the frustule to the cell and 3. Transport to the outside
198 of the frustule from the free solution, which is their aquatic environment. The converse is
199 true for transmission of matter away from the cell. Transport of matter through the aquatic
200 environment towards the cell has been investigated simultaneously with cell uptake kinetics,
201 but without reference to the effect of the frustule on mass transfer. Transport of matter
202 through the frustule is the least understood out of the three and therefore will be the primary
203 area of focus in this investigation.

204 Section 2.1, provides a general overview of the physics associated with the transport of
205 matter in a dynamic ocean environment at the spatial scales of diatoms. Section 2.3 describes
206 the physical kinematic response of a diatom cell to this changing aquatic environment. While
207 Sections 2.2 and 2.4 delve into the transport of matter towards and across the cell membrane
208 of a diatom, as well as the effect of the frustule on this transport, respectively. Objectives and
209 research questions are then defined in Section 2.5 in preparation for the main body of work.

2.1 Transport of Matter in the Ocean

To begin to synthesise an understanding of how mass is transported through the pores of the frustule, an understanding of how chemical species are transferred and distributed through the ocean surrounding diatoms is needed. Samples, from the water column in the Eastern English Channel, were used to spatially measure nitrite, nitrate, phosphate and silicate concentrations (Mitchell et al. (2013)). These results confirm a heterogeneous distribution with the size of hotspots on the order of centimetres with significant concentration gradients, even for a turbulent marine environment such as the Eastern English Channel i.e. high dissipation rates, 5×10^{-7} to 5×10^{-4} $m^2 s^{-3}$ (Mitchell et al. (2013); Seuront (2005)). Measured chemical concentration values from various ocean locations are shown in Table A.1 in Appendix A.

The heterogeneous nature of nutrient distribution can be attributed to localised stirring, mixing, and nutrient replete/deplete activities i.e. local consumption and re-suspension of nutrients (Pasciak and Gavis (1974); Williams and Follows (2011)). If there is a nutrient "hotspot" within the turbulent region of the ocean, two transport phenomena will disperse this patch; diffusion and advection[1] (Stocker (2012); Williams and Follows (2011)). Advective transport will be from turbulence and mixing in the ocean. Long, thin filaments of nutrients begin to form as turbulence shears and elongates this matter. These filaments thin further from shearing, causing a larger concentration gradient between the filament and the ambient conditions, which then begins to promote the effects of diffusion even more (Stocker (2012)). Consequently, there exists a length scale, in a turbulent fluid environment, at which the transport due to diffusion and advection are equal, and this is the Batchelor length (Batchelor (1959)),

$$\eta_b = \left(\frac{\nu D_{fs}^2}{\varepsilon} \right)^{\frac{1}{4}} \tag{2.1}$$

where D_{fs} ($m^2 s^{-1}$), ε ($m^2 s^{-3}$) and ν ($m^2 s^{-2}$) are the free-space mass diffusion coefficient, kinetic energy dissipation rate and kinematic viscosity, respectively. The Batchelor length is typically $30 - 300 \mu m$ in the ocean (Stocker (2012)), which is comparable to the length scale of a diatom frustule. Below the Batchelor length diffusion takes transport dominance over advection. However, mass transport can be enhanced at these small scales by advection as further elucidated in Section 2.2.3.

The above section outlines how matter, like dissolved nutrients, behave in the ocean. Subsequent sections describe how the diatom cell physically interacts with this ever changing aquatic environment.

[1] Assuming that convection is the summation of advective and diffusive mechanisms in transporting matter.

2.2 Transport of Matter Towards and Across an Osmotroph Cell Membrane

This section, outlines the extensive progress made in understanding the diffusion of matter towards an osmotroph and its uptake kinetics. Initially, an imaginary case is considered in which a diatom has no frustule surrounding its cell to exaggerate the effect the frustule will have on the transport of matter towards a cell in later sections.

2.2.1 Diffusive Mass Transport and Cell Uptake for Osmotrophs

The total diffusive mass transport towards a spherical osmotroph is defined by the following expression,

$$Q_{Diff} = 4\pi D_{fs} r_0 (C_\infty - C_0) \tag{2.2}$$

where, C_0 ($\mu molL^{-1}$) and C_{inf} ($\mu molL^{-1}$) are the concentration of a solute at the surface of the cell and at ambient, respectively, r_0 (m) is the size of the cell and D_{fs} ($m^2 s^{-1}$) is the free space diffusion coefficient. From Equation 2.2, if there is no advection for a perfectly absorbing cell, i.e. $C_0 = 0$, the only ways to increase the diffusive flux are to increase the free-space diffusion coefficient, D_{fs} ($m^2 s^{-1}$), of the nutrients diffusing towards the cell, increase the size of the cell, r_0 (m), or increase the ambient nutrient concentration surrounding the cell, C_∞ ($\mu molL^{-1}$) (Jumars et al. (1993); Karp-Boss et al. (1996)). There are constraints which limit the benefit of changing these parameters to maximise this diffusive flux. As previously covered in Table A.1 there are nominal values for the ambient concentration and size of nutrients and trace elements in the oceans. Also, as the cell size increases the demand for nutrients increases at a greater rate compared to the diffusive flux. This dependency of metabolic rate on cell size can be predicted using allometric relations (Edwards et al. (2012); Marañón (2015); Marbà et al. (2007); Verdy et al. (2009)). The dependency of the metabolic rate (R) on the mass of the organism (M) often follows the following expression $R = aM^b$ (Jumars (1993)). A non-linear metabolic rate has been assumed to scale with cell size by r_0^a where $1 < a < 3$ (Jumars (1993); Kiørboe (2008)). Generally the values of a and b in the mass-specific metabolic rate equation $R^* = aM^b$ for diatoms are 0.48 and -0.13, respectively (Marañón (2015)). For organisms such as birds and mammals the exponent has the value -0.25 (Marañón (2015)).

The diffusive flux, uptake rate and metabolic rate must be matched for the cell to grow to its maximum size possible, represented in Figure 2.3 by point 1a and 1b. For a diffusion limited case where the uptake rate is dictated by the diffusion rate towards the cell, there

exists an optimal cell size where the difference between the uptake rate and the metabolic rate is a maximum and the cell is at its most energy efficient. This case is represented by point 2a and 2b in Figure 2.3.

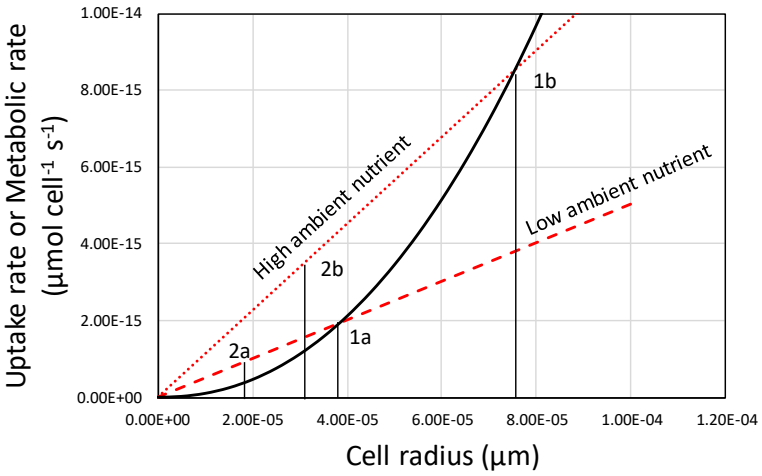

Figure 2.3 Plot showing the relationship between uptake/metabolic rate and cell size (Jumars (1993); Kiørboe (2008)). Point 1a and 1b defines the maximum cell size for a low and high ambient nutrient case, respectively. While point 2a and 2b indicates the most efficient cell size for a low and high ambient nutrient case, respectively. (Dashed and dotted red curves) Diffusion limited uptake rate. (Solid black curve) Cell metabolic rate.

Cell size limitation can be similarly explained by the decrease in diffusive flux per unit cell volume with increasing cell size, as Figure 2.4 shows. This is because the diffusive flux is proportional to r_0 whereas cell volume is proportional to r_0^3, which is driven by the fact that surface area to volume ratio decreases as the cell size increases (Karp-Boss et al. (1996); Roberts (1981); Smetacek (2000); Williams and Follows (2011)). However, this has a smaller role to play compared to the exponential increase in metabolic rate for an upper cell size limit (Kiørboe (2008)). The advantage of a smaller cell in diffusion cases may be evident in nature during the diatom reproductive cycle where the daughter cell is always smaller than the parent cell. Its size is constrained by the formation of the daughter cell inside the parent cell during cell division. As a diatom bloom progresses, nutrient levels wane and new cells are smaller than their predecessor which may be a slight advantage in a depleted environment (Jumars (1993); Kiørboe (2008)). However, a theory has been proposed, known as the “small yet large” theory. Where diatoms increase their cell size while also minimising the energy required to maintain the cell by importing and exporting ionic species into storage vessels, known as vacuoles, located in the cell (Kiørboe (2008); Menden-Deuer and Lessard (2000)).

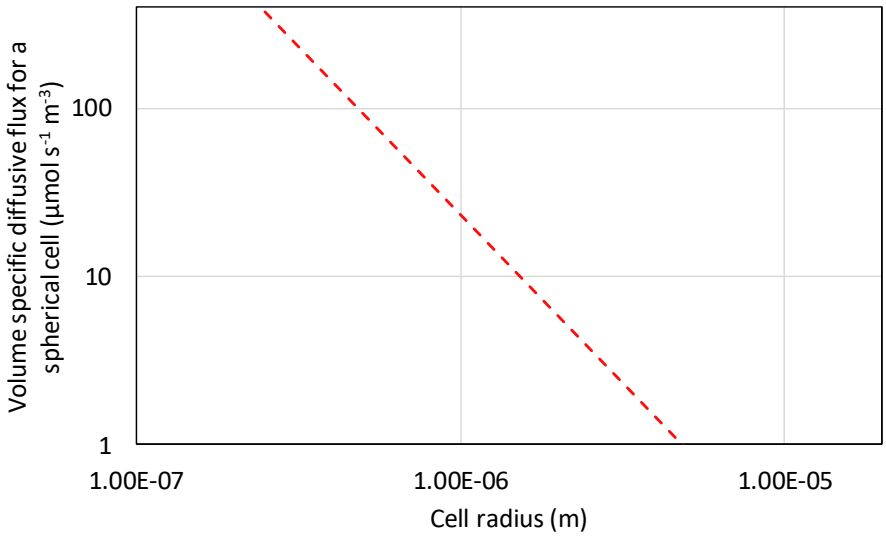

Figure 2.4 Volume specific diffusive flux ($\mu mols^{-1}m^{-3}$) for a spherical cell.

2.2.2 Cell Membrane Uptake

Now that the nature of diffusion towards or away from a spherical cell has been introduced, this section will expand upon the uptake across the cell membrane. Transport proteins in the cell membrane facilitate the transport of dissolved ions across the membrane into the diatom cell against an electrochemical gradient (Taylor (2009); Williams and Follows (2011)). Recent research papers have discussed the transport of ions across the diatom membrane through channels via action potentials; uptake of potassium (Boyd and Gradmann (1999a); Gradmann and Boyd (1999a)), uptake of nitrate and ammonium (Boyd and Gradmann (1999b)) and uptake of sodium and calcium (Gradmann and Boyd (2000, 1999b); Taylor (2009)). Action potentials are characterised by the electrical membrane potential increasing rapidly and then decreasing, this corresponds to ions being transported across the membrane (Taylor (2009)). As well as the uptake of nutrients across the diatom cell membrane being dependent on the finite number of these active uptake sites on the cell membrane and their handling time of ions (Williams and Follows (2011)), it has been demonstrated in numerous experimental studies (Eppley et al. (1969); Eppley and Thomas (1969); Falkowski (1975); Paasche (1973)) that the uptake rate of nutrients by phytoplankton is dependent on the ambient nutrient concentration as shown in Figure 2.5. V_{max} and K_{Sat} are usually measured in experiments to describe the behaviour of the uptake rate with respect to ambient concentration. V_{max} is the maximum cell uptake rate and K_{Sat} is the ambient concentration at $V_{max}/2$ (Harrison et al. (1989); Wheeler et al. (1982)).The origin of the curves is described below.

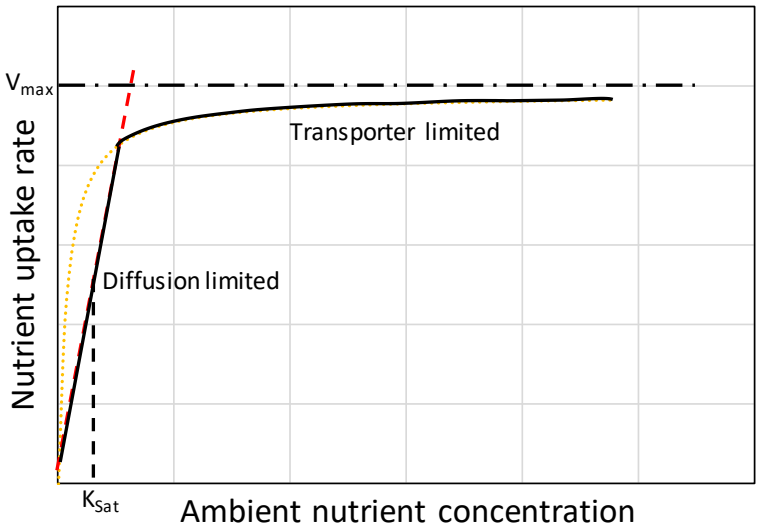

Figure 2.5 The theoretical form of the uptake curve as a function of ambient concentration. This is reflective of the Michaelis–Menten curve which is normally empirically fitted (Williams and Follows (2011)). (Dashed red curve) Diffusion limited uptake rate. (Dotted orange curve) Transporter limited cell uptake rate. (Solid black curve) Combination of both uptake limitations, diffusion limited at low ambient concentrations and transporter limited at high ambient concentrations.

The uptake is limited by the linear diffusive flux to the cell at low ambient nutrient concentrations as shown in Figure 2.5 and described in Equation 2.3. As the cell uptake rate is much larger than the diffusive flux, concentration at the external surface of the cell will become depleted ($C_\infty >> C_0$). This concentration condition defines the uptake rate from Equation 2.2 as,

$$V = 4\pi D_{fs} r_0 C_\infty. \tag{2.3}$$

Conversely, as the ambient concentration increases, the nutrient gradient outside the cell would diminish ($C_\infty \approx C_0$). In this limit there is an abundance of nutrients surrounding the cell and the only limitation is the physical uptake mechanism of the cell using transporters to move the ions internally. This uptake can be approximated by the Michaelis-Menten equation,

$$V = V_{max}\left(\frac{C_0}{K_{Sat} + C_0}\right) \tag{2.4}$$

where C_0 is the concentration at the cell surface.
As the ambient, C_∞, and surface, C_0, concentrations are approximately equal, in the limit of high ambient concentrations, the following relationship is obtained,

$$V = V_{max}\left(\frac{C_\infty}{K_{Sat}+C_\infty}\right). \tag{2.5}$$

The diffusion limited case described by Equation 2.3 is plotted in Figure 2.5 as the red dashed line, and the transport limited case described by Equation 2.5 is the orange dotted curve. The solid black curve represents a mixture of both depending on the relevant limiting flux.

The number of active uptake sites increases with the ambient nutrient concentration to make the most of this surplus of nutrients. However, similar to the cost/growth analysis discussed previously, there are two cases at which the percentage of coverage of the active uptake sites would be optimum and maximum. Above this maximum value the cost of making and maintaining transporters is greater than the benefit from the increased flux towards the cell used to maintain cell structure and operation. This then corresponds to an asymptoting of the uptake rate to a maximum value (V_{max}) in the transporter limited regime in Figure 2.5. There have been an increasing number of studies to determine the quantitative effect the density of uptake sites in the cell membrane and their handling times has on uptake rates (Aksnes and Egge (1991); Berg and Purcell (1977); Jumars et al. (1993)).
Berg and Purcell (1977) proposed another expression to describe the effect of the density of these active uptake sites on the uptake rate of the cell, taking a similar form to Equation 2.5 and given by,

$$Q_{Diff\_Mod.} = Q_{Diff}\left(\frac{Ns}{Ns+\pi r_0}\right). \tag{2.6}$$

N and s (m) are the number and radius of active absorptive sites on the cell membrane surface, respectively. r_0 (m) is the radius of the cell from its centre to its cell membrane. It does not take many active sites, approximately 2% of the surface covered, to regain the unabated diffusive flux, described in Equation 2.2.

Taking the analysis of the uptake of ions by cells further, Aksnes and Egge (1991) have included the handling times for the uptake sites in the form,

$$V = \frac{nAhC}{1+tAhC}. \tag{2.7}$$

Where V (No. of ions s^{-1}) is the uptake rate of ions by the cell, A (m^2) is the surface area of a transporter site, n is the number of transporter sites on the cell membrane, h (ms^{-1}) is the mass transfer coefficient, C (No. of ions m^{-3}) is the concentrations of solute and t (s) is

the handling time of a single ion in a transporter. They present the same limits as previous authors. The cell uptake rate approaches $nAhC$ in the diffusion limit at low concentrations. While it approaches nh^{-1} in the transporter limited regime in aquatic environments with plentiful nutrients. Most importantly, Aksnes and Egge (1991) proposed six hypotheses, defined below, regarding the link between the uptake parameters measured in experiments, i.e. V_{max} and K_{Sat}, and cell size and temperature.

1. V_{max} increases linearly with the square of the cell radius (Aksnes and Egge (1991)).
2. K_{Sat} increases linearly with cell radius (Aksnes and Egge (1991)).
3. V_{max}/K_{Sat} increases linearly with cell radius (Aksnes and Egge (1991)).
4. V_{max} increases exponentially with temperature (Aksnes and Egge (1991)).
5. K_{Sat} increases with temperature (Aksnes and Egge (1991)).
6. V_{max}/K_{Sat} increases with temperature similar to that of molecular diffusion (Aksnes and Egge (1991)).

Pasciak and Gavis (1974) further elucidated the relationship between uptake rate and ambient concentration. They assessed the influence of diffusion limited nutrient transport and the recharging of the diffusion boundary layer by fluid advection, on the uptake of nutrients across the cell membrane of multiple diatom species. Assuming a steady state case, the uptake of nutrients given by Equation 2.5, was equated with the diffusive transport of the nutrients towards the cell described by Equation 2.2. Using this approach they defined the parameter,

$$P = \frac{4\pi r_0 D K_{Sat}}{V_{Max}} \tag{2.8}$$

to assess the behaviour of the system. For large values of P, where $1/P << |1-(C_\infty/K_{Sat})|$, the cell absorbs nutrients so slowly that Equation 2.5 can be used to describe uptake, where $C_0 \approx C_\infty$. Conversely, for small values of P, where $1/P >> |1-(C_\infty/K_{Sat})|$, the uptake rate is limited by diffusion of chemicals towards the cell. For this case the uptake rate is described by,

$$V = V_{max}\left(\frac{PC_\infty}{K_{Sat}+PC_\infty}\right). \tag{2.9}$$

This relationship between P, the relative uptake rate V/V_{max} and the relative concentration C_∞/K_{Sat} is described in Figure 2.6.

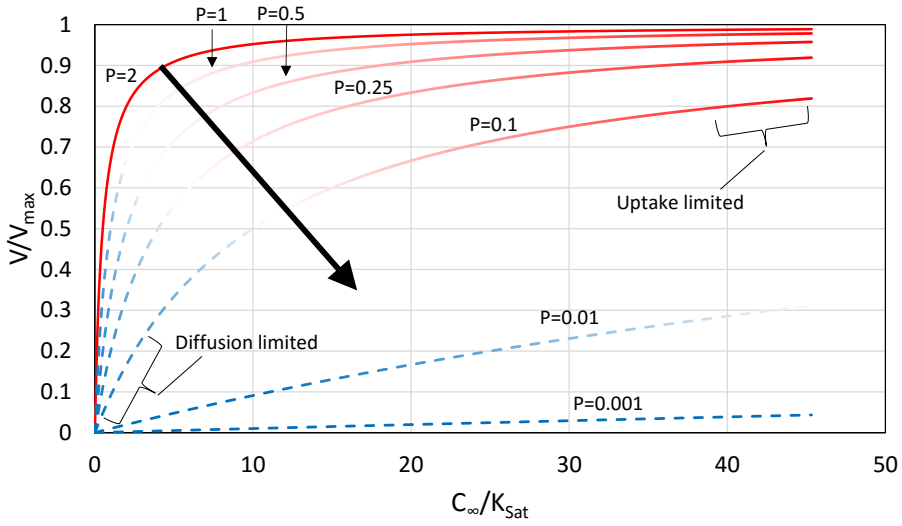

Figure 2.6 The relationship between relative uptake rate and non-dimensional ambient concentration (Pasciak and Gavis (1974)). (Solid red) Uptake limited. (Dashed blue) Diffusion limited. (Black arrow) Decreasing value of P. The strength of the colour indicates the dominance of the limitation on cell uptake.

As can be deduced from Figure 2.6, cell uptake at lower ambient concentrations is diffusion limited while being transporter limited at higher concentrations. However, this relationship is now dependent on the value P. A modified P^* value, which accounts for fluid advection relative to the cell, will be discussed in the next section.

2.2.3 Effect of Fluid Advection, Turbulence and Cell Shape on Mass Transport and Cell Uptake

For a motionless cell in a still hydrodynamic environment, transport of mass towards, or away, from that cell will be dictated by diffusion as discussed in the previous section. Furthermore, if the cell is considered a perfect absorber then it will be diffusion limited. The organism is said to be diffusion limited if the uptake of nutrients is faster than the transport of nutrients toward the cell by diffusion (Karp-Boss et al. (1996)). As mentioned in the previous section, the diffusive flux is proportional to the size of a spherical cell. However, an increase in diatom cell size actually increases the effectiveness of turbulence and advection on enhancing the transport of mass to the cell and reduces the likelihood of being consumed by predators (Kiørboe (2008)).

Relative motion between seawater and the cell surface can replenish the immediate area of depleted nutrients adjacent to the cell's surface and increases the concentration gradient

along the radial direction towards the cell and thus increases the diffusive flux (Karp-Boss et al. (1996)).
This relative fluid motion can be generated by either turbulence or diatoms sinking and rising through the water column. The effect of this relative fluid motion on the flux across the diffusion boundary layer of small, non-swimming organisms has been investigated theoretically by Jumars et al. (1993), Karp-Boss et al. (1996), Munk and Riley (1952), Kiørboe (1993), Gavis (1976), Kiørboe (2008) and Lazier and Mann (1989). Karp-Boss et al. (1996) provides the most critical analysis on this area of research, while Guasto et al. (2011) provides a comprehensive review.

From early research, relative motion between the fluid and a cell, i.e. sinking at 10 *cell diameters* s^{-1}, was found to enhance the diffusive flux by $\approx 100\%$ for cells greater than $\approx 20\mu m$ (Berg and Purcell (1977); Munk and Riley (1952)). Turbulence has a noticeable enhancement of this diffusive flux as well but for motionless organisms $> 100\mu m$ experiencing strong turbulence and $> 1mm$ in weak turbulence (Lazier and Mann (1989)). These studies assumed a constant background concentration and steady state conditions.
For the same steady state conditions, similar to their work in defining the uptake rate of a cell for a solely diffusive case, Pasciak and Gavis (1974) found an expression to modify P, (to become P^*) which includes advection as well, which is given by,

$$P^* = P\left(1 + \frac{r_0 u}{2D_{fs}}\right). \tag{2.10}$$

u (ms^{-1}) is the relative velocity between the fluid and the diatom cell. P is the non-dimensional parameter defined in Equation 2.8.

The Sherwood number (Sh) is a dimensionless term which defines the ratio between the total net flux and the net flux due to the diffusion of matter (Karp-Boss et al. (1996)). This is an indication of how much the flux is enhanced by fluid advection (Karp-Boss et al. (1996)). For example if $Sh = 1.4$ for a convective case then advection enhances the transport of matter by 40% relative to diffusion only. The Sherwood number is empirically dependent on the dimensionless Reynolds (Re) and Péclet (Pe) numbers. The Reynolds number is the ratio of inertial to viscous forces given by $Re = \rho uL/\mu$ and it describes the state of turbulent flow. Pe is the ratio of advection to diffusive transport. The second term in the brackets in Equation 2.10 is actually $Pe/2$. For the laminar flow case around a spherical diatom cell $Sh \approx 1$, for $Pe < 1$, and begins to increase at $Pe \approx 1$ (Karp-Boss et al. (1996)). There exists a general relationship where fluid advection, either from turbulence or sinking, enhances the flux towards, or away from, a diffusion limited cell. Empirical Péclet-Sherwood relationships based on analogous engineering heat transfer analysis were used to give a

more accurate view of how much the mass flux is enhanced by fluid advection (Karp-Boss et al. (1996); Musielak et al. (2009)). To achieve an enhancement in mass flux of 100% of its original value for a sinking spherical diatom cell the critical cell size ranges from $40-85\mu m$, depending on the variation in density between the cell and its fluid environment when sinking (Karp-Boss et al. (1996)). In addition, the critical size of a microorganism affected by small-scale turbulence was found to be $\approx 160-200\mu m$ for a 100% increase in mass flux, or $\approx 60-100\mu m$ for a 50% increase (Karp-Boss et al. (1996)). Below these size ranges advection does not significantly enhance mass transport. Karp-Boss et al. (1996) went on to elucidate the shortfalls of these early studies for mass flux enhancement for low *Re* cases for phytoplankton cells.

These findings are critical to diatoms as they cannot provide their own relative fluid flow by swimming or moving the water around them. Diatoms are considered passive feeders and without the ability to replenish the depleted concentration of particles at their surface they risk being diffusion limited (Karp-Boss et al. (1996)). Considering this, the intermittency of turbulence is of interest as to how long and how frequent a diatom cell is exposed to beneficial conditions that enhance mass transport towards the cell in turbulent water (Karp-Boss et al. (1996)).

2.3 The Dynamic Fluid Environment of Diatoms

2.3.1 Advection

As mentioned previously, diatoms do not possess their own propulsion system to seek out nutrients or light like their competitors i.e. bacteria and other phytoplankton (Mitchell et al. (2013)), they spend the majority of their time in the more turbulent upper mixed layer / euphotic zone of aquatic environments (Mitchell et al. (2013); Stocker (2012)) at the mercy of the inherent fluid motion. This is illustrated in Figure 2.7.

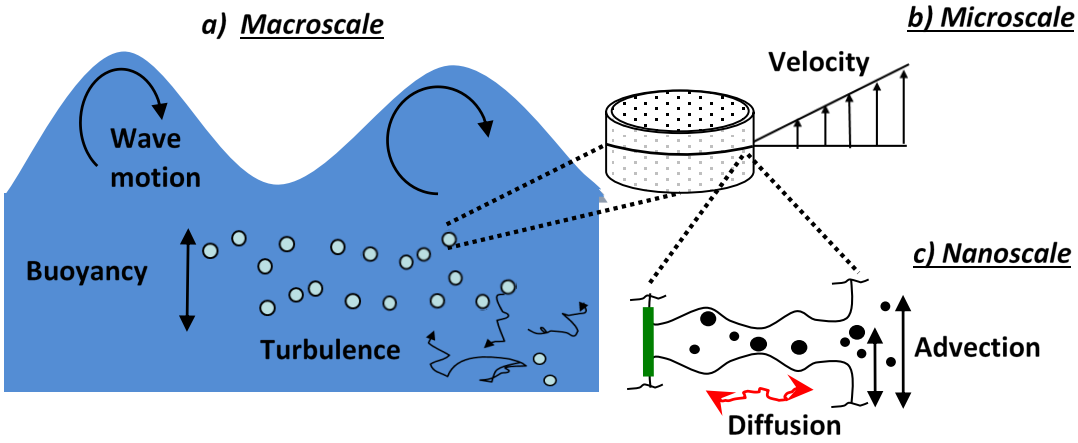

Figure 2.7 Different types of flow fluctuations experienced by pelagic marine diatoms from the macro- to nanoscale (Yang et al. (2011)). Reproduction from Yang et al. (2011) with permission from the Royal Society of Chemistry

Turbulence in the ocean is comprised of different sized eddies caused by a number of unsteady fluctuations, disturbances and instabilities, i.e. currents, tides or waves (Gregg (1973)). There exists a transfer of kinetic energy from larger to smaller eddies (Kiørboe (2008)). The smallest eddy is inversely proportional to the intensity of turbulence (KoehlI et al. (2003)) and is characterised by the Kolmogorov length (Kolmogorov (1941)),

$$\eta = \left(\frac{\nu^3}{\varepsilon}\right)^{\frac{1}{4}} \tag{2.11}$$

where $\eta > \eta_b$. Assuming the energy dissipation in the ocean ranges from $10^{-5} m^2 s^{-3}$ in the upper mixed layer, for wind speeds of $15-20 ms^{-1}$, to $10^{-9} m^2 s^{-3}$ in deeper parts of the ocean (Kiørboe (2008)), the scales of the smallest eddies are typically between $1-10 mm$ (Karp-Boss et al. (1996); KoehlI et al. (2003)). Eddies below the Kolmogorov length are

dominated by viscous forces, and this flow can be described by a linear shear. Eventually, these eddies transfer their energy as heat through molecular interactions (Kolmogorov (1941)). The size of the smallest eddies are still much larger than the microscopic size of diatoms, which means they experience a laminar flow, illustrated by the linear fluid velocity field in Figure 2.7 (KoehlI et al. (2003); Lazier and Mann (1989); Yang et al. (2011)).
The unsteadiness of the linear velocity field below the Kolmogorov scale can be described by (Lazier and Mann (1989); Mitchell et al. (1985); Musielak et al. (2009)),

$$\tau = 2\pi \left(\frac{\nu}{\varepsilon}\right)^{\frac{1}{2}} \tag{2.12}$$

which characterises the correlation time of a local shear field, until a new one is generated with a new magnitude and direction (Karp-Boss and Jumars (1998); Musielak et al. (2009); Tennekes and Lumley (1972)). From the values of energy dissipation above the correlation time of a Kolmogorov eddy shear field in the ocean ranges over $\tau \approx 0.6 - 200s$. The characteristic velocity difference (u_{shear}) between two points in turbulence, below the Kolmogorov length, is given by (Hill (1992)),

$$u_{shear} = 0.42Gd = 0.42d \left(\frac{\varepsilon}{\nu}\right)^{\frac{1}{2}} \tag{2.13}$$

where d (m) is the distance between the two points and G (s^{-1}) is the shear rate. The typical range of values for this shear velocity, at the length scales of centric marine diatoms, is $\approx 40 - 130\mu m s^{-1}$. This flow can be characterised using the ratio of inertial to viscous forces called the Reynolds number which is given by $Re = \rho U_c L_c / \mu$. The low velocities and small spatial scales means the flow is dominated by viscous forces ($Re < 1$) and is laminar.

Diatoms are either cylindrical or ellipsoidal but certainly not spherical, so their shape must be considered when describing their physical interaction with fluid flow. The three-dimensional kinematic rotational trajectory can be approximated for an elongated diatom cell in a linear shear field, generated by turbulence, with the Jeffery orbit model for a prolate spheroid. A possible trajectory is shown in Figure 2.8 (Kim and Karrila (2013); Pahlow et al. (1998)).
The period of this orbit is defined by (Kim and Karrila (2013)),

$$T_{JO} = \frac{2\pi}{G}\left(r_a + r_a^{-1}\right) \tag{2.14}$$

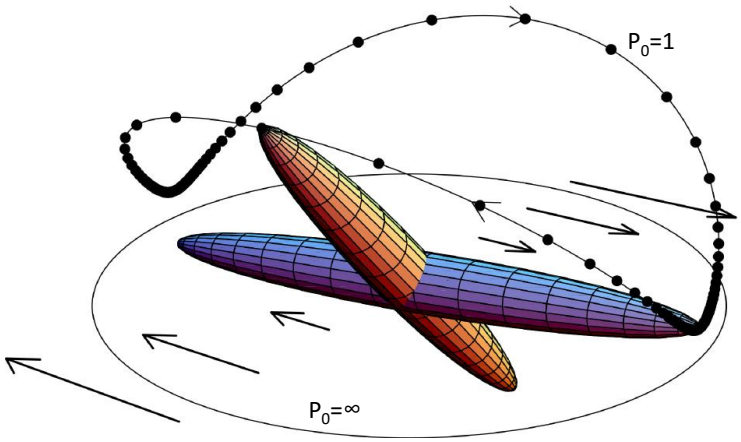

Figure 2.8 Positional trajectory of a prolate spheroid experiencing a linear shear field — Jeffery orbit (Pahlow et al. (1998)). The diagram shows two positions of one prolate cell at its highest and lowest velocity rotation, corresponding to the largest and smallest spacing between black dots, respectively. The orbit parameter P_0 dictates the orbit path taken by the prolate cell (Kim and Karrila (2013)). Pahlow M, Riebesell U, Wolf-Gladrow DA. Impact of cell shape and chain formation on nutrient acquisition by marine diatoms. Limnology and Oceanography 1997;42:1660-72. Copyright Wiley. Reproduced with permission.

where r_a (m) is the aspect ratio of the diatom cell. The shear rate, G (s^{-1}), present in a Kolmogorov eddy can be defined as,

$$G = \left(\frac{\varepsilon}{\nu}\right)^{\frac{1}{2}} \tag{2.15}$$

and is expected to be $0.03 - 10s^{-1}$ (Kiørboe (2008)).

As shown in Figure 2.9, for the typical values of energy dissipation rates in the ocean, the period of orbit, T_{JO}, is much larger than the residence time of the linear shear field, τ, and therefore intermittency of the shear field provides the dominant force relevant for diatoms in their natural environment. However it is a complex interaction where Jeffery orbit motion will still play a part in diatom motion.

The rotational motion of diatoms, and the intermittency of the shear field due to turbulence generates fluid advection relative to the diatoms' surface (Pahlow et al. (1998)). This facilitates advective transport ($L > \eta$ and $\eta > L > \eta_b$) and diffusive transport ($L < \eta_b$) and affects the supply of nutrients to the external surface of the frustule. This in-turn impacts upon the next stage of transport, through the pores of the frustule as well as uptake by the cell membrane.

Similar to the mixing of nutrients in a turbulent ocean, the shear fields generated by turbulence can also transport nutrients closer to a diatom cell. Consider the case depicted in

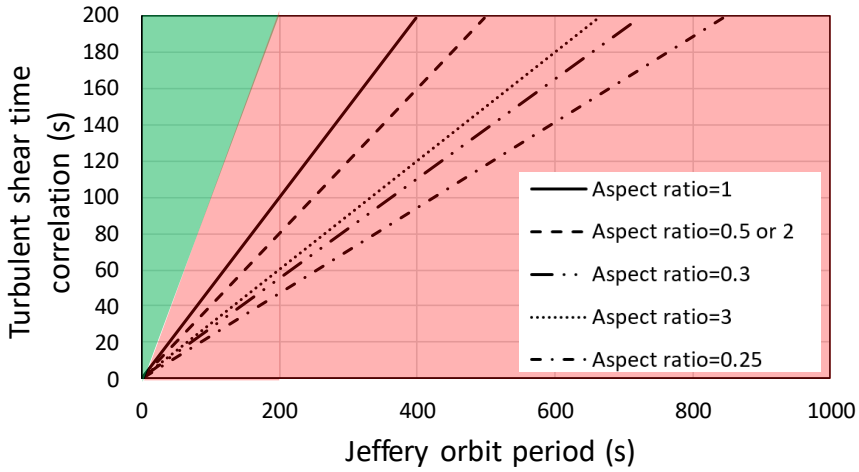

Figure 2.9 Relationship between Jeffery orbit period (T_{JO}) and the correlation time (τ) for turbulent linear shear field for diatoms with various cell aspect ratios. Red shaded section represents aspect ratios where the period of the Jeffery orbit is dominant over the correlation time for turbulent shear.

Figure 2.10, where a nutrient "hotspot" is elongated by a linear shear field. While the diatom is the same distance away from the centre of the original nutrient plume, D_1, the thinning out of the plume due to the shear field has brought it closer to the cell, D_2, where diffusion takes over at smaller spatial scales to reach the cell.

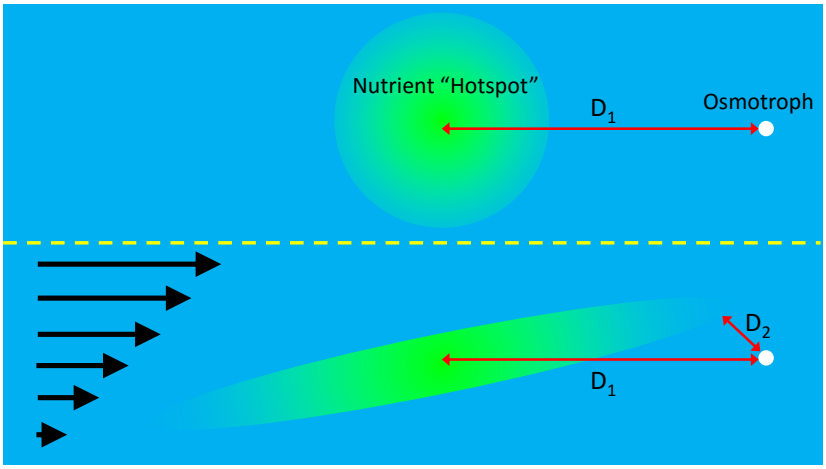

Figure 2.10 Effect of a linear fluid shear field on the distance between nutrients in an osmotroph's surrounding aquatic environment (Kiørboe (2008)).

2.3.2 Sinking / Buoyancy

In addition to turbulence, the presence of a diatom's silica frustule generally makes them denser than water and can therefore sink in the water column. The sinking rate of *Coscinodiscus sp.* has been reported to be $80-350\mu ms^{-1}$ (Eppley et al. (1967); Smayda (1971, 1970)) and is characterised by laminar flow with $Re \approx 0.002-0.02$ (Karp-Boss et al. (1996); Smayda (1970)). Whilst sinking at these low Reynolds numbers, the frustule does not orient itself to maximise its drag, such as the case in higher Re situations, it will retain its initial arbitrary orientation unless the center of mass is redistributed within the cell during sinking (Sournia (1982)). Also, sinking rates in individual diatoms may be controlled by; forming chains with other individual cells or growing spines on their silica frustules to increase hydrodynamic drag (Guasto et al. (2011); Raven and Waite (2004)). However, chain formation is suspected to take place for a number of other reasons, including; improved nutrient uptake, protection from predators and improving chances of fertilisation (Musielak et al. (2009)).
Stokes' law predicts an increase in sinking rates with the square of the radius of a sinking sphere

$$v_s = \frac{2}{9}\frac{\rho_p - \rho_f}{\mu} g R^2, \tag{2.16}$$

where v_s (ms^{-1}) is the settling velocity, ρ_p and ρ_f (kgm^{-3}) is the sphere and fluid density, respectively, and R (m) is the particle radius. Whereas, sinking rates in diatoms follow a weaker dependence on the radius and this has been suggested to be a result of the decrease in diatom cell density with an increase in size i.e. due to the presence of carbohydrate ballasting in and out of vesicles in larger diatoms $> 100\mu m$ (Guasto et al. (2011); Miklasz and Denny (2010)). Miklasz and Denny (2010) suggested that the effect of the porosity of the frustule and the presence of a mucilage layer on its surface on the sinking rate is not significant although this hypothesis is yet to be proved. In addition to sinking, some larger diatoms have the ability to control their buoyancy within the water column. Buoyancy is generally controlled by carbohydrate ballasting in vesicles in diatoms $> 20\mu m$ or ion replacement in vacuoles in diatoms $< 20\mu m$ (Anderson and Sweeney (1978); Fisher (1995); Gross and Zeuthen (1948); Moore and Villareal (1996)). Recently, Gemmell et al. (2016) showed variation in the instantaneous sinking rate of $10-750\mu ms^{-1}$ for *Coscinodiscus waiselii* depending on different nutrient deplete/replete conditions, with a period of this sinking rate variation on the order of seconds. These experimental findings suggest that larger diatoms can finely control their sinking rates and therefore nutrient fluxes towards the cell, which is in response to metabolic cues from the cell.

As a result of reviewing past research, relative advection between a diatom and the surrounding ocean is a result of:

1. Turbulence, i.e. from currents, waves or tides, causing fluid shearing which, at the length scale of a diatom, can be considered a linear shear field. This linear shear promotes the rotation of an elongated diatom following the motion of a Jeffery orbit.

2. Controlled transient buoyancy forces causing sinking and rising in the water column.

2.3.3 Effect of Chain Formation

It has been established that there are variables which affect nutrient uptake by single diatoms including; fluid advection in a turbulent environment, cell shape and cell rotation. However diatoms often form chains that are attached by sticky polysaccharide excreations (Karp-Boss and Jumars (1998); Musielak et al. (2009); Pahlow et al. (1998); Round et al. (1990); Srajer et al. (2009)). For an advection case, a single prolate cell experienced greater nutrient supply compared to a spherical cell, while cell chains experienced an even greater nutrient supply than that of a prolate spheroid (Pahlow et al. (1998)). This was suggested to be due to the unsteady "flipping" of the elongated spheroid (KoehlI et al. (2003)). Nevertheless, diatom chains exhibit a decrease in diffusive flux and taking this into account, the total nutrient supply to a chain is worse than for a single spherical cell (Pahlow et al. (1998)). However, chain formation was favourable in high nutrient concentrations and turbulence. This may be reflected within a natural marine ecosystem, where at the beginning of a phytoplankton bloom, which corresponds to higher nutrient and turbulence levels, chain formation would be promoted and chains would get shorter as the bloom progressed (Pahlow et al. (1998)). Interestingly, the chains were modelled as rigid prolate spheroids of constant small radius, where the aspect ratio was varied to change the length of the chain (Pahlow et al. (1998)). Musielak et al. (2009) completed a similar diatom chain versus solitary cell nutrient uptake analysis in turbulence with uniform and heterogeneous ambient nutrient concentration. They analysed it in two dimensions, with spacing between the cells and considering chain stiffness. Stiffer chains (per cell) are better at getting nutrients than individual cells. Also, in a heterogenous ambient nutrient environment the stiffer chains had a greater uptake compared to more flexible chains which tend to "ball up" to a smaller size in the flow, becoming too small to capture those nutrient "hotspots". There was a local variation of *Sh* observed with relative tangential flow over the chain resulting in a thinning of the diffusion boundary layer and generating large values of *Sh*. Musielak et al. (2009) and Pahlow et al. (1998) only considered flux of nutrients in neutrally buoyant diatoms in shear flows and did not consider sinking effects.

Interestingly, it has been proposed that the relative movement of water across the diatom chain, *Rutilaria philipinnarum*, generates one-dimensional oscillations between the diatom units in the chain creating a pumping flow between the valves of the adjacent diatoms, as shown in Figure 2.11 (Srajer et al. (2009)).

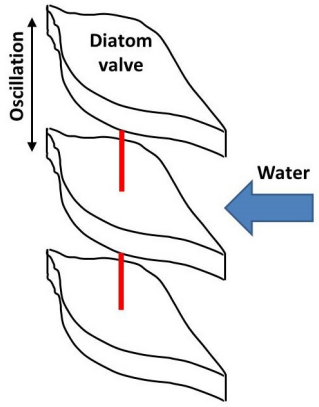

Figure 2.11 Oscillating diatoms in chains acts as a pump transferring mass through their valve (Srajer et al. (2009)).

All of these studies concerning the effect of advection, turbulence, diffusion and uptake on the transport of mass towards/away from the cell of a diatom do not consider the effect of the rigid frustule or distinguish its effect.

2.4 Effect of the Frustule on Mass Transport

This section examines the influence of the valve and girdle band pore shape and overall frustule morphology on mass transport with specific reference to well-documented centric diatom species; *Coscinodiscus sp.* and *Thalassiosira sp.*

2.4.1 Morphology of the valve structure of *Coscinodiscus sp.* and *Thalassiosira sp.*

The centric diatom valves comprise of microscale chambers, known as aereoli, bound on one end by a porous sieve plate (cribellum) while the other end is unbound, shown in Figure 2.12 (Losic et al. (2006)). These pores are characterised by a near-cylindrical shape.

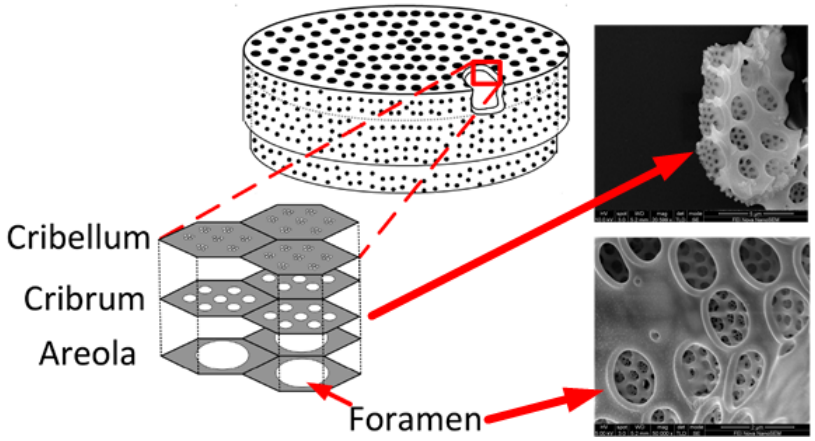

Figure 2.12 (Left) Valve structure of *Coscinodiscus sp.* (Losic et al. (2007a)). (Right) SEM images of the valve pore structure of *Coscinodiscus wailesii*.

Coscinodiscus sp. incorporates three layers into their valve structure; the cribellum (external), cribrum (mid) and finally the aereoli chambers (internal)[2]. The porosity and pore size of each layer increases moving from the outside to the inside layer (Losic et al. (2006)). *Thalassiosira eccentrica* has a similar structure to that of *Coscinodiscus sp.*, however the order of the porous layers are reversed, and it has only two – the cribellum and aereoli chambers (Losic et al. (2006)).

An organic layer also surrounds the inorganic silica frustule from when it is generated inside the silica deposition vesicles located in the protoplast of the cell (Round et al. (1990)). This organic coating around the frustule is thought to prevent dissolution of the silica frustule in its aquatic environment (Lewin (1961); Round et al. (1990)). Furthermore, a diatotepic layer, which is an organic polysaccharide, has been found between the frustule and the cell membrane. The role of this layer is not fully understood but it has been suggested it may be used to help contain the contents of the cell (Von Stosch (1981)). Both these organic layers are thought to also reduce the effective size of the pore in the silica frustule and therefore modify its permeability (Round et al. (1990); Von Stosch (1981)).

A summary of the general frustule dimensions of the diatoms; *Coscinodiscus sp.* and *T. eccentrica* are given in Appendix A in Table A.2 (Losic et al. (2006)) showing, interestingly, very similar pore sizes, however reversed valve layer architecture.

[2]The terms “internal” or “inside” and “external” or "outside" refers to the location adjacent to the cell membrane or the surrounding marine environment, respectively

2.4.2 Morphology of the girdle band of *Coscinodiscus sp.*

The girdle band pores are axisymmetric and have an asymmetric profile (Losic et al. (2007b); Yang et al. (2011)). The asymmetry of the pore is specified with respect to the change in the diameter of the pore along its axis shown in Figure 2.13. Generally, there is only one repeating asymmetric unit through the thickness of the girdle bands, however, two can exist in series in regions where the girdle bands overlap one another.

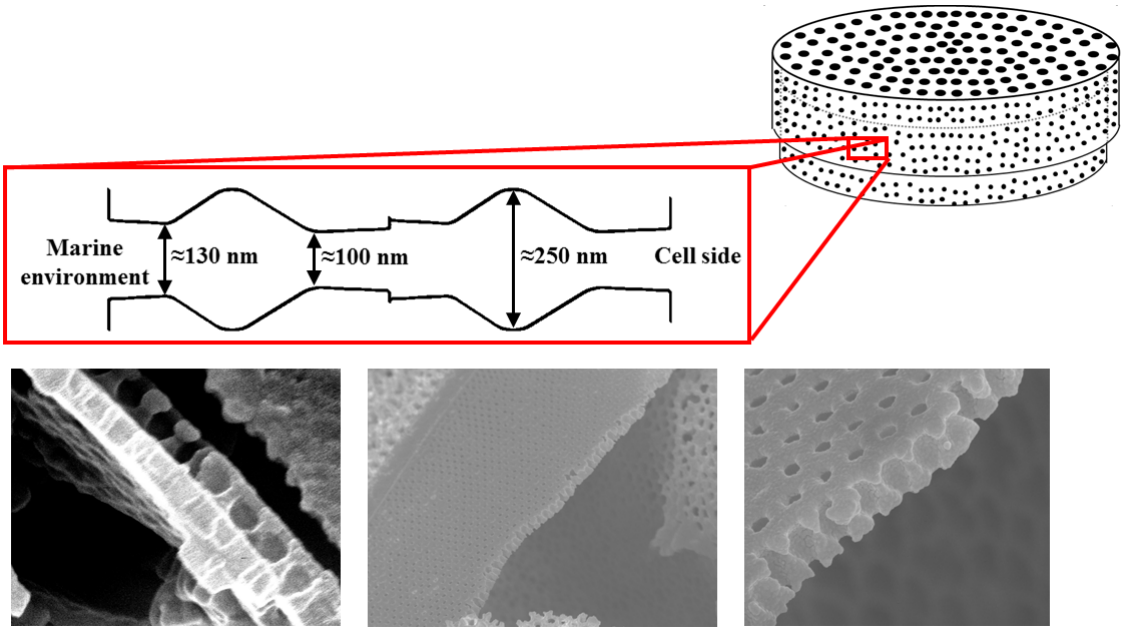

Figure 2.13 (Top) Approximate schematic representation of a section of an axisymmetric girdle band pore. (Bottom) SEM images of the girdle band structure of *Coscinodiscus wailesii*.

2.4.3 Mass Transport Through the Valve Pores

As covered in the previous section, a detailed structural examination has been completed by Losic et al. (2006) using AFM and SEM for the two centric diatom species *Coscinodiscus sp.* and *T. eccentric* in a further attempt to describe the diatom frustule's capability to sort and filter particles. The following interesting observations have been made with respect to this capability:

- The smallest pores, common to both frustules, are $\approx 45nm$ in diameter which may indicate a common size exclusive particle filtering capacity (Losic et al. (2006)).

- Ridges around the foramen on the inside of the frustule valve of *Coscinodiscus sp.*, form radial channels from the centre of the valve (Losic et al. (2007a)).
- Diffusion based filtering capabilities. The variation in geometry through the pores in the frustule could produce entropic barriers which can influence diffusion (Rosengarten (2009)).

Given the above observations it still remains unknown what dictates the size and shape of pores in the diatom frustule. As outlined in Table A.2 in Appendix A, there is a physical restrictive lower limit on the size of particles allowed to pass through the frustule barrier, dictated by the smallest pore diameter of $\approx 45nm$ in the valve's sieve plate and $\approx 100nm$ in the girdle band pores. In live diatoms these opening sizes are likely to be smaller due to an organic coating over the silica. Losic et al. (2009) suggests the function of the diatom sieve plate (valve layer with the smallest pores) is used for "molecular and colloidal sorting". This size restriction corresponds to the ultrafiltration/nanofiltration regime illustrated in Figure 2.2. The typical size of viruses which infect diatoms is of the order of $25-220nm$ (Nagasaki (2008)). Thus while there is a chance for small viruses to enter the pores, entities smaller than the minimum pore diameter are much more likely to be ionic species useful for diatom growth rather than harmful viruses (Losic et al. (2006)). Alternatively, the fabrication of the smallest pore size may be a geometric limitation of the arrangement of the silica nodules precipitated when the frustule is first formed. These silica nodules are the building blocks of the frustule. The average diameter of a silica nodule in the frustules of *Coscinodiscus sp.* and *T. eccentrica* ranges from $20-70nm$ (Losic et al. (2007a)). The silica nodules increase in size moving towards the outer porous layers in both species and it is not yet understood why this occurs (Losic et al. (2007a)).

The cribellum layer and girdle bands of *Coscinodiscus sp.* are the most fragile part of the frustule based on mechanical testing by Losic et al. (2007b) and Hamm et al. (2003). As the cribellum layer does not seem to be an integral load bearing structure, it has been suggested that it solely has an alternative function, such as acting as a sieve plate (Losic et al. (2006)). Also, it may be that the remainder of the ornate rigid frustule structure like the aereoli chambers, are used to maintain the structural integrity of this very thin and delicate sieve plate (Hamm (2005)). However, this raises the question, why is the sandwich type structure reversed in the two aforementioned diatom species? And why are the girdle band pores, which can cover more than half the surface area of the total frustule, different to the valve pores? The answer to the former question may have been elucidated by Mitchell et al. (2013). They have proposed that the order of the different porous layers in the valve of *Coscinodiscus sp.* is suited to conditions of nutrient pulses in which there is a lull in ambient nutrient concentration because of the heterogeneous distribution of chemicals in the ocean.

653 The aereoli chambers act as a temporary holding chamber for nutrients after the pulse has
654 dissipated. Whereas, the valve of *Thalassiosira sp.* characterised by the reversed porous
655 layer to that of *Coscinodiscus sp.* is more suited to homogenous nutrient environments, in
Figure 2.14 (Mitchell et al. (2013)).

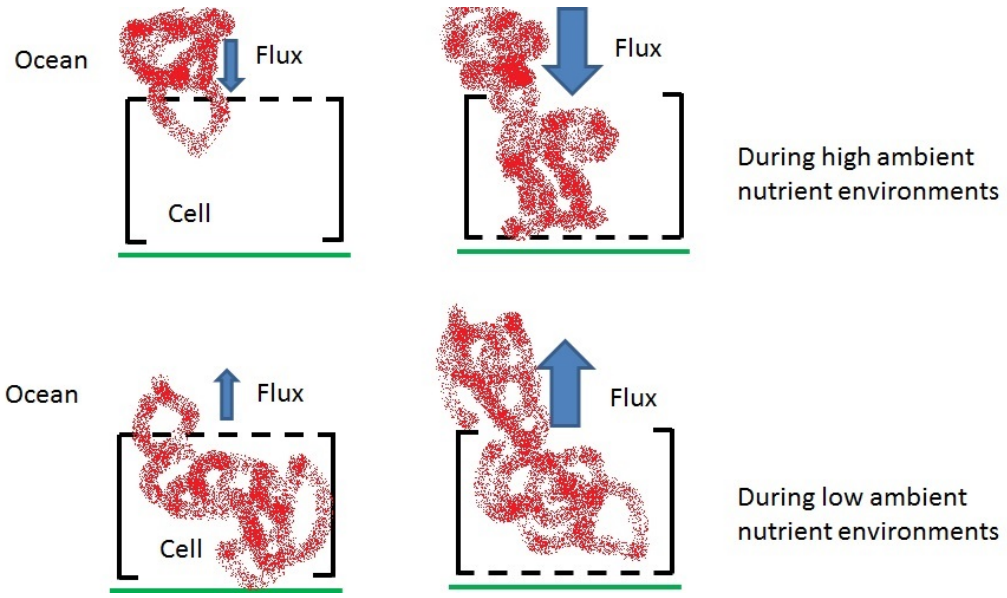

Figure 2.14 (Left) *Coscinodiscus sp.* more suited to heterogeneous nutrient environments and (Right) *Thalassiosira sp.* more suited to homogeneous nutrient environments.

656
657 This work shows an advantageous role the frustule can play in environments with differing
658 distributions of nutrients. There also exists the possibility that either the crossflow or dead-
659 end flow through the pores generates small vortices assisting in the transport of matter
660 (Cardenas (2008)). This prospect has not been explored with respect to diatom frustules as of
661 yet.

662 In an attempt to explain the effect of the frustule on diffusive mass transport a number
663 of experiments have been assessing the effective diffusion of solutes through the valves of
664 diatoms. A diatom valve from *Coscinodiscus sp.* attached to the end of a microcapillary, as
665 shown in Figure 2.15, demonstrated its filtrate size selectivity by allowing 20*nm* particles
666 to diffuse through the diatom valve whilst preventing 100*nm* particles doing the same.
667 This also demonstrated the feasibility of directly applying a diatom valve into a crossflow
668 microflitration setup (Losic et al. (2006)). This is the first known direct application of a
669 diatom valve in a microfluidic device and serves as a proof-of-concept for future applications
670 in microfluidic devices for filtration purposes. Broken diatom frustules do, however, have a
671 history of being used as efficient macroscale filters in the form of diatomaceous earth (Barron
672 et al. (1982); Farrah et al. (1991); Schuler et al. (1991)).

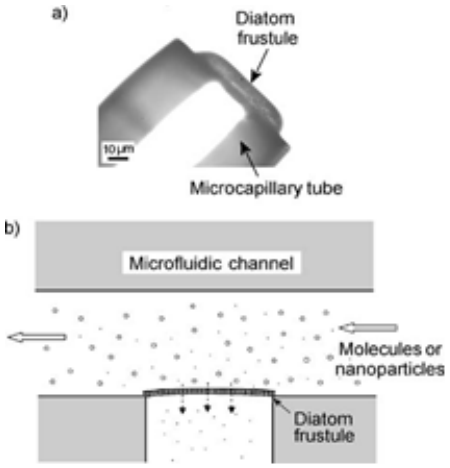

Figure 2.15 Attachment of a frustule valve, from *Coscinodiscus sp.*, over the opening of a microcapillary tube. As illustrated in the experiment schematic crossflow filtration through a diatom valve was observed (Losic et al. (2006)). Reproduction from Losic et al. (2006) (Figure 5), with permission from American Scientific Publishers.

673 The diffusion coefficient of small dye particles, approximately 1*nm* in size, has been
674 characterised through a diatom valve from *Coscinodiscus sp.* with only the aereoli pores
675 present (porosity $\approx 29\%$) and one with the cribellum (fine sieve plate) layer removed (porosity
676 $\approx 14\%$) (Bhatta et al. (2009b)). This was completed to determine the influence of the frustule
677 on a solute with a small particle to pore diameter ratio. From Figure 2.16, these experiments
678 showed that as the toruosity increased or the porosity decreased, the diffusion coefficient
679 decreased by an order of magnitude compared to free-space diffusion.

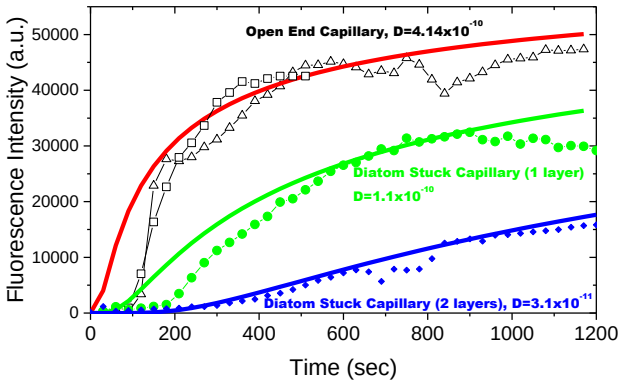

Figure 2.16 Experimental analysis of the diffusion through two different diatom valves and free diffusion (Bhatta et al. (2009b)). Theoretical curves (solid lines) were fitted to the experimental data to calculate the corresponding diffusion coefficients. Reproduction from Bhatta et al. (2009b) with permission from Trans Tech Publications Ltd.

A more detailed experiment looking at the diffusion of small dye particles, approximately $0.6nm$ in size through a single aereoli pore and the cribrum layer showed the diffusion coefficient was almost half of that for free-space diffusion (Bhatta et al. (2009a)). The diffusion coefficient through the diatom pores was found to be $\approx 8.9 \times 10^{-10} m^2 s^{-1}$ for Oregon Green dye particles of diameter $0.6nm$ (Bhatta et al. (2009a)). This result is comparable to the diffusion coefficient measured in the previous experiment of $\approx 3.1 \times 10^{-11} m^2 s^{-1}$ for a similar case. This result was unlikely due to hindered diffusion as the dye molecules were considerably smaller (≈ 80 times) than the pore diameter.

These studies do suggest that diffusion is affected by either the walls of the frustule or even entropic trapping due to the sudden change in size of pore. An example of how the diffusion coefficient may vary due to the relative diffusivities is shown schematically in Figure 2.17.

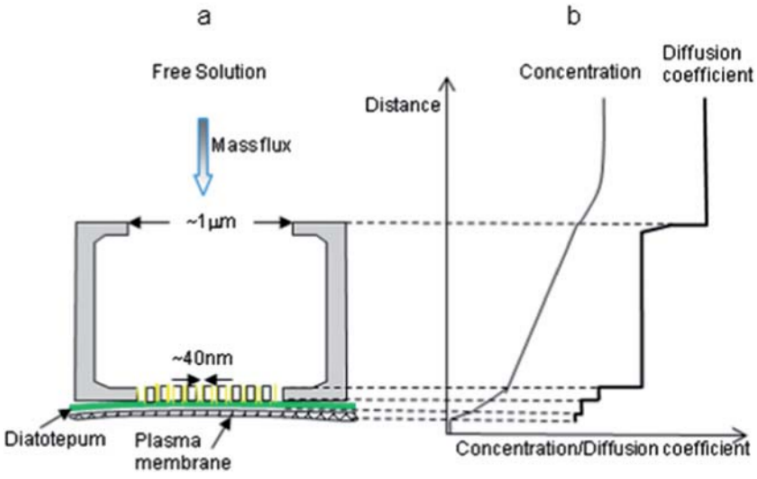

Figure 2.17 (Left) Cross sectional schematic of a diatom aereoli and cribellum pores in a generic diatom valve. (Right) Prediction of the concentration gradient and diffusion coefficients through those pores (Yang et al. (2011)). Reproduction from Yang et al. (2011) with permission from the Royal Society of Chemistry.

Whilst also reducing the area available for solute to diffuse through the frustule, the walls of the frustule actually alter the near diffusion coefficient of particles. This can be seen in Figure 2.17 where the diffusion coefficient and the concentration is shown to vary through the structure of a diatom frustule pore, diffusing from the "free solution" to the cell membrane. From experiments by Carbajal-Tinoco et al. (2007), it can be seen that the perpendicular and parallel components of the diffusion coefficient of a rigid microparticle is dependent on the minimum distance to a rigid wall. The diffusion tends to zero closer to the wall whereas it tends to the free-space diffusion coefficient away from the wall. This spatial variation in a particles' diffusion coefficient is a result of lubrication forces between a particle and a solid

wall. Results from experiments by Carbajal-Tinoco et al. (2007), in Figure 2.18, show this variation in parallel and perpendicular diffusion coefficients in proximity to a solid wall.

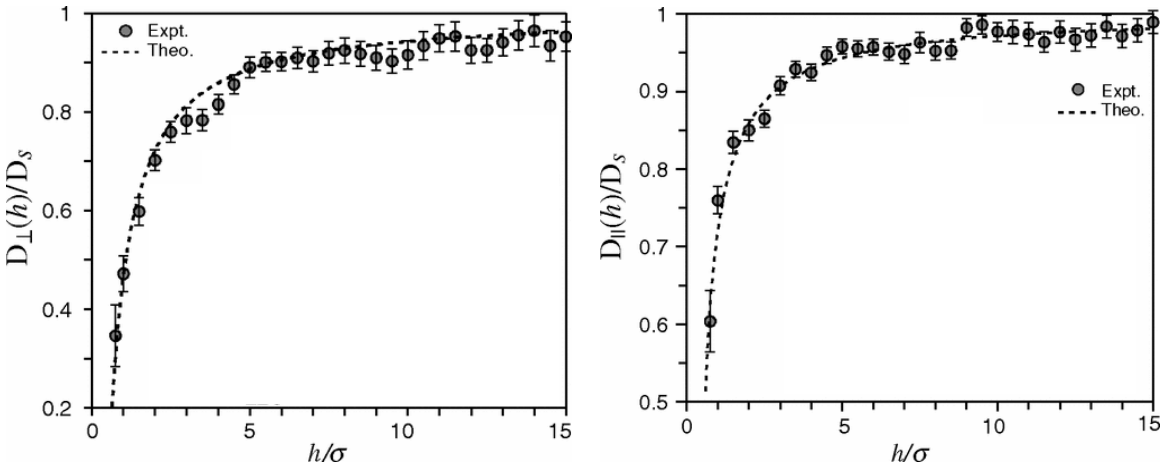

Figure 2.18 Dependency of particle diffusion coefficient (Left) perpendicular and (Right) parallel to a rigid wall. D_S is the free-space diffusion coefficient, h is the minimum distance from the centre of the particle to the wall and σ is the diameter of the particle (Carbajal-Tinoco et al. (2007)). Reprinted figures with permission from Carbajal-Tinoco MD, Lopez-Fernandez R, Arauz-Lara JL. Asymmetry in Colloidal Diffusion near a Rigid Wall. Physical Review Letters 2007;99:138303. Copyright 2007 by the American Physical Society.

With the pore walls of the frustule changing orientation with constrictions and expansions through the thickness of the valve like that depicted in Figure 2.17, the diffusion coefficient starts to decrease in a region around 5 particle radii from the wall.

A numerical simulation was completed by the author to show how the concentration field varies between a diatom with and without a frustule over time. The results are shown in Figure 2.19. The diffusion problem was modelled using a one-dimensional Forward Time Centered Space (FTCS) finite difference scheme to calculate the concentration profile over time. To represent a cell with a frustule surrounding it, a band surrounding the cell with a lower diffusion coefficient than that for free-space was numerically modelled. As can be seen in Figure 2.19, the diffusion boundary layer is changed when the altered diffusion coefficient of the frustule is taken into account. It is not fully understood whether the transport of particles through diatom valve pores is mainly as a result of diffusion or advection. Furthermore, if advection is an important part of the transport phenomena, it is not clear whether this is dictated by crossflow or dead-end filtration. Crossflow is more likely because of hindrance

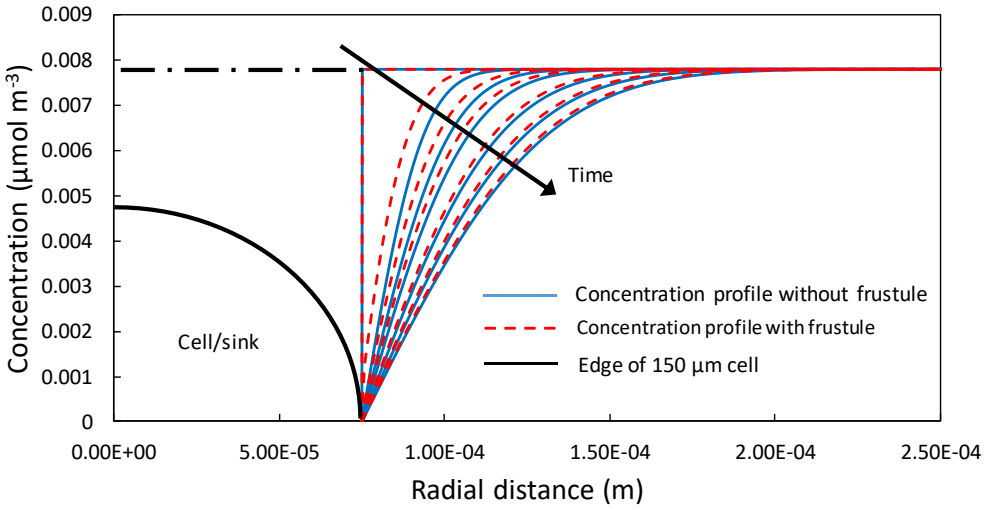

Figure 2.19 (Red dashed lines) Concentration curves changing in one dimension over $1s$ for the case of a cell with a frustule. The frustule is modelled as a $1\mu m$ region of $D = 1 \times 10^{-11}$ (Blue solid curves) Concentration curves changing in one dimension over $1s$ for the case of a cell without a frustule. The free-space diffusion is $D = 1 \times 10^{-9}$.

of flow directly through the pores by the cell inside the frustule. The direct effect of the crossflow will be to replenish the diffusion boundary layer, as previously discussed, and to also possibly manipulate particles over the external valve surface, which will be discussed in the next section. The characteristic time for diffusion across the length of the valve pores is approximately 1×10^{-3} s. There would not necessarily be any benefit from advection within the pore depending on the limiting uptake rate of the cell membrane unless it was to filter nutrients from harmful entities.

2.4.4 Influence of External Frustule Surface on Mass Transport

As previously described, two mechanisms exist in nature for generating relative flow between diatoms and the ocean; turbulence and sinking. These relative flows generate a crossflow over the external surface of the frustule, meaning a rough porous surface structure would affect the diffusion or advection of matter.

The porous and microscopic nature of the diatom frustule means it has a high surface area to volume ratio. This means that frustule surface-particle interactions become significant when assessing the controlling, sorting and separation characteristics of the frustule. Using AFM and SEM imaging techniques, Losic et al. (2009) identified microscopic features on the frustule surface including raised ridges around the foramen pores and the small hillock

topography of the external sieve plate of *Coscinodiscus sp.* Prior to the study highlighting the importance of the frustule surface from Losic et al. (2009), Hale and Mitchell (2001a) conducted phenomenological experiments, where advecting and diffusing microparticles were observed over a frustule valve. Figure 2.20 shows localised concentration of particles around the ridges of a valve of two centric diatom species; *Coscinodiscus sp.* and *T. eccentrica*, with only diffusion present (Hale and Mitchell (2001a)).

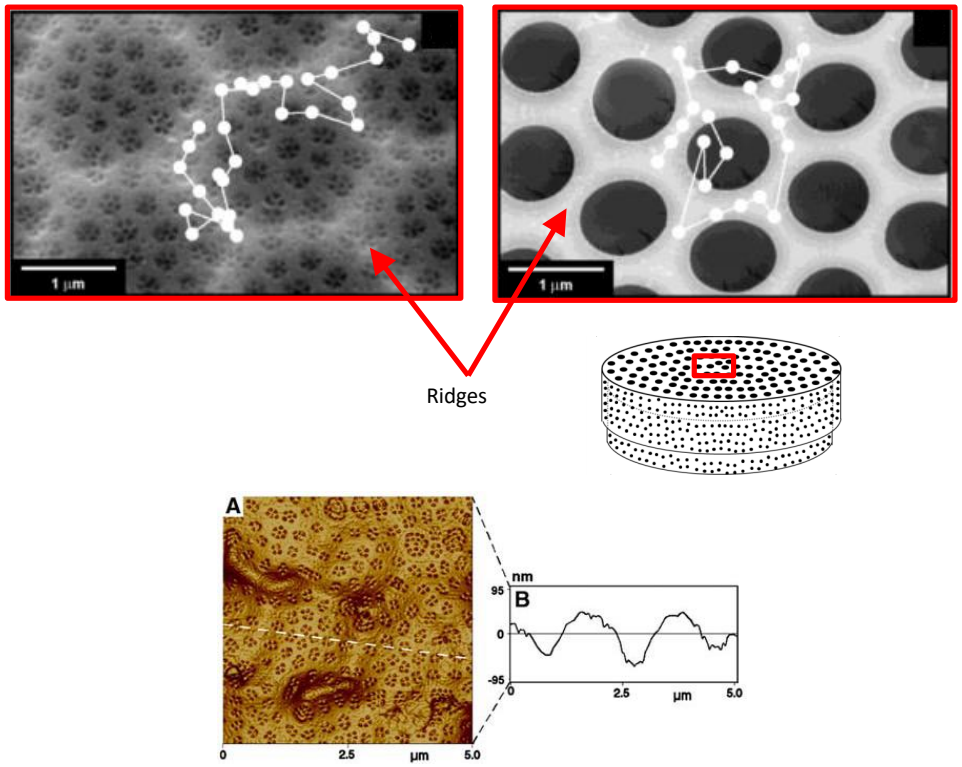

Figure 2.20 Top: Diffusion of a microsphere over the ridges of the valves of *Coscinodiscus sp.* (top left) and *T eccentrica* (top right). The scalebar is $1\mu m$. Adapted with permission from Hale MS, Mitchell JG. Motion of Submicrometer Particles Dominated by Brownian Motion near Cell and Microfabricated Surfaces. Nano Letters 2001;1:617-23. Copyright 2001 American Chemical Society. Bottom: A) AFM image of the outer surface, cribellum layer, of the diatom Coscinodiscus sp. (Losic et al. (2007a)) B) profile across the dotted line on A. Springer Losic D, Pillar RJ, Dilger T, Mitchell JG, Voelcker NH. Atomic force microscopy (AFM) characterisation of the porous silica nanostructure of two centric diatoms. Journal of Porous Materials 2007;14:61-9, Copyright Springer Science+Business Media, LLC 2006. Reprinted with permission of Springer.

The behaviour of the microparticles can be attributed to surface-induced drag and it confirmed the importance of the dimensionless parameter; particle-to-pore radii ratio (Hale and Mitchell (2001b)). A small ratio resulted in particles spending more time over the ridges, shown in

Figure 2.20. Hale and Mitchell (2001b) have promoted the idea of the diatom frustule surface possibly being used as a passive filtration system, noting the effect of surface features on the behaviour of different sized particles.

When crossflow was applied over the valve surface to represent the relative flow aforementioned, the particle behaviour; such as lateral deflection, flow reversal and particle velocity was dependent on the far-field flow velocity, surface microtopography and the size of the particle (Hale and Mitchell (2002)).

A phenomenological relationship between the lateral deflection of a spherical particle and Péclet number (*Pe*) was established for flow over the surface of a diatom valve. A bead in flow dominated by diffusion ($Pe < 1$) has more lateral deflection than that dominated by advective transport ($Pe > 1$) (Hale and Mitchell (2002)).

Typical *Pe* quoted by Karp-Boss et al. (1996) for phytoplankton, with reference to Smayda (1970) are $Pe \approx 5.7 - 24$ using a characteristic length of the diatom radius. However, due to the intermittency of this fluid advection due to turbulence or sinking events, there will be times of diffusion dominated flow ($Pe < 1$). The increase in residence time of microparticles around the edge of pores due to changes in surface-induced drag may influence the chances of particles entering pores and eventually diffusing towards the cell.

For future testing, quantitative flow visualisation techniques used by Stroock et al. (2002) were suggested to better understand the flow over diatom frustules and also potentially help derive a theoretical model which predicts this behaviour (Hale and Mitchell (2002)). However, this has not yet been completed.

2.4.5 Mass transport through the girdle band pores

Although the mass transfer through the girdle bands could be dictated by restricted / hindered diffusion through a porous membrane as previously discussed; Losic et al. (2009) has also suggested that the geometry of the girdle band pores of *Coscinodiscus sp.* are similar to that of a hydrodynamic drift ratchet. A hydrodynamic drift ratchet uses an oscillating fluid flow within an asymmetric / axisymmetric pore to separate microparticles embedded within that fluid based on their size, without net displacement of the fluid (Kettner et al. (2000)). A drift ratchet must operate at the microscopic scale where Brownian motion becomes significant and where the fluid flow is characterised by a low Reynolds number ($Re << 1$) (Kettner et al. (2000); Matthias and Muller (2003)). Based on the comparison between the geometry of the girdle band pores and that of hydrodynamic drift ratchets it was suggested that the diatom may employ the same mechanism for selective transport of matter towards and away from the diatom cell based on a particle's size.

As Figure 2.13 shows, these girdle band pores are located in the mid-section of the frustule,

between the valves. The girdle band region dominates the total surface area of the frustule of a centric diatom and is therefore important in mass transport to and from the cell.

Although there may exist similarities between the drift ratchet pores defined by Matthias and Muller (2003) and the girdle band pores of the diatom *Coscinodiscus sp.*, there also exist differences driving this research. As shown in Figure 1.2 and Table 2.1:

- The diatom girdle band pores are more than ten times smaller than the drift ratchet pores studied by Kettner et al. (2000), Matthias and Muller (2003) and Mathwig et al. (2011b).
- The girdle band pores only have a maximum number of two repeating units in series compared to the 17-33 in series for the massively parallel drift ratchet membrane (Figure 1.2 – Top),
- The oscillating fluid frequency and amplitude in a diatom will be significantly different to those studied in larger ratchets.

Table 2.1 Comparison of the pore profile geometry between the drift ratchet studied by Kettner et al. (2000); Matthias and Muller (2003) and a girdle band pore. The profiles of each are shown in Figure 1.2.

Geometric feature	Drift ratchet	Girdle band
Max. diameter	$\approx 4\mu m$	$\approx 0.25\mu m$
Min. diameter	$\approx 1.5\mu m$	$\approx 0.1\mu m$
Length of a repeating unit	$6\mu m$	$0.5\mu m$
No. of repeating units in series	17-33	1-2

If the girdle band pores act as a drift ratchet then what fluctuations are driving this mechanism in diatoms? Oscillations in external pressure derived from the sinking or rotation of the diatom or ocean turbulence, shown in Figure 2.7, or possibly oscillations in internal pressure from changes in the shape of the cell membrane dictated by turgor pressure? Table A.3, in Appendix A, summarises the scope of the research that has taken place already with respect to hydrodynamic drift ratchets. However, Chapter 4 outlines that it is unlikely that diatoms utilise the drift ratchet mechanism to sort and control ions used for growth from harmful particles like viruses. A new theory is then proposed, that instead of using the drift ratchet, they employ diffusiophoresis to prevent virus infection. The new term given to this protection is “hydrodynamic immunity”. This will be further elucidated in Chapter 4.

2.5 Objectives, Scope and Outline

Considering that the literature review has highlighted a shortfall in incorporating the effect of the frustule with respect to the uptake of nutrients and trace elements from harmful entities, such as pathogens, poisons and pollutants. This study will focus on whether the girdle band pores act as a drift ratchet. With that, there exists a very present need to demonstrate a drift ratchet experimentally and verify the mechanism using experiments. As such the following questions will be asked and the answers sought.

1. Does the diatom, *Coscinodiscus sp.*, use the drift ratchet phenomenon to sort trace elements from harmful particles based on size? If so, what parameters affect the size based filtration?

2. Due to inconclusive results from past hydrodynamic drift ratchet experiments, can a novel experiment be designed and fabricated to prove the drift ratchet mechanism exists?

3. During these experiments, can data be obtained regarding the main cause for this drift ratchet mechanism? That is, the behaviour of advecting particles when interacting with the pore wall. This could be used to improve theoretical drift ratchet models.

4. Can a dimensionless scaling relationship be demonstrated for a numerical drift ratchet model?

The aim of this project will be achieved by completing numerical and experimental analyses.

- The numerical simulations, to address research questions 1 and 4, are split into three stages; model validation, scalability analysis and girdle band simulation. First, a comparison of results from this study's numerical simulation to that of Kettner et al. (2000) is completed under the same parametric conditions to verify the numerical model. Once verification is complete, dynamic similarity for a drift ratchet is demonstrated (Question 4 – Chapter 3). Finally, the scenario of the girdle band pores is assessed to determine whether they exhibit the drift ratchet mechanism using the numerical model developed (Question 1 – Chapter 4).

- Experiments, to address research questions 2 and 3, are divided into two stages; microfluidic chip fabrication and the drift ratchet experiments. The results from the experiment will be compared to results from the developed numerical model, as well as experimental results from the past studies; Mathwig et al. (2011b) and Matthias

and Muller (2003). In particular, research question 3 will be addressed using a novel fabrication method for a drift ratchet membrane, using a three-dimensional planar drift ratchet pore described fully in Chapter 5.

Chapter 3

Numerical Simulations of Hydrodynamic Drift Ratchets

There have only been a few experimental studies of hydrodynamic drift ratchets (Kettner et al. (2000); Mathwig et al. (2011b)) and their results are contradictory due to design flaws. As such, experiments assessing particle separation capabilities of drift ratchets are required to validate numerical simulations, confirm the existence of the ratcheting mechanism, understand the importance of hydrodynamic interactions, and to eventually develop commercial particle separation devices.

To further explain the drift ratchet mechanism and assess how it scales a numerical model describing the motion of a Brownian particle in an infinite drift ratchet pore was developed. This model drew inspiration from Golshaei and Najafi (2015) using hard core interactions between finite radius particles and the pore wall, coupled with a spatially-varying diffusion coefficient. This was then combined with the approximate flow field, calculated using a similar method as that from Kettner et al. (2000) as shown in Section 3.2.1.

3.1 Hydrodynamic Drift Ratchet: The Story So Far

A hydrodynamic drift ratchet is a micro/nano fluidic device consisting of oscillating zero-mean fluid flow in a series of periodic ratchet-shaped pores, Figure 3.1, which generates rectified motion of finite-sized colloidal Brownian particles (Kettner et al. (2000); Mathwig et al. (2011b); Matthias and Muller (2003)). They have received considerable attention over the past decade due to their intriguing non-equilibrium thermodynamic properties and myriad of potential applications (Eijkel and van den Berg (2005); Eijkel and van den Berg (2006); Kettner et al. (2000)).

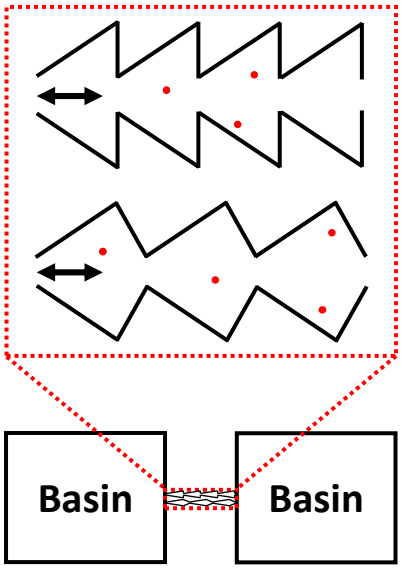

Figure 3.1 Asymmetric, ratchet-shaped pore profiles, with the arrows indicating oscillating fluid motion (Herringer et al. (2017)).

Drift ratchets operate at nano- to microscopic spatial scales where Brownian motion is a dominant transport mechanism, and convert random thermal motion into directed particle motion. Whilst such disordered diffusion may not be expected to generate mean particle flux due to the Second Law of Thermodynamics, these systems are driven far from thermal equilibrium, and therefore may be considered as open weakly dissipative systems. Based on past studies (Golshaei and Najafi (2015); Kettner et al. (2000); Martens et al. (2013); Schindler et al. (2007)), rectified particle transport arises from a combination of irreversible Brownian motion and symmetry breaking due to hydrodynamic interactions between the advecting particle and asymmetric ratchet walls. The rectified rate of movement in one direction along the pore axis is commonly termed the drift velocity. The drift velocity magnitude and direction are dependent upon a combination of the basic particle physical properties (e.g. size and shape) and ratchet geometry. Hence - if designed and tuned correctly - the drift ratchet is capable of continuous particle separation on the basis of small differences in basic particle properties alone.

Particle separation is a critical step in many micro/nano fluidic applications and lab-on-a-chip devices and these drift ratchets offer a unique and fundamentally simple technique for it. Also, if the mechanism of separation is understood properly, it may subsequently lead to further insights into transport in biological systems, like that tackled in Chapter 4 (Losic et al. (2006); Yang et al. (2011)). Yet despite the potential importance of drift ratchet applications, these have remained unexplored. A lack of efficient accurate quantitative models for the

prediction of the drift velocity and most importantly the lack of experimental confirmation are the issues limiting further progress in this field.

In addressing the lack of experimental confirmation, the computational results of Kettner et al. (2000) were experimentally replicated at a qualitative level by Matthias and Muller (2003), who observed unidirectional drift of spherical particles in a massively parallel drift ratchet membrane driven by an oscillatory pressure-driven flow. These experiments appeared to verify the numerical results of Kettner et al. (2000) and clarify the influence of the fluid oscillation amplitude upon drift current. This was done by comparing the average drift velocity of particles in simulations with the measured change in concentration of fluorescent microparticles in the experiments. More recently, however, work by Klaus and colleagues (Mathwig et al. (2011b)) attempted to replicate the experimental results, albeit with a slightly different pore geometry. In contrast to Matthias and Muller (2003), Mathwig et al. (2011b) found that drift also occurred in straight-walled cylindrical pores. More specifically, they concluded that the particle transport was due to advection under pressure-driven oscillatory flow, inducing non-zero mean flow rather than a ratchet mechanism. Specifically, they could not confirm that the fluid volume displaced over an oscillation half period was not less than the total pore volume through the membrane, which is inconsistent with previous drift ratchet cases studied. Coupled with the non-reversible circulation effects in the basins, these observations cast doubt on the previous conclusion that particle transport is due to a ratchet mechanism. Mathwig et al. (2011b) suggested this behaviour may be generic to most pressure driven oscillatory flows, however they state that this finding does not invalidate the ratchet phenomenon, and suggest alternate experimental forcing mechanisms to avoid spurious drift. It is important to note that both Matthias and Muller (2003) and Mathwig et al. (2011b) conducted their experiments in the dilute particle regime with concentrations of the order of one particle per pore to simplify elucidation of the drift mechanism. The impact of particle-particle interactions upon performance of the drift ratchet is currently an open question that has not been explored in previous experimental and numerical studies, nor will it be addressed here.

Given the paucity of experimental work and the inconclusive nature of results to date, the focus of this chapter is to better understand the scaling behaviour of an axisymmetric hydrodynamic drift ratchet pore. Once the non-dimensional terms dictating the scalability of a drift ratchet are understood, this information can be used to aid in experimental design by exploiting the ability to extrapolate / predict results from dynamically similar experiments. To verify the scaling properties of the drift ratchet a numerical model was developed based on the Langevin equation both presented by Kettner et al. (2000) and Golshaei and Najafi (2015). Alternative studies (Ai and Liu (2008); Makhnovskii et al. (2012); Martens et al. (2011);

Reguera et al. (2012)) progressed further and were able to explain the drift ratchet mechanism via the Fick-Jacobs approximation, which is based on entropic arguments that attempt to quantify the augmented particle diffusion coefficient in confined geometries. However, the applicability of the Fick-Jacobs approximation to hydrodynamic drift ratchets is currently unresolved (Martens et al. (2013)), hence the numerical model were not based off these equations. Moreover, to resolve the hydrodynamics of a drift ratchet, Brenk et al. (2008) and Mehl et al. (2008) used a coupled finite volume scheme to fully resolve the particle-fluid hydrodynamics of a non-diffusive particle within a drift ratchet. These studies ignored Brownian motion and considered significantly larger pressure amplitudes and frequencies than previous simulations (Kettner et al. (2000)) and experiments (Mathwig et al. (2011b); Matthias and Muller (2003)). Despite being able to accurately resolve the fully coupled particle hydrodynamics in the ratchet, this method is highly computationally expensive and therefore not well-suited for large parametric studies of the ratchet phenomena presented herein.

To model the drift ratchet mechanism, a similar methodology developed by Kettner et al. (2000) and Golshaei and Najafi (2015) was followed to build upon these models. As aforementioned, one of the first numerical drift ratchet studies conducted by Kettner et al. (2000) demonstrated that both particle diffusion and particle-wall hydrodynamic interactions are necessary for rectified motion and are thus essential to model within the numerical simulations. Although Brenk et al. (2008) and Mehl et al. (2008) omit particle diffusion to initially simplify computations, Brownian motion (diffusion) plays an important role in the drift ratchet mechanism. In the absence of diffusion, particle trajectories are fully reversible over a forcing period. Thus diffusion facilitates the crossing of otherwise restrictive viscous laminar streamlines by particles.

Furthermore, for a particle-fluid system bounded by a wall, particle-wall collisions cannot occur for smooth particles as the hydrodynamic resistance diverges logarithmically as the particle-wall gap approaches zero. This reduction in diffusive motion as a particle approaches a wall can be represented by a tensorial particle diffusion coefficient (Carbajal-Tinoco et al. (2007); Happel and Brenner (2012); Perkins and Jones (1992)). This spatially varying particle diffusion coefficient must be quantified to accurately predict particle drift. Golshaei and Najafi (2015) developed a numerical model for the spatially varying particle diffusion coefficient via superposition of the particle mobility near a flat wall to mimic the ratchet geometry. Their results were for a drift ratchet pore with a unidirectional forcing protocol, not purely sinusoidal, that is not representative of the fluid flow field in a hydrodynamic drift ratchet.

Similar to the tensorial particle diffusion coefficient, when an advecting particle approaches a wall it experiences lubrication forces that diverge as the particle-wall gap tends to zero. This means that the particle never impacts with the wall but rather particle motion is strongly influenced by the pore wall. The common term for this influence is hydrodynamic interaction, and is thought to be the major factor driving rectified motion in drift ratchets.

Blanchet et al. (2009) and Kondratyev et al. (2016) studied the dynamics of the Fokker-Planck equation that describes the evolution of the particle probability distribution function (PDF), and showed that particle drift only arises when the asymptotic particle PDF is non-uniform. As such, particle drift can be associated with the accumulation and depletion of particles in the fluid flow field. More specifically, for spherical particles under the flow conditions within the ratchet, the particle velocity in the bulk fluid is divergence-free (Schindler et al. (2007)) and so particle accumulation cannot occur in this region. Whereas, the particle velocity (defined at the particle centre) near boundaries is not divergence-free due to the geometric requirement that the particle boundary cannot cross the pore boundary. Thus, it has been identified that the hydrodynamic interactions between an advecting particle and the asymmetric pore wall causes this non-uniform PDF within a drift ratchet (Schindler et al. (2007)). In fact, the hydrodynamic interactions induce accumulation and depletion of particles at converging and diverging ratchet walls, respectively, leading to rectified particle motion. Rectified motion in the drift ratchet is thus thought to be persistent particle accumulation that arises from the combination of advecting particle lubrication dynamics and particle diffusion.

This chapter seeks to uncover the scaling behaviour of the drift ratchet; namely how the particle drift velocity and dispersion scale (diffusion coefficient ratio) as a function of the ratchet geometry and forcing parameters. As well as evaluating the dynamic similarity of a drift ratchet, this chapter will also determine the effect of a spatially varying diffusion coefficient in a hydrodynamic drift ratchet.

Ideally one would like to develop a model which can fully predict the particle motion based upon the two-way hydrodynamic coupling (such as Stokesian Dynamics), however it must be noted that whilst significant developments have been made very recently regarding Stokesian Dynamics (Swan and Brady (2011)) for a suspension confined by planar walls, these methods are not applicable to walls of constant or arbitrary curvature. Indeed, the solution to Stokes flow around a spherical particle in the presence of arbitrary shaped walls remains an outstanding problem fundamental to Stokesian fluid dynamics. This work only seeks to recover the correct scaling behaviour of the drift ratchet, as such a much simpler particle-wall interaction can be employed, which is based on one-way coupling between the particle and fluid, namely the reflection boundary conditions employed by Kettner et al.

(2000) and others (Golshaei and Najafi (2015); Matthias and Muller (2003)) in foundation studies of the drift ratchet. Whilst this boundary treatment does not recover the correct hydrodynamic interactions, it must be noted that this reflection condition is based upon Stokes fluid flow in the absence of particles, and the reflection boundary treatment itself is linear with respect to this velocity field. As both the particle Brownian dynamics and the two-way coupled flow field are linear, the simplified treatment inherits the same scaling behaviour as the full hydrodynamic problem even though the predicted drift velocity may contain errors. As such this simplified one-way model will be used to study the scaling behaviour of the drift ratchet and elucidate the governing mechanisms.

3.2 Model Development

3.2.1 Particle Hydrodynamics

The spatial displacement of a Brownian particle in the bulk of a viscous fluid flow (Burada et al. (2009)) over a time step Δt is described by the overdamped Langevin equation,

$$\boldsymbol{x}_{particle}(t) = \boldsymbol{x}_{fluid}(\boldsymbol{x}(t),t) + \sqrt{2D_{th}\Delta t}\boldsymbol{\gamma} \tag{3.1}$$

where $\boldsymbol{x}_{particle}(t)$ and $\boldsymbol{x}_{fluid}(\boldsymbol{x}(t),t)$ are the displacements of a Brownian particle and the fluid respectively, $D_{th} = k_B T/6\pi r\mu$ is the free-space particle diffusivity, Δt the time step and $\vec{\gamma}$ is a Gaussian random variable with unit variance (Kettner et al. (2000)). The drift ratchet simulation uses a progressive code in MATLAB to calculate the displacement of the particle resulting from a random Brownian force and drag force from the fluid advection, at each time step. Generally, to reduce truncation error the time step is reduced to accurately simulate the dynamics of the governing equation. In the absence of fluid flow, the numerical solution of Equation 3.1 over an ensemble of 100 particles recovers the particle mean square displacement associated with the constant particle diffusion coefficient. The ensemble statistics were found to be independent of time step for $\Delta t \leq 10^{-6}s$, hence $\Delta t = 10^{-6}s$ was used in the numerical model. Dilute particle concentrations and a large number of repeating ratchet units in series were assumed, meaning both particle-particle interactions, and the effect of finite pore length and basins at either end of the ratchet can be neglected.
The axisymmetric, steady fluid velocity field $v_0(x) = \nabla \times \left(\frac{\Psi}{r} e_\theta\right)$ is approximated using the stokes stream function,

$$\Psi(r,z) = -\frac{1}{2}\left(\frac{r}{r_p(z)}\right)^2 + \frac{1}{4}\left(\frac{r}{r_p(z)}\right)^4 \tag{3.2}$$

where r and z are the radial and axial coordinates, respectively, inside the pore wall described by $r_p(z)$. The accuracy of this analytical assumption is shown in Figure 3.2 where the velocity profile at two cross sections of the pore are compared against Computational Fluid Dynamics (CFD) solutions.

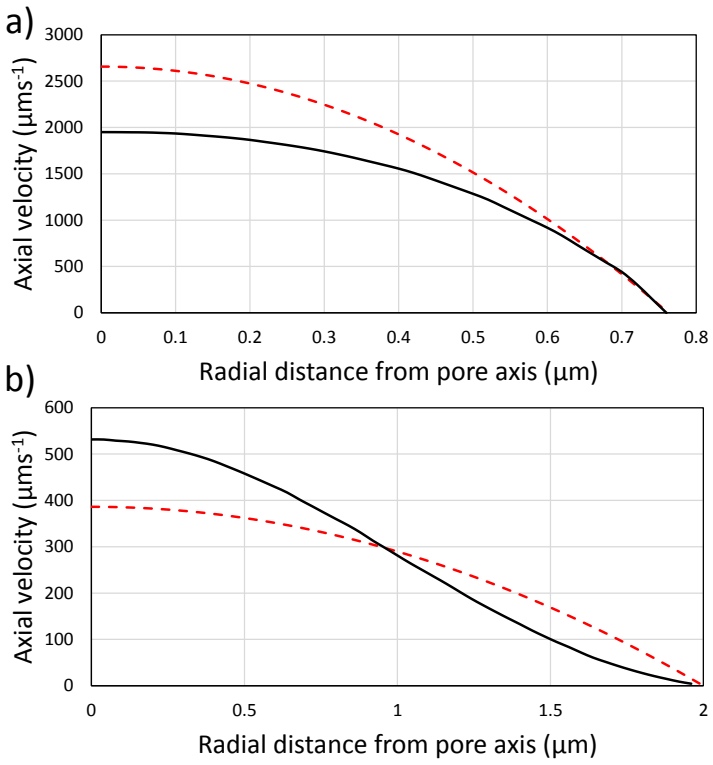

Figure 3.2 Fluid velcocity profile at the a) minimum and b) maxiumum pore diameter. (Red/dotted line) Velocity using analytical method based on Equation 3.2. (Black/solid line) Velocity using CFD. The flow rate was similar between the two positions for the CFD simulation and analytical methods, i.e. conservation of mass was satisfied.

This analytical approximation for the fluid flow field is valid for small perturbations of the pore radius compared against its axial length. This assumption is satisfied by the below equation for the drift ratchet pore wall studied by Kettner et al. (2000).

$$r_p(z) = \frac{1}{2.1}\left[2.9 + \sin(2\pi z/6 - \pi/3) + \frac{1}{2}\sin(2\pi z/3 - 2\pi/3)\right] \tag{3.3}$$

In the cases explored in this study the Strouhal number is less than 10^{-1} and therefore the transient fluid velocity field can be represented by the separable equation,

$$\boldsymbol{v}_{fluid}(\boldsymbol{x}(t),t) = \boldsymbol{v}_0(\boldsymbol{x}(t))g(t) \tag{3.4}$$

where $g(t) = sin(\omega t)$ is the time dependent component in the case modelled herein.

As the particles are neutrally buoyant, have negligible Stokes number and the particle and fluid Reynolds numbers are both negligible, the only mechanism for particles to deviate from fluid trajectories is via particle-wall hydrodynamic interactions and Brownian motion. Other mechanisms such as added mass, buoyancy, lift and Basset forces in the ratchet are also negligible. The impact of particle motion upon the fluid field can also be shown to be negligible, hence oneway coupling was only considered between the fluid and particles, as reflected by Equation 3.1. Under the approximation of a point particle, the fluid velocity at the centre of the particle was used in the first term of Equation 3.1, and the rotation of a particle as a result of fluid shear is not considered.

3.2.2 Capturing Augmented Diffusivity

To study the impact of spatially-variable particle diffusivity due to reduced particle mobility near the pore wall, simulations with a constant diffusion coefficient D_{th} were initially performed prior to introducing a tensorial diffusion coefficient $D_V(x(t))$. Due to lubrication forces, this diffusivity approaches the free-space diffusivity for large values of the particle-wall gap h and decays to zero as h approaches the particle radius a. As the lubrication forces are anisotropic, the resultant particle diffusivity is tensorial. For a particle undergoing diffusion in the presence of an isolated planar wall, the parallel $D_{\parallel}(h)$ and perpendicular $D_{\parallel}(h)$ components of which are (Happel and Brenner (2012); Perkins and Jones (1992))

$$\frac{D_{th}}{D_{\parallel}(h)} = 1 - \frac{8}{15}\ln(1-\beta) + 0.029 + 0.04973\beta^2 - 0.1249\beta^3 + ... \tag{3.5}$$

$$\begin{aligned}\frac{D_{th}}{D_{\perp}(h)} = \frac{4}{3}\sinh(\alpha)\sum_{n=1}^{\infty}\frac{n(n+1)}{(2n-1)(2n+3)}\times \\ \left[\frac{2\sinh(2n+1)\alpha + (2n+1)\sinh 2\alpha}{4\sinh^2(n+\frac{1}{2})\alpha - (2n+1)^2\sinh^2\alpha} - 1\right]\end{aligned} \tag{3.6}$$

where $\beta = a/2h$ and $\alpha = \cosh^{-1}(2h/a)$. Both of these relationships have recently been verified experimentally (Carbajal-Tinoco et al. (2007)) for colloidal particles diffusing near a planar wall, the problem of diffusion in the presence of curved walls has received little

attention and is still an outstanding problem in fluid mechanics. When the lateral κ_{radial} (m^{-1}) and longitudinal κ_{axial} (m^{-1}) curvature of the pore wall are negligible compared to that of the particle, $\frac{1}{r(z)} = \kappa_{radial} \gg \frac{1}{a}$, $\kappa_{axial} \gg \frac{1}{a}$, the isolated flat wall relationships Equations 3.5 and 3.6 accurately approximate the particle diffusivity in the ratchet, where h is the smallest particle-wall spacing. The maximum curvature of the wall along the longitudinal direction of the pore is less than the particle curvature, $1.4m^{-1} < 2.9m^{-1}$. The curvature in the lateral direction follows a similar behaviour, $1.3m^{-1} < 2.9m^{-1}$. Clearly in this case the curvatures are similar in magnitude and so the validity of this assumption is unclear.

The spatially-varying diffusion coefficient for the drift ratchet case is shown in Figure 3.3.

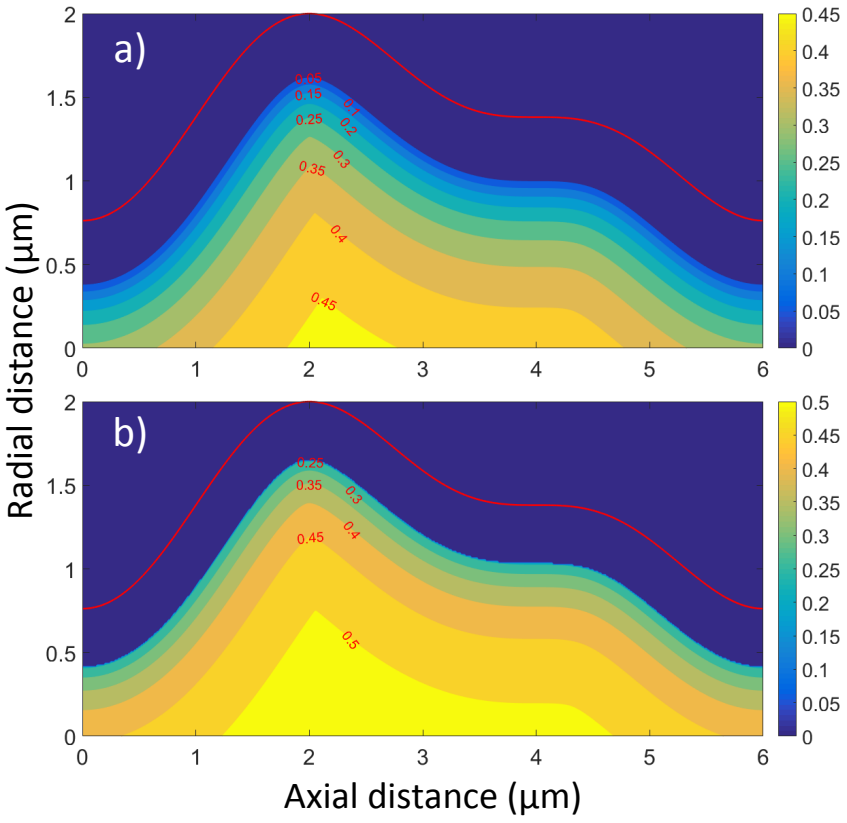

Figure 3.3 a) Diffusivity perpendicular to the pore wall using Equation 3.5. b) Diffusivity parallel to the pore wall using Equation 3.6. The free diffusion coefficient used was $0.5982\mu m^2 s^{-1}$ and particle radius of $0.35\mu m$. The units for the spatially-augmented diffusivity is $\mu m^2 s^{-1}$ (Herringer et al. (2017)).

3.2.3 Particle-Wall Interactions

Rectified particle motion is generated by the combination of particle diffusion and the hydrodynamic interactions between an advecting particle and the pore wall, as summarised in Section 3.1. To study the scaling properties of the drift ratchet these interactions using a simplified model illustrated in Figure 3.4 were simulated.

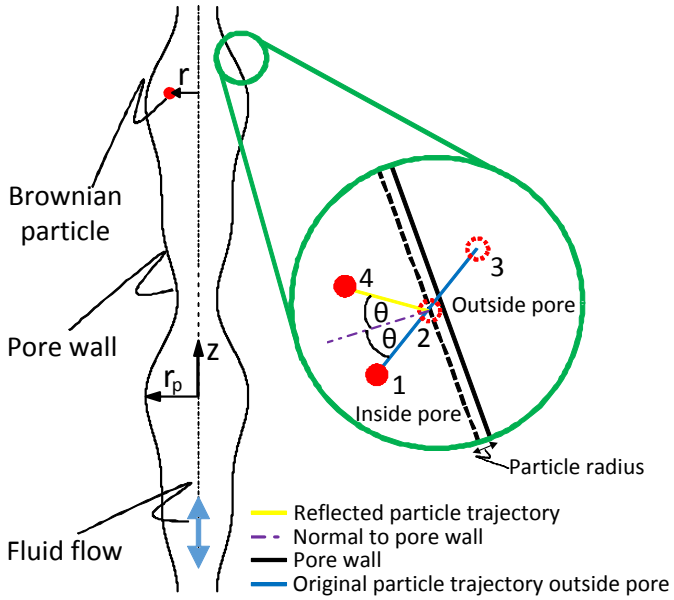

Figure 3.4 Schematic of the particle-wall interactions used in this numerical model (Herringer et al. (2017)). The lengths 2-3 and 2-4 are equal. The geometry of the pore is that studied by Kettner et al. (2000).

Here particles are advected by the fluid velocity and diffuse via Brownian motion as per the overdamped Langevin Equation 3.1. While particle-wall collisions (arising from either advective or diffusive motion) cannot occur for smooth particles as the hydrodynamic resistance diverges logarithmically as the particle-wall gap approaches zero, Equations 3.5 and 3.6, in the same vein as Kettner et al. (2000), the particle-wall hydrodynamic interactions were modelled via a reflective boundary condition which qualitatively recovers the same particle clustering behaviour as the complete hydrodynamic interactions. The gross effect of this reflective boundary condition is that it augments the particle PDF near the ratchet walls in a manner that is dependent upon the wall orientation with respect to the fluid streamlines. Specifically, the reflection condition tends to accumulate particles on converging walls and likewise deplete particles on diverging walls, hence the qualitative impact of this condition is similar to that of the true particle-wall hydrodynamic interactions. This reflection condition

also recovers the property that the drift velocity decays to zero with decreasing particle size. Whether the reflection condition is quantitatively representative of the full hydrodynamic interaction is currently an open question.

3.2.4 Dimensionless Parameters

To develop scaling arguments for the drift ratchet, the following dimensionless parameters were defined, which are kept constant over the different ratchet sizes: the Péclet number Pe, which captures the relative advection and diffusion timescales, the Strouhal number St, which characterises the relative viscous and forcing timescales, the ratio of particle to pore size α, and the non-dimensional fluid flow amplitude β.

$$Pe = \frac{v_{max} d_{min}}{D_{th}} \tag{3.7}$$

$$St = \frac{d_{min}}{T v_{max}} \tag{3.8}$$

$$Pe = \frac{a}{d_{min}} \tag{3.9}$$

$$Pe = \frac{T v_{max}}{A} \tag{3.10}$$

v_{max} is the maximum fluid velocity within the pore which occurs at the minimum pore diameter d_{min}, T is the period of fluid oscillation, a is the diameter of the particle and A is the distance fluid travels along the centreline of the pore over half a period of oscillation. The remaining dimensionless number is the Reynolds number, Re, which is typically less than unity in microfluidics, corresponding to laminar and reversible flow (the maximum Reynolds number in this study was approximately 10^{-2}). However, it is important to note that fluid recirculation regions can occur within the drift ratchet, even at low Reynolds numbers for certain pore geometries. Such recirculation does not arise for the small smooth undulations of the pore geometry studied herein (Islam et al. (2015)). Inertial effects associated with acceleration of the oscillating fluid may be considered negligible if the viscous timescale $\tau = d_{min}^2/\nu$ ($\approx 10^{-5} s$) is smaller than the fluid forcing period T. This ratio is given by the product of the Reynolds and Strouhal numbers, both of which are small, justifying separability of the temporal velocity field, Equation 3.4. The product $StRe$ results in this ratio of viscous timescale to forcing period. The Reynolds number and Strouhal number are small and therefore inertial effects due to the oscillations can be neglected.

3.2.5 Model Validation

The parameters used in the drift ratchet simulations are summarised in Table 3.1. The two cases of ratchet operation investigated by Kettner et al. (2000) were considered: in Case 1 the fluid displaced along the centreline of the pore, in half an oscillation period is equal to a single ratchet unit length, whilst under Case 2 the fluid displaced is double the ratchet unit length.

Table 3.1 Parameters used in validation of the drift ratchet simulations (Kettner et al. (2000)).

Parameters	Case 1 (1x amplitude)	Case 2 (2x amplitude)
Fluid amplitude (A)	6μm	12μm
Flow rate (Q_z)	$2426.5\mu m^3 s^{-1}$	$4853\mu m^3 s^{-1}$
Fluid frequency (f)	$40Hz$	
Viscosity (μ)	$0.5\mu_{water}$	
μ_{water}	$1.025 \times 10^{-3} Nsm^{-2}$	
Temperature (T)	$293K$	
Particle radius (r)	$0.35\mu m$	
Boltzmann constant (k_B)	1.38×10^{-23} m^2.kg.s^{-2}.K^{-1}	
Minimum pore diameter (d_{min})	$1.52\mu m$	
Reynolds number (Re)	Less than 0.008	
Stokes number (Stk)	1×10^{-2}–1×10^{-4}	

To verify the drift ratchet model the calculated average particle drift velocity, v_e,

$$v_e = \frac{\langle z(t_{run}) \rangle}{t_{run}} \tag{3.11}$$

and effective diffusion coefficient, D_e,

$$D_e = \frac{\langle z^2(t_{run}) \rangle - \langle z(t_{run}) \rangle^2}{2t_{run}} \tag{3.12}$$

are compared to those calculated by Kettner et al. (2000), where $z(t_{run})$ is the displacement along the axis of the pore over a time period t_{run} and $\langle \cdots \rangle$ denotes the ensemble average over 100 particles. Typical motion of an ensemble of particles for the 1x and 2x amplitude cases outlined in Table 3.1 are illustrated in Figure 3.5. These results indicate that a doubling of the oscillation amplitude results in reversal of the mean transport direction. The calculated mean drift and diffusion values are shown in Table 3.2, illustrating that the results compare

well with those of Kettner et al. (2000).

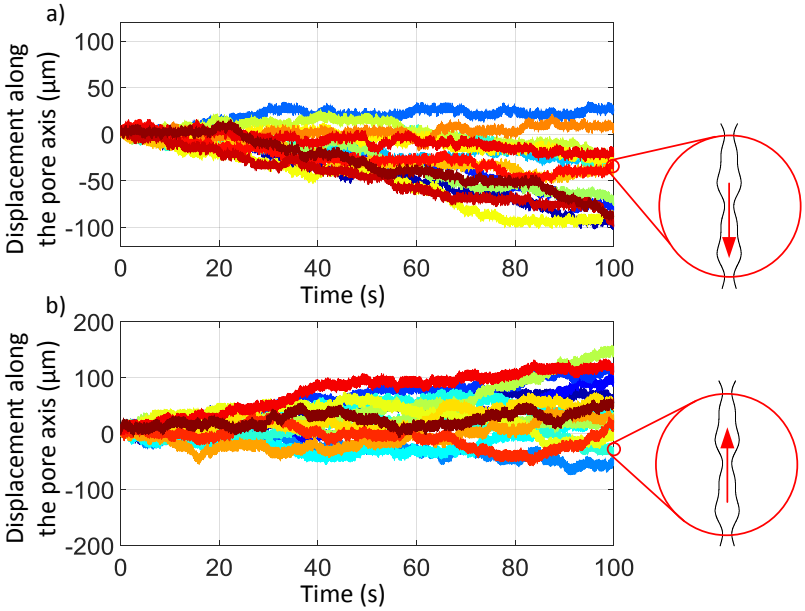

Figure 3.5 Displacement of 15 random particles as a function of time (Herringer et al. (2017)). a) 1x amplitude and b) 2x amplitude as per Table 3.2.

Table 3.2 Comparison of the average drift velocity and effective diffusion coefficient between this model and Kettner et al. (2000) for case 1 and case 2, averaged over 100 particles. A negative drift velocity represents particles moving downwards in Figure 3.5.

	Case 1 (1x amplitude)			Case 2 (2x amplitude)	
Numerical models	This model (Velocity field approximated by analytical solution)	This model (CFD solved velocity field)	Kettner et al. (2000)	This model (Velocity field approximated by analytical solution)	Kettner et al. (2000)
v_e (μms^{-1})	-0.41	-0.44	-0.46	0.39	0.45
D_e/D_{th}	3.12	2.5	2.45	9.6	-

The discrepancy in the validation results above could be attributed to the different representations of the particle-wall interactions, and/or the approximation of the fluid flow, or not averaging the fluid velocity over the volume of the particle in this model. The higher effective diffusion coefficient in the 2x amplitude case, even though it has a smaller or

equivalent drift velocity compared to that in the 1x amplitude case, shows higher variance in total axial displacements over the same time period.

3.3 Particle Behaviour

It has recently been demonstrated (Martens et al. (2013); Schindler et al. (2007)) that in the absence of hydrodynamic interactions between the particles and the pore walls, the equilibrium adiabatic particle probability distribution function (PDF) is uniform across an asymmetric pore, hence the drift velocity is zero. Whilst the particle reflection boundary condition only captures these hydrodynamic interactions in a qualitative sense, the simulations herein recover the limiting hydrodynamic behaviour that particle drift does not occur when the particle radius is zero. This is clearly shown in Figure 3.6, where particle displacement is plotted as a function of time for finite diameter particles and point particles. The only difference between a finite radius particle and a point particle is how close the centre of the particle can approach a wall.

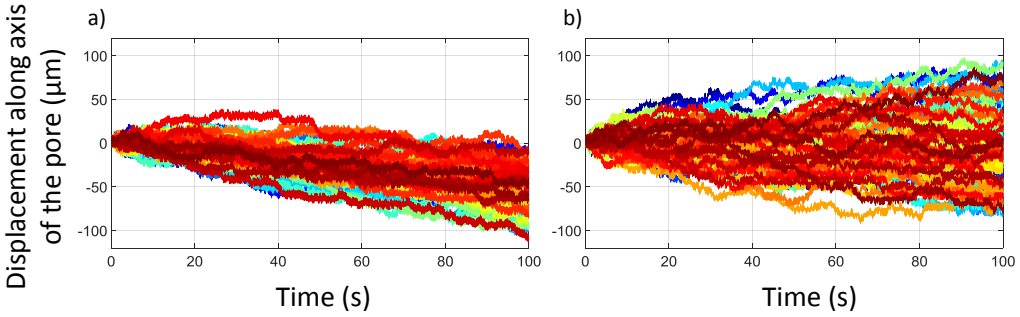

Figure 3.6 Displacement of 100 random particles as a function of time for a constant diffusion coefficient (Herringer et al. (2017)). a) Particle-wall interaction with a finite particle radius and b) Particle-wall interaction using point particle.

Point particles (zero radius) in the absence of Brownian motion follow streamlines which cannot intersect the wall. Brownian motion facilitates the traversing of particles across streamlines in an otherwise restrictive laminar flow and move towards the wall. Once finite radius particles are close enough to the wall streamlines can be crossed simply by the hydrodynamic interactions between a finite radius particle and the pore wall. It is this interaction which is necessary to generate particle drift. This concept is illustrated in Figure 3.7 that shows the motion of a finite advecting particle near a wall. A particle advecting along streamline A in Figure 3.7 is forced onto a path parallel to the pore wall at the edge of the particle exclusion zone (minimum distance from the wall the centre of a particle can

occupy due to its finite radius). After travelling through a constriction in the pore, the particle experiences a diverging pore wall and remains on a faster, straighter streamline B in Figure 3.7 (Schindler et al. (2007)).

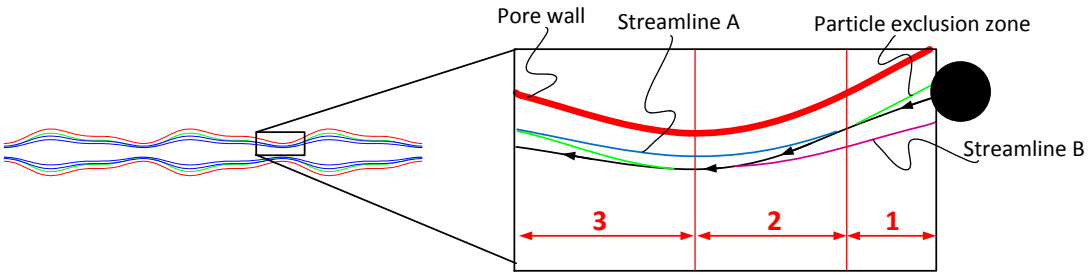

Figure 3.7 Schematic of the mechanism thought to be contributing to driving a drift ratchet adapted from Schindler et al. (2007).

So how does the reflecting boundary condition affect particle dynamics? To answer this question, the distribution of the particles within the pore, as a function of time, was examined. This is graphically represented by the particle PDF over a periodic ratchet unit in Figure 3.8. The particle PDF $\rho(x(t),t)$, averaged over 100 particles, is scaled with the local axial fluid velocity inside the pore to calculate the average drift velocity,

$$g_+(x) = \frac{1}{T}\int_0^{T/2} \rho(x(t),t)v_{fluid}(x,t)dt \tag{3.13}$$

$$g_-(x) = \frac{1}{T}\int_{T/2}^{T} \rho(x(t),t)v_{fluid}(x,t)dt \tag{3.14}$$

$$v_e = \sum g_+(x) + \sum g_-(x). \tag{3.15}$$

The summation in Equation 3.15 is over the ratchet unit area shown in Figure 3.8. Maxima of particle probability occur at the edge of the exclusion zone at 0 and 6 μm along the pore as shown in Figure 3.8. This is due to the interaction of the particles with the pore wall, moving them to a faster (inner) streamline as previously discussed. Similar to that observed in Schindler et al. (2007) it can be seen in Figure 3.8 that particles accumulate on the inside of a converging wall and disperse when the walls diverge. The particles traverse the width of the pore in the 1x amplitude case as shown in Figure 3.8(a) and Figure 3.8(c), whereas the radial migration of particles, in the 2x amplitude case, is restricted as depicted in Figure 3.8(b) and Figure 3.8(d). This restriction comes from the fact that, for the 2x case, no matter where particles are with respect to a ratchet unit the fluid advection term is large enough

to make them cross a throat of the pore, during a fluid oscillation cycle. This throat wall interaction continually constricts the particle as outlined in Figure 3.7. As seen from Kettner et al. (2000), doubling the fluid amplitude can reverse the direction of particle drift. This difference in particle position probability outlined here highlights significant differences between the two cases that can lead to drift reversal.

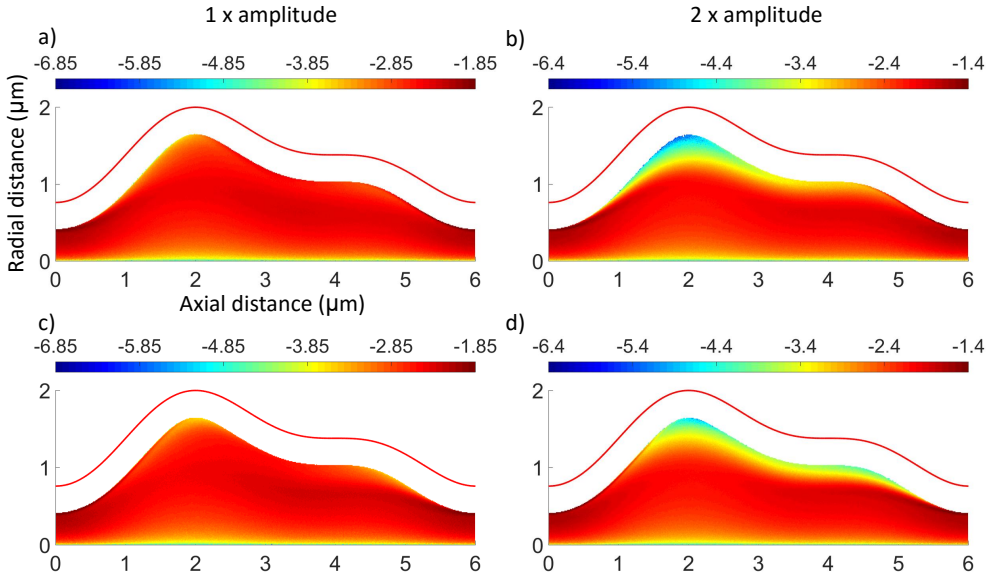

Figure 3.8 The log of the absolute particle probability distribution over a run time of 100*s* and 100 particles in a drift ratchet pore for the 1x and 2x amplitude case, left and right respectively. a) and b) represent the half of a period of fluid oscillation in the positive direction particles/fluid moving from left to right, Equation 3.13. Whereas, c) and d) is that in the negative direction, particles/fluid moving from right to left, Equation 3.14. The red curve represents the pore wall. The white region between the pore wall and the PDF plot is the particle exclusion zone (Herringer et al. (2017)).

The average drift velocity presented can be recovered from the PDFs illustrated in Figure 3.8 and is tabulated in Table 3.3.

Table 3.3 Comparison of average drift velocity from tracking particles from the numerical model, and from the PDFs in Figure 3.8

	Case 1 (1x amplitude)		Case 2 (2x amplitude)	
	Numerical model	PDFs	Numerical model	PDFs
v_e (μm.s^{-1})	-0.41	-0.41	0.39	0.28

The local Péclet number, calculated with the local fluid velocity, mass diffusion coefficient and minimum pore diameter, is shown in Figure 3.9 for the 1x amplitude case. At a time interval of $10^{-5}s$ either side of the nodes of the sinusoidal wave in Figure 3.9, the Péclet number reduces to below unity where diffusion would dominate transport of particles. This a very small percentage of the period of oscillation (0.16%) and thus the particles are dominated by advection in the drift ratchet. In the 2x amplitude case the percentage of time dominated by diffusion is halved to 0.08% of the oscillation period.

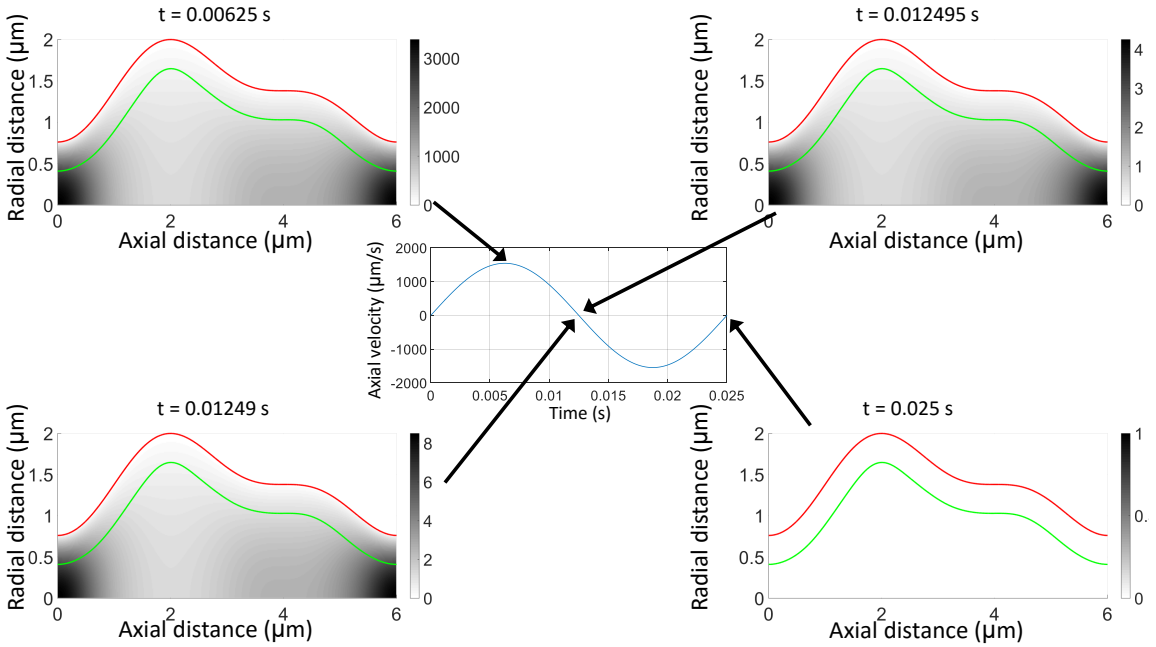

Figure 3.9 Péclet number distribution for a constant diffusion coefficient and length scale based on the minimum pore diameter for the 1x amplitude case (Herringer et al. (2017)).

3.4 Dynamic Similarity Analysis

The effect of drift ratchet size on the drift velocity and the effective diffusion coefficient at the various geometric scales relative to the pore size used in Kettner et al. (2000) have been investigated. The shape is the same as that used in the previous section and the cases are outlined in Table B.1 in Appendix B. Across these cases the Péclet number, Strouhal number, the particle/minimum pore diameter ratio and the dimensionless fluid amplitude are all constant.

3.4.1 Effect of Drift Ratchet Pore Size

The ratio between the effective and free-space particle diffusion coefficients is independent of the pore sizes as per Figure 3.10. That is the relative magnitude of diffusion to advection, as characterized by the Péclet number, and relative size of the particle with respect to the pore size, are both held constant. The increased scatter for the higher amplitude case is due to a higher velocity while keeping the time step constant across all the cases. Also included in Figure 3.10 are the results of simulations within a straight-walled cylinder to show the effect of an asymmetric pore wall.

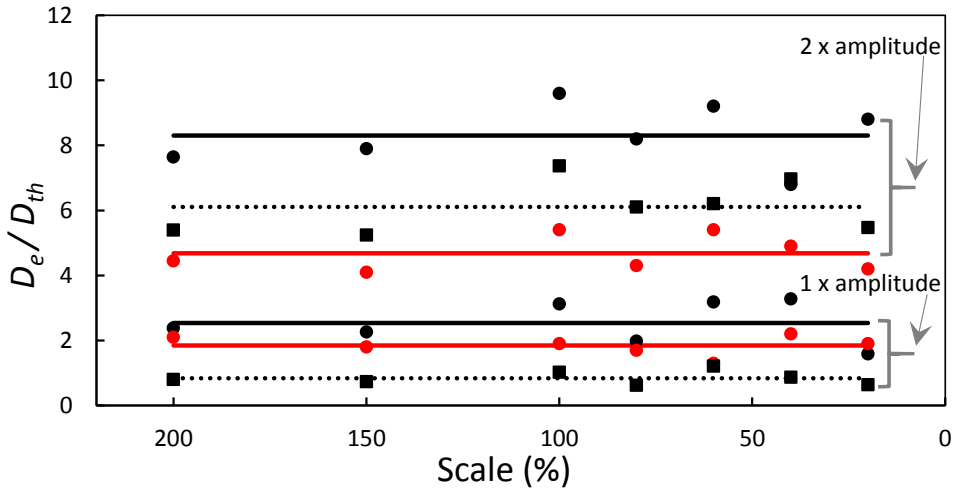

Figure 3.10 Ratio of effective to free-space particle diffusion coefficients as a function of pore size for $\Delta t = 10^{-6}s$ (Herringer et al. (2017)). The circles and solid lines represent simulations with a constant diffusion coefficient, whereas square markers and dotted lines represent spatially-varying diffusion coefficient. (Black) Drift ratchet pores and (Red) straight-walled pores (Herringer et al. (2017)).

Whilst one might expect the relative diffusion coefficient to be unity for a straight walled pore, Taylor-Aris dispersion comes into play, where Brownian particles diffuse longitudinally and radially on similar time-scales. The parabolic shape of the temporally oscillating fluid velocity field affects the effective diffusion coefficient. As expected with plug flow in a straight pore, the longitudinal dispersion is equivalent to the particle diffusivity as shown in Figure 3.11.

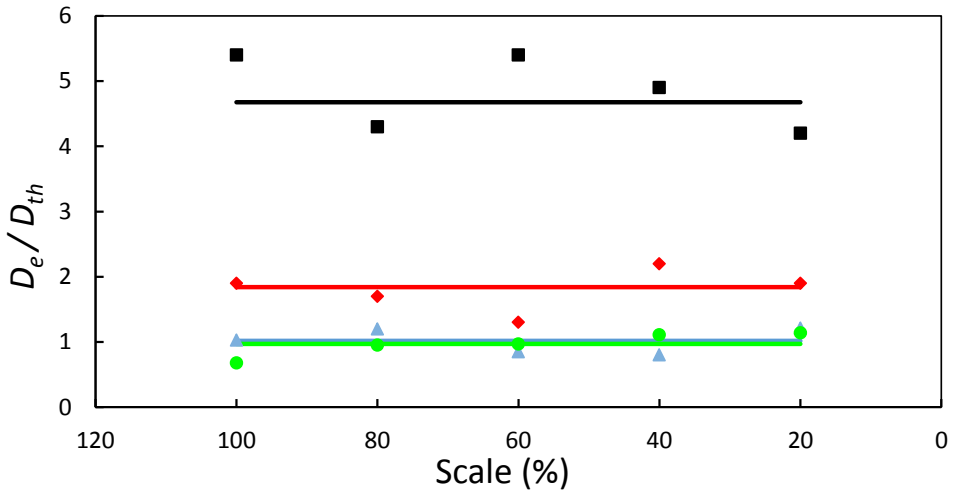

Figure 3.11 Ratio of effective to free-space particle diffusion coefficients as a function of pore size for straight-walled pores with $\Delta t = 10^{-6}s$ (Herringer et al. (2017)). (Black/square) 2x amplitude with a parabolic velocity profile, (Red/diamond) 1x amplitude with a parabolic velocity profile, (Blue/triangle) Just diffusion no fluid advection and (Green/circle) 1x amplitude with a uniform velocity profile (Herringer et al. (2017)).

In order to scale the drift velocity, v_e, with pore size a non-dimensional relative drift velocity was introduced,

$$v_{Reldrift} = \frac{T v_e}{L} \tag{3.16}$$

where T is the period of fluid oscillation, and L is the axial length of a ratchet period, and so $v_{Reldrift}$ is independent of ratchet size as shown in Figure 3.12. As expected, the drift velocity for straight walled pores is essentially zero.

3.4.2 Effect of Spatially-Varying Diffusion Coefficient

As discussed in Section 3.2, the particle diffusion coefficient is both anisotropic and spatially variable near pore walls due to particle-wall hydrodynamic interactions. As shown in Figure 3.12 there is only a minor difference between having a constant and a spatially-varying diffusion coefficient for the 2x amplitude case, reflecting the fact that diffusion is relatively weak at higher Péclet numbers. This can be explained by understanding that no matter where the particle starts a fluid oscillation cycle with respect to the pore wall, it will pass through

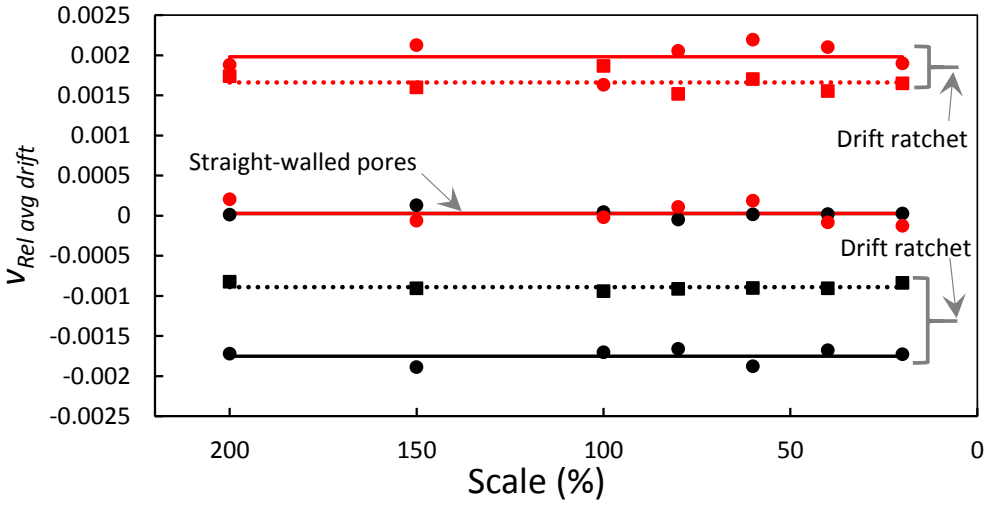

Figure 3.12 Relative drift velocity as a function of pore size for $\Delta t = 10^{-6}s$ (Herringer et al. (2017)). The circle markers and solid lines represent simulations with a constant diffusion coefficient whereas square markers and dotted lines represent spatially-varying diffusion coefficient. (Black) 1x amplitude case and (Red) 2x amplitude case (Herringer et al. (2017)).

the throat of the pore. This continuously constrains the particle into the straighter, higher velocity streamlines towards the axis of the pore, where advection dominates diffusion, and the effect of the varying pore diameter is diminished (Motz et al. (2014)). This mechanism can be observed in the 2x amplitude case in Figure 3.8. Conversely, for the 1x amplitude case, the drift velocity reduces as to be expected because the diffusion coefficient is monotonically decreasing as it approaches the wall. There is less diffusion and therefore less displacement of the particle in a given amount of time, which leads to a reduction in the ratchet effect. This effect is also apparent in the reduction in the effective diffusion coefficient in both the 1x and 2x amplitude cases. Similar to the results presented herein, Golshaei and Najafi (2015) found that the comparison to a constant diffusivity, a spatially-varying diffusivity reduces the particle current through the drift ratchet.

The variation of the constant parameters in the aforementioned plots are shown in Table 3.4.

Table 3.4 Variation in effective diffusion coefficient and relative average drift velocity for 100 particles.

	Effective diffusion coefficient		Relative average drift velocity	
	Mean	Relative standard deviation (%)	Mean	Relative standard deviation (%)
Drift ratchet 1x amplitude	2.5	±26.0	-1.8×10^{-3}	±5.3
Drift ratchet 2x amplitude	8.3	±11.6	2.0×10^{-3}	±9.8
Straight-walled pores 1x amplitude	1.8	±15.9	2.8×10^{-5}	±190.8
Straight-walled pores 2x amplitude	4.7	±11.9	2.8×10^{-5}	±479.7
Drift ratchet 1x amplitude varying diff coefficient	0.84	±25.3	-8.9×10^{-4}	±4.7
Drift ratchet 2x amplitude varying diff coefficient	6.1	±13.4	1.7×10^{-3}	±7.2

3.5 Drift Ratchet Efficiency

The work done to move a specified fluid volume over a ratchet unit length in half a period can be defined by,

$$W_{MovingLiquid} \approx \Delta P \times Q \times \frac{T_{ff}}{2} \tag{3.17}$$

$$\Delta P = -2 \int_0^L \frac{\partial^2}{\partial r^2} v_z(r=0,z)dz \tag{3.18}$$

where, ΔP (Pa) is the pressure difference across a ratchet unit length (Kettner et al. (2000)), v_z (ms^{-1}) is the fluid velocity long the pore axis, Q $(m^3 s^{-1})$ is the volumetric flow rate and T_{ff} (s) is the period of fluid oscillation.

Equation 3.19 defines the work done on N particles by the fluid being pumped back and forth

in a drift ratchet pore in half a period of oscillation, this can be calculated by summing the incremental work done on the particles i.e. summation of the product of the drag force on a particle and the incremental distance traveled by that particle.

$$W_{MovingParticles} \approx N \sum_{0}^{L} F_{Drag} \Delta s \tag{3.19}$$

Where, L (m) is the length of a ratchet unit length, F_{Drag} (N) is Stokes drag force on a spherical particle and s (m) is the incremental distance over which the drag force acts on the particle.

The energy efficiency of a drift ratchet can be estimated by comparing the above two energy terms. If $0.3\mu m$ diameter particles are assumed to be drifting in a drift ratchet pore with a particle dilution of 3% by volume, the work done on all the particles is $1.43 \times 10^{-15} J$ and the work done on the fluid is $2.30 \times 10^{-15} J$. Then the efficiency of a drift ratchet can be around 60% based on Equation 3.20.

$$\eta_{DriftRatchet} \approx \frac{W_{MovingParticles}}{W_{MovingLiquid}} \tag{3.20}$$

3.6 Summary of Findings

There is a clear need for further experimental investigation of hydrodynamic drift ratchets to: (i) corroborate initial results with numerical simulations; (ii) confirm the existence of the phenomenon and underlying mechanisms; and (iii) to assist in the development of novel applications, fabrication procedures and designs (Herringer et al. (2017)). This chapter shows that dynamic similarity of the hydrodynamic drift ratchet arises when the relevant dimensionless parameters are held constant; a direct consequence of the linearity of the governing hydrodynamics and particle dynamics under creeping flow conditions. This provides a basis for experimental design of the drift ratchet as it allows scaling of the drift velocity and longitudinal dispersion as a function of the pore geometry. This makes it easier to design drift ratchet experiments by giving us the ability to compare results between dynamically similar experiments and eventually lead to the development of drift ratchet membranes potentially for commercial use (Herringer et al. (2017)). In terms of numerical modelling, an accurate representation of the two-way coupled particle-wall lubrication dynamics is critical to the development of a predictive drift ratchet model necessary for ratchet design and optimization. However, this is beyond the scope of this research (Herringer et al. (2017)).

Chapter 4

Girdle Band Pores and Drift Ratchets

As previously mentioned in Chapter 1 and Section 2.4.5, Losic et al. (2009) identified a similarity in geometries between a drift ratchet pore and a girdle band diatom pore from the species *Coscinodiscus sp.* The possibility of identifying the drift ratchet mechanism in diatoms is intriguing from both an engineering and biological perspective. Biologically this would be the first identified example of a hydrodynamic drift ratchet in nature and will contribute a great deal to our understanding of how these microorganisms survive in their environment. Furthermore, there is the potential to use this and future knowledge gained regarding drift ratchet mechanisms, to improve the performance and efficiency of man-made separation and sorting devices (Yang et al. (2011)). In this chapter, the concept that diatoms use the drift ratchet mechanism to sort nutrients from harmful objects is explored.

The girdle band is the mid-section of the frustule, whereas the caps of the cylinder are known as the valves, as can be observed in Figure 4.1. These two regions have distinctly shaped pores, the significance of which is not yet understood. One side of the girdle band pore is open to the surrounding ocean environment while the other is bound by the deformable diatom cell membrane as shown in Figure 2.5, with the green membrane. Among other proposed functions it has been suggested that diatoms use their porous silica frustule to control, sort and separate nutrients from harmful entities such as colloids, pollutants, poisons and pathogens (Losic et al. (2006); Mitchell et al. (2013); Raven and Waite (2004)). It has been suggested that the architecture of the frustule could play an important role with respect to such separation, yet the exact mechanism for this has not been identified. In an attempt to explain how the distinct shape of the girdle band pores could control mass transfer to and from the cell membrane, Losic et al. (2009) recognised that these pores are geometrically similar to those of the hydrodynamic drift ratchet shown in Figure 4.2 (Kettner et al. (2000); Mathwig et al. (2011b); Matthias and Muller (2003)).

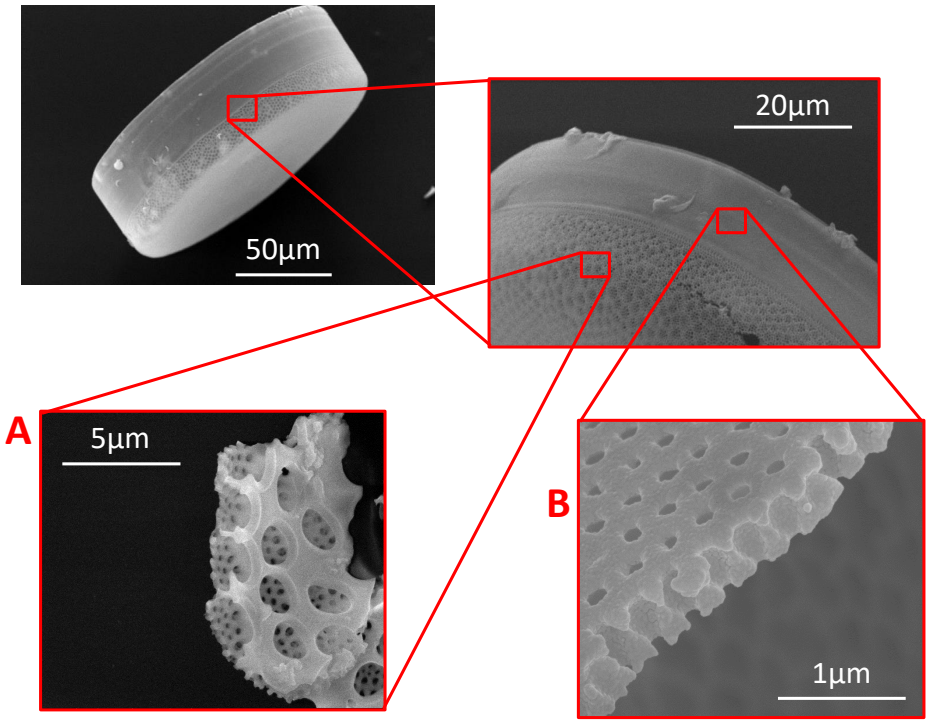

Figure 4.1 SEM of the diatom, *Coscinodiscus waiselii*. A) Valve structure and B) girdle band structure.

Consequently, this chapter will focus on establishing whether these girdle band pores can act as an effective hydrodynamic drift ratchet, to filter nutrients from harmful entities like viruses.

A hydrodynamic drift ratchet is a man-made microfluidic device comprised of a series of ratchet-shaped axisymmetric pores that are often placed in parallel to form a massively parallel membrane, shown in Figure 4.2a. Under the action of an oscillating fluid flow each pore can generate rectified motion of microparticles (Kettner et al. (2000); Mathwig et al. (2011b); Matthias and Muller (2003)), even though there is no net displacement of the fluid flow. These particles are able to migrate through the pore due to the combined effects of Brownian motion and particle-wall hydrodynamic interactions (Golshaei and Najafi (2015); Kettner et al. (2000); Schindler et al. (2007)). As the diatom cell membrane is deformable, the girdle band pore can also allow such zero-mean oscillatory fluid flow, and so could also function as a drift ratchet pore.

Typical membranes are comprised of around $15-30$ ratchet-shaped elements in series, hence these membranes are often analysed by neglecting end effects and idealizing these as an infinite series of periodic elements. In contrast, the diatom girdle band is comprised

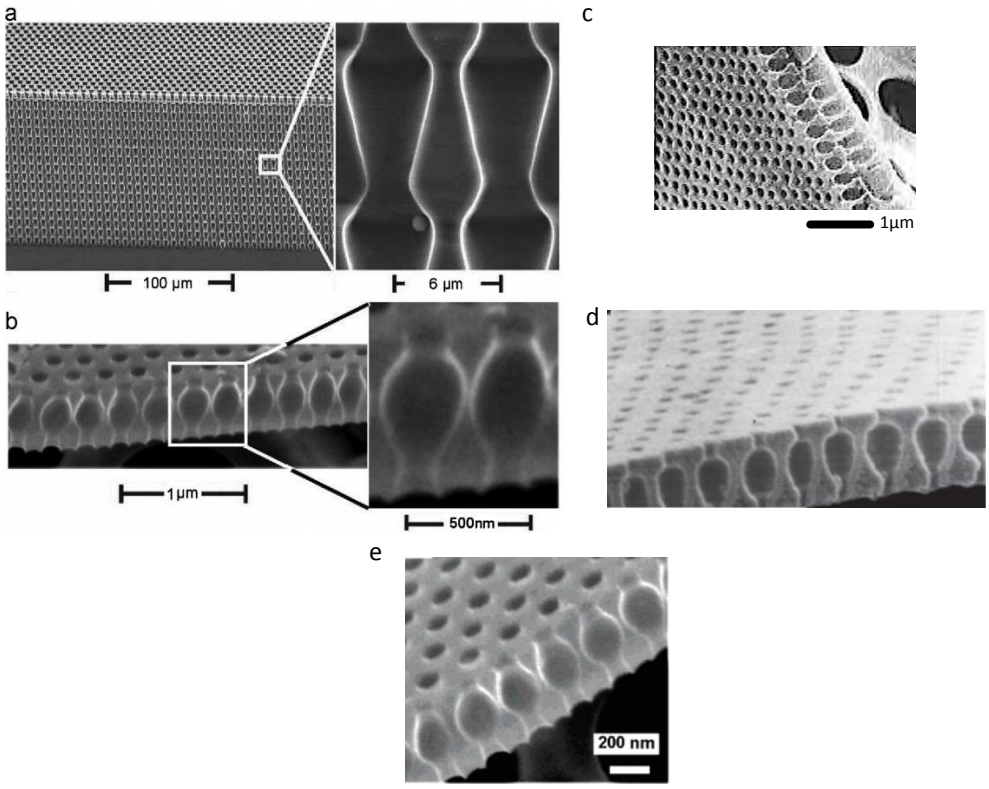

Figure 4.2 a) SEM of a massively parallel silica membrane with asymmetric pores (Matthias and Muller (2003)). b) SEM of girdle band pores of diatom *Coscinodiscus sp.* (Losic et al. (2009)). c) SEM of girdle band pores of diatom *Coscinodiscus sp.* (Rosengarten (2009)). d) SEM of girdle band pores of diatom *Coscinodiscus sp.* (scale unknown) – reproduced by permission of The Royal Society of Interface (Kucki and Fuhrmann-Lieker (2012)). e) SEM of girdle band pores of diatom *Coscinodiscus sp.* (Losic et al. (2007b)).

of a smaller (diameter and length), differently shaped pores, shown in Figure 4.2, and it is unknown whether such architecture can act as an efficient drift ratchet.

The shapes of the hydrodynamic drift ratchets studied in Kettner et al. (2000) and Matthias and Muller (2003), and shown in Figure 4.3a or Figure 4.2a, respectively, are not optimised to maximise particle separation performance or drift velocity. Therefore, these examples cannot be considered an ideal hydrodynamic drift ratchet. While this is true, these examples are still considered hydrodynamic drift ratchets and consequently will be referred by that name throughout this work.

Using the numerical model validated in Section 3.2, the possibility of the girdle band pores of *Coscinodiscus sp.* acting as a drift ratchet was investigated. To accomplish this, in Section 4.3, a single drift ratchet unit bound by two basins at each end was assessed to

determine if it retains the drift ratchet mechanism. This was completed to determine whether the 1-2 girdle band units would be able to generate drift.
In Section 4.4, the effect of a diminishing ratio between the advective and diffusive transport of particles in a drift ratchet was assessed and compared to the case of a diatom girdle band pore. Finally, in Section 4.5, it was determined whether only these two factors are at play when ruling out the girdle band pores as a drift ratchet by testing the shape of the girdle band pores at the scale of previously validated drift ratchets (Kettner et al. (2000)). The analyses presented in this chapter did not directly simulate the girdle band pore as the time step needed to resolve the particle-wall interactions was too small and therefore computationally expensive. As such, the larger drift ratchet pore geometry or a scaled-up girdle band pore are used in future computations in this chapter.

The intention of this chapter is to determine whether the girdle band pores can act as an effective drift ratchet, to do this, it must first be acknowledged that there are significant differences between a girdle band and a drift ratchet pore, namely the size, shape and configuration, as previously discussed. These differences will be further elucidated in the following section.

4.1 Difference between Drift Ratchet and Girdle Band Pores

To begin, the physical differences between the pores of the girdle band and a drift ratchet membrane shown in Figure 4.2 must be outlined. Also, the major oceanic processes that may cause oscillatory flows within the girdle band pores of the diatom in their natural aquatic environment, and the implications of these for particle sorting must be identified.

4.1.1 Difference in size, shape and configuration of the pores

As shown in Figure 4.3 and Table 2.1, both the typical diameter and length of a ratchet element within the diatom girdle band pore are smaller than those of the drift ratchet pores studied by Kettner et al. (2000), Matthias and Muller (2003) and Mathwig et al. (2011b). Furthermore, the girdle band pores only have one or two repeating units in series, which is significantly less than the $15-30$ ratchet units in series for the massively parallel drift ratchet membrane shown in Figure 4.2a.

Given the low number of repeating ratchet units in series for the girdle band pores, all simulations conducted herein involve a 1x amplitude fluid oscillation. This means that a parcel of fluid on the centreline of the pore travels the length of one repeating ratchet unit over half a period of fluid oscillation (Kettner et al. (2000)).

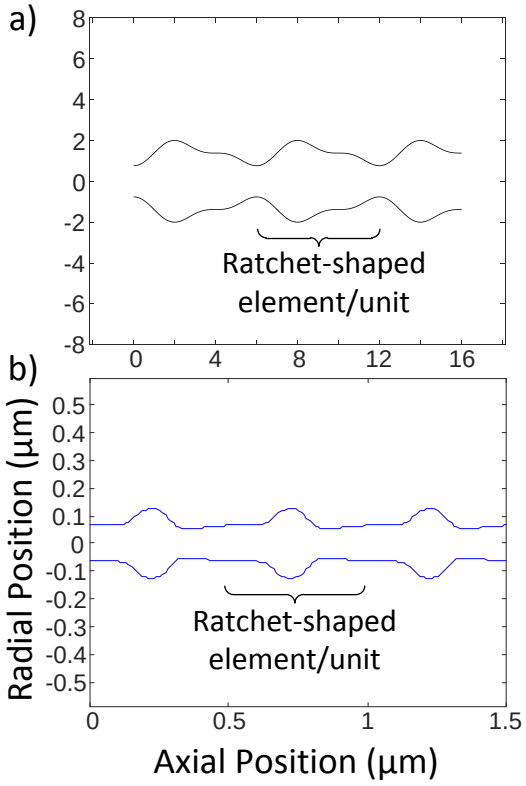

Figure 4.3 Schematic of the pore profile of a) a typical drift ratchet studied by Kettner et al. (2000) and b) girdle band pore of *Coscinodiscus sp.*

4.1.2 Forcing fluid

Hydrodynamic drift ratchet pores use an oscillating fluid flow to achieve rectification of microparticles in one direction. For diatom girdle band pores to act as a hydrodynamic drift ratchet, they must also experience a similar fluid oscillation, and the presence of the diatom cell membrane ensures such oscillations must have zero net displacement. Such oscillatory flow is driven by pressure fluctuations external to the girdle band pore. There are two main mechanisms that can generate pressure fluctuations relevant to diatoms in the Upper Ocean: (i) turbulent fluctuations in the upper oceanic flow and (ii) pressure fluctuations which arise from Jeffrey orbits (Jeffery (1922)) undertaken by the diatom in this flow due to its elongated shape. These pressure fluctuations need to be quantified to determine their impact upon flow in the girdle band. The timescales of the two pressure fluctuations; turbulent fluctuations (τ) and Jeffery orbit (T_{JO}) are assumed to be separable. Therefore, if $T_{JO} << \tau$ for a linear shear field then the Jeffery orbit movement will dominate the behaviour of the diatom in its

environment. Conversely, if $T_{JO} >> \tau$ then the response of the diatom to its environment will mainly be due to the residence time of the turbulence eddies.

To describe the typical geophysical fluid flow a diatom experiences in the surrounding ocean, it is necessary to consider the turbulence structure of the upper ocean flow. Similarly addressed in Chapter 2, geophysical turbulence in the upper ocean is comprised of superposed eddies of different sizes which are driven by a number of unsteady forcings and instabilities including wind, currents, tides and waves (Gregg (1973)). Breaking internal waves have been shown to be a critical component in the advective transport of deep, high nutrient waters and generation of high turbulence environments in particular scenarios (Alford (2003); Alford et al. (2015); Ferrari and Wunsch (2009)). In addition to these drivers, the turbulent structure of the flow acts to transfer kinetic energy from larger to smaller eddies, leading to the classical turbulent cascade (Kiørboe (2008)). The smallest eddy size is inversely proportional to the intensity of the turbulent kinetic energy (KoehlI et al. (2003)), which is characterised by the Kolmogorov length-scale η (Kolmogorov (1991)),

$$\eta = \left(\frac{\nu^3}{\varepsilon}\right)^{\frac{1}{4}}. \qquad \text{(2.11 revisited)}$$

Where ν is the kinematic viscosity (m^2s^{-1}) and ε is the kinetic energy dissipation rate (m^2s^{-3}). Energy dissipation in the open ocean typically ranges from $10^{-5}m^2s^{-3}$ in the upper mixed layer of the ocean for wind speeds of $15-20ms^{-1}$ to $10^{-9}m^2s^{-3}$ in deeper parts of the ocean (Kiørboe (2008)). From Equation 2.11 revisited, the length-scale of the smallest eddies range between $1-10mm$ (Karp-Boss et al. (1996); KoehlI et al. (2003)). Some parts of the ocean, like the South China Sea, reach an energy dissipation of approximately $10^{-4}m^2s^{-3}$ (Alford et al. (2015)), which means the Kolmogorov length drops to $300\mu m$. Below the Kolmogorov length-scale the smallest eddies are dominated by viscous forces, and so the local flow can be described as a linear shear flow and where these eddies transfer energy as heat via viscous dissipation (Kolmogorov (1991)). As the size of even the smallest eddies is significantly larger than a typical diatom size ($\approx 150\mu m$), all diatoms in the upper ocean experience a locally laminar flow, which is well-described as a local shear flow as illustrated by the linear velocity profile shown in Figure 2.1 (KoehlI et al. (2003); Lazier and Mann (1989); Yang et al. (2011)). This velocity field can lead to translation and rotation of the diatom which could drive the temporally symmetric fluid oscillations needed in the girdle band pore to generate a drift ratchet mechanism.

The unsteady character of this laminar flow field is described by the Kolmogorov time-scale (Lazier and Mann (1989); Mitchell et al. (1985); Musielak et al. (2009)),

$$\tau = 2\pi \left(\frac{\nu}{\varepsilon}\right)^{\frac{1}{2}} \qquad \text{(2.12 revisited)}$$

which characterises the correlation time of a local shear field, until a new one is generated with a new magnitude and direction (Karp-Boss and Jumars (1998); Musielak et al. (2009); Tennekes and Lumley (1972)). From the values above, the correlation time of a Kolmogorov eddy shear field in the ocean ranges over $\approx 0.6 - 200s$. This correlation time may then be interpreted as the period of the oscillating fluid force due to turbulent fluctuations.

As shown in Figure 1.2, diatoms are not spherical but rather are shaped like a prolate spheroid. Consequently, prolate spheroids within a linear shear field undergo tumbling motions in conjunction with a periodic translation orbit, known as a Jeffery orbit, shown in Figure 2.6. This lack of spherical symmetry in their frustule geometry means the diatoms can translate whilst undergoing tumbling in their hydrodynamic environment, leading to so-called variations of Jeffery orbits. The Jeffery orbit of a prolate spheroid has been used to represent the three-dimensional kinematic rotational trajectory of an elongated diatom cell in a linear shear field (Kim and Karrila (2013); Pahlow et al. (1998)). The fluid flow resulting from these pressure fluctuations are laminar and viscous dominated because of its low Reynolds number $Re \approx 0.005 - 0.1$, which is characteristic of the Stokes regime. These periodic flows can be described as instantaneous. Additionally, due to the unsteady nature of the flow as described by Equation 2.14 revisited the diatom will experience a variant of a Jeffery orbit.

The period of this orbit is then (Kim and Karrila (2013); KoehlI et al. (2003))

$$T_{JO} = \frac{2\pi}{G}\left(r_a + r_a^{-1}\right) \qquad \text{(2.14 revisited)}$$

where r_a is the aspect ratio (major to minor axis or minor to major axis) of the diatom cell and G the fluid shear rate. The characteristic shear rate in a Kolmogorov eddy is

$$G = \left(\frac{\varepsilon}{\nu}\right)^{\frac{1}{2}} \qquad \text{(2.15 revisited)}$$

which ranges from $0.5 - 12s^{-1}$ (Kiørboe (2008)) in the upper ocean. Combining these values for a sphere, aspect ratio $r_a = 1$, typical values for the period of orbit range over $\approx 1 - 25s$. For an aspect ratio more typical of a diatom, $r_a = 0.5$, the period of orbit ranges over $\approx 1.3 - 31s$. This rotational motion, in combination with the intermittency of the shear field in upper ocean turbulence generates fluctuations in the local velocity and pressure fields relative to the diatom surface (Pahlow et al. (1998)). These fluctuations could provide the oscillating flow required to generate particle drift via the ratchet mechanism in diatom

pores. As shown in Figure 2.7, for all of the values of energy dissipation rates, the period of orbit, T_{JO}, is much larger than the residence time of the linear shear field, τ, and therefore intermittency of the shear field provides the dominant fluctuations relevant for diatoms in their natural environment.

Another mechanism in which flow fluctuations could arise is during sinking of the diatom through the water column. Compared to the spontaneity of turbulence in the ocean, diatoms can self-regulate their buoyancy in response to external signals as well as forming chains and growing spines to alter their sinking rates (Guasto et al. (2011); Raven and Waite (2004)). Many studies (Eppley et al. (1967); Smayda (1971, 1970); Walsby and Holland (2006)) have investigated the bulk sinking rates of larger diatoms, however experiments by Gemmell et al. (2016) have shown that diatom sinking is a dynamic event in that larger diatoms can control their instantaneous decent rate within $200-300ms$. The bulk sinking rate of *Coscinodiscus sp.* has been reported to be $80-350\mu ms^{-1}$ (Eppley et al. (1967); Smayda (1971, 1970)). Whereas, Gemmell et al. (2016) shows variation in the instantaneous sinking rate of $10-750\mu ms^{-1}$ for *Coscinodiscus waiselii* depending on different nutrient deplete/replete cases, with a period of this variation on the order of seconds. Relative fluid velocity resulting from the combination of diatom sinking and ocean turbulence could generate these periodic fluid fluctuations that could potentially give rise to a drift ratchet in the girdle band pores.

This section has described examples of periodic fluid flow that could give rise to a drift ratchet flow through the girdle band pores of the diatom *Coscinodiscus sp.* During the remaining sections, the potential of the girdle band pores to act as drift ratchets will be investigated.

4.2 Effect of Particle Size on Drift Ratchet Performance

To determine whether the girdle band pores of a diatom could work as a hydrodynamic drift ratchet, in this section the effect of particle size on the performance of a drift ratchet was assessed and these results were applied to the case of a diatom girdle band pore. As shown in Figure 4.4, the magnitude of the particle drift velocity in a drift ratchet exhibits a maximum as a function of the ratio of particle size to minimum pore diameter. For smaller and smaller particles, the dominance of diffusion in transporting the particles increase relative to the advective component, reducing the Péclet number (Pe) and resulting in reduced particle drift through the drift ratchet. This continues to a limit where the smallest particles act as infinitesimal point particles and therefore do not interact with the pore wall at all and so the particles exhibits no drift. Conversely, as the micro-particles increase in size relative to the

pore they reach a physical limit of the minimum pore diameter and cannot travel through the drift ratchet. Before this limit though the Pe increases, where particle advection dominates in the fluid oscillation cycle. For an infinite Pe the particle's motion is fully reversible along a streamline and no drift occurs.

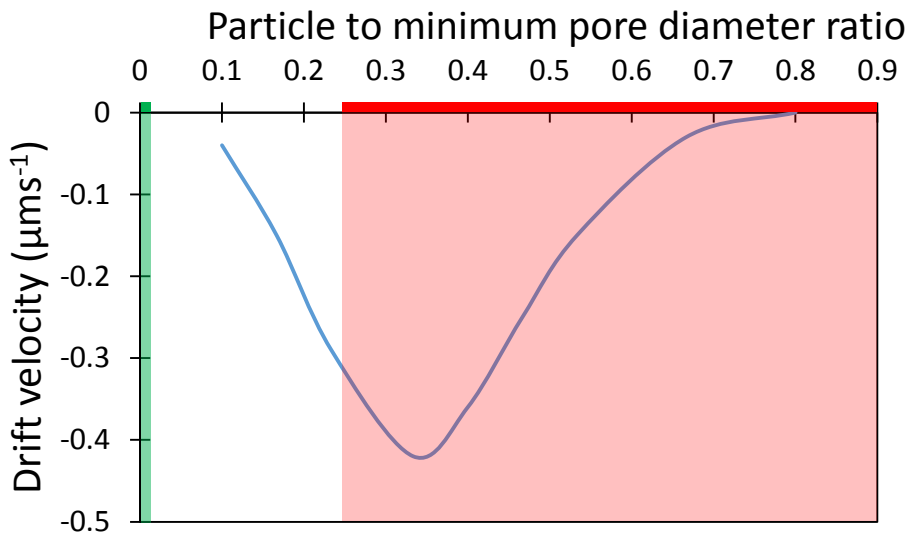

Figure 4.4 Effect of particle size on drift velocity data from Kettner et al. (2000) for a drift ratchet with fluid oscillations of $40Hz$ and fluid viscosity that of water. (Red) Ratio of typical virus size to minimum girdle band pore diameter. (Green) Ratio of nutrient ion size to minimum girdle band pore diameter. The negative drift velocity represents the direction through the pore the particles are drifting.

These results can then be applied to the range of particles diatoms encounter in their natural environment. Diatoms live in the euphotic zone of marine environments to facilitate energy production and cell growth via photosynthesis. They uptake and process inorganic nutrients and trace elements used for a variety of differing cell functions, including;

- Fe^{3+} and Fe^{2+}: used for fixing nitrogen and maintenance of photosynthetic organelles (Sunda and Huntaman (1997))
- H^{+}, Cl^{-}, K^{+} and Na^{+}: used to control ionic cell content and control transmembrane pores (Taylor (2009))
- $NH_4{}^{+}$, $NO_3{}^{-}$ and $PO_4{}^{3-}$: used as inorganic nutrients in protoplasm growth (Boyd and Gradmann (1999b); Round et al. (1990))

- $Si(OH)_4$: used to build the rigid silica frustule (Kamykowski and Zentara (1985); Melkikh and Bessarab (2010); Wischmeyer et al. (2003))

- HCO_3^- and pCO_2: used as a source of carbon dioxide in photosynthesis to produce sugars, energy and oxygen (Tortell et al. (1997))

- Trace metals (Cu, Cd and Zn) for catalysing reactions (Morel et al. (1991)).

In ionic form, these chemical species move through the pores of the silica frustule before being taken up by the cell membrane (Hochella Jr. et al. (2008)). The size of these ions is typically $1-2nm$, yielding a ratio of ion to pore size ranging over $\approx 0.01-0.02$ with respect to the minimum girdle band pore diameter, of $100nm$, presented in Table 2.1. This range is represented by the thin green band in Figure 4.4, indicating that the drift velocity of these nutrients and trace elements is negligible and so would not be significantly transported by a drift ratchet. Diatoms are also exposed to harmful entities such as viruses, bacteria, pollutants and poisons. The typical size of viruses which can infect diatoms are of the order of $25-220nm$ (Nagasaki (2008)), corresponding to a particle to pore size ratio of $0.25-2.2$ which is represented by the red band in Figure 4.4. For particles with the particle to pore ratio in the range $0.25-0.7$, it appears a drift ratchet could significantly transport these deleterious entities, and the mean flux would need to be directed away from the pore membrane. The next section investigates whether the small number asymmetric ratchet-shaped units in the girdle band pores can still produce drift of particles.

4.3 Finite Pore Bounded by Basins

The diatom girdle band pore differs from an engineered drift ratchet in that only $1-2$ ratchet elements are connected in series in girdle band pore. To determine whether the single ratchet-shaped unit in the girdle band pores can give rise to the drift mechanism a simulation of a planar two-dimensional drift ratchet pore with a single ratchet-shaped element between two fluid reservoirs was performed. Zero-mean oscillating flow was applied between these reservoirs, shown in Figure 4.5, where the pore shape is the same as a typical drift ratchet shown in Figure 4.1a.

The evolution of the particle position within the pore was captured via stochastic Langevin equation

$$\frac{d\boldsymbol{x}}{dt} = v_{fluid}(\boldsymbol{x}(t),t) + \boldsymbol{\eta}(t) \tag{4.1}$$

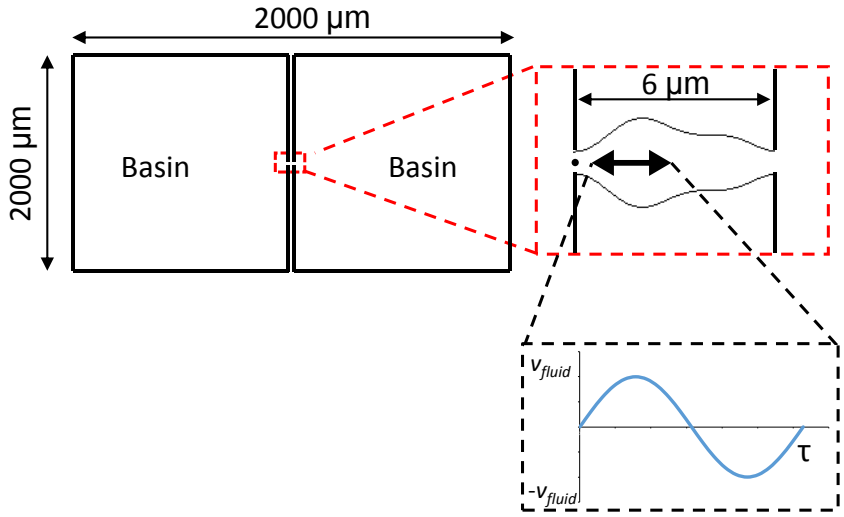

Figure 4.5 Schematic of the numerical simulation of the finite drift ratchet pore, bound by two basins.

where v_{fluid} is the local fluid velocity (determined via computational fluid dynamics (CFD)) and Brownian motion is modelled as the Gaussian white noise $\boldsymbol{\eta}(t)$ (Kettner et al. (2000)). The discretised set of equations for the location of the particle in the x and z coordinates from Equation 4.1 is,

$$x_{n+1} = x_n + v_{fluid}(x(t),t)\Delta t + \sqrt{2D_{fs}\Delta t}\gamma \tag{4.2}$$

$$z_{n+1} = z_n + v_{fluid}(z(t),t)\Delta t + \sqrt{2D_{fs}\Delta t}\gamma \tag{4.3}$$

Δt is the time step, D_{fs} is the free space particle diffusion coefficient and γ is a random number from a standard normal distribution with variance equal to one. The z-axis is along the two-dimensional drift ratchet pore presented in Figure 4.5. Following earlier studies (Herringer et al. (2017); Kettner et al. (2000); Schindler et al. (2007)), the particle-wall interactions are captured as a simplified fully elastic ballistic reflection which qualitatively captures the action of the pore wall in generating rectified particle motion. All particles were initially placed at the left opening of the pore, and the flow cycle was such that the initial fluid velocity was from left to right in Figure 4.5. The magnitude of the fluid oscillation was such that a fluid element along the pore centreline is displaced by a distance of one pore length over a half-cycle of the oscillating flow. This fluid amplitude was chosen because all drift ratchet studies up to now have defined the fluid amplitude as being displaced one or two

ratchet elements over half a fluid oscillation cycle. Since the girdle band pores of the diatom *Coscinodiscus sp.* are usually characterised by a single ratchet-shaped unit, implementing a fluid amplitude of more than one ratchet element would short circuit the ratchet pore and make having a drift ratcheting mechanism pointless as the particles contact the diatom membrane.

To identify whether a finite single ratchet-shaped pore will exhibit particle drift its performance was compared to that of its two-dimensional infinite pore counterpart and two-dimensional finite straight pore shown in Figure 4.6.

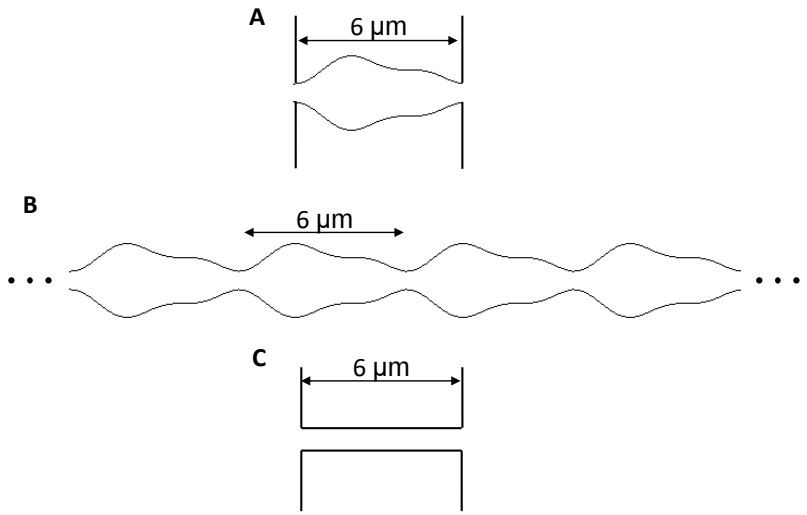

Figure 4.6 A) Finite two-dimensional and B) Infinite two-dimensional hydrodynamic drift ratchet pore. C) Finite two-dimensional straight pore

The ratio of effective to free space particle diffusion coefficient

$$\frac{D_e}{D_{fs}} = \frac{\left[\frac{\langle z^2(t_{run})\rangle - \langle z(t_{run})\rangle^2}{2t_{run}}\right]}{D_{fs}} \qquad \text{(3.12 revisited)}$$

and average drift velocity

$$v_e = \frac{\langle z(t_{run})\rangle}{t_{run}} \qquad \text{(3.11 revisited)}$$

are parameters used to assess the performance of a typical drift ratchet. Where, $z(t_{run})$ is the displacement of a particle along the axis of the drift ratchet pore over a time period t_{run}. $\langle \cdots \rangle$ represents the ensemble average over 100 particles.

In the straight-walled pore no drift of particles was expected. The results shown in Table 4.1 show more than one repeating ratchet unit is required to obtain the drift velocity

corresponding to an infinite drift ratchet pore. This means that it is unlikely that the girdle band pores act as a drift ratchet. Future work could be focused on determining the critical number of ratchet elements needed in series to generate drift representative of an infinite pore, however this is not the objective of this study.

The results shown in Table 4.1 show that even for a drift ratchet more than one repeating ratchet unit is required to obtain the drift velocity corresponding to an infinite drift ratchet pore.

Table 4.1 Drift velocity and ratio of effective to free-space diffusion coefficient for the case of a two-dimensional finite drift ratchet and straight-walled pore bound by two basins. Compared to an infinite two-dimensional drift ratchet pore.

	Infinite 2D drift ratchet	Finite 2D ratchet unit	Finite 2D straight pore
D_e/D_{fs}	5.0	1.2	1.3
v_e	-0.24	9×10^{-4}	6×10^{-3}

The next section takes the investigation a step further and determines whether the increase in diffusion dominance at the smaller scale of the girdle band pores has an effect on it being able to generate particle drift. A typical infinite drift ratchet pore was simulated over a range of different Pe to define a relationship between Pe and drift velocity. This relationship was then translated to the case of a diatom girdle band pore.

4.4 Effect of Péclet Number on Drift

From previous studies (Kettner et al. (2000); Schindler et al. (2007)) it is known that a decreasing Péclet number (Pe), which relates to an increase in diffusive transport processes over advective, leads to a vanishing particle drift. Consequently, this section elucidates the qualitative relationship between Pe and the average drift velocity in an infinite drift ratchet pore. It can then be seen whether the Pe of a typical girdle band pore is in the same range as that determined to generate particle drift.

First, the average Péclet number was defined as,

$$Pe_{Avg.} = \frac{VL}{D_{fs}} \tag{4.4}$$

where the mean particle velocity is $V = 2L/T_{ff}$, L is the fluid displacement along the pore axis over half a period of fluid oscillation $T_{ff}/2$. The free-space diffusion coefficient of the particle in the fluid flow is represented by,

$$D_{fs} = \frac{k_B T}{6\pi\mu R} \tag{4.5}$$

where, k_B is the Boltzmann constant, T is the temperature, μ is the dynamic viscosity and R is the particle radius. The same numerical model as described in the previous section in Equation 3.1 was used, however instead of a constant diffusion coefficient a spatially varying diffusion coefficient was used, which is different to the free-space parameter defined in Equation 4.5. This spatially dependent diffusion coefficient arises from lubrication forces between the diffusing Brownian particle and the pore wall. As the perpendicular distance from the particle's centre to the wall decreases the hydrodynamic resistance diverges. The implementation and effect of this augmented diffusion coefficient is explained further in Chapter 3 (Herringer et al. (2017)). The shape of the drift ratchet pore modelled is shown in Figure 4.3a. Table 4.2 shows the geometric characteristics of the diatom pores, Case 2, compared to a previously studied drift ratchet, Case 1, shown in Figure 4.3a.

Table 4.2 Comparison between parameters for a drift ratchet and girdle band pores.

	Case 1	Case 2			
Minimum pore diameter (μm)	1.58	0.1	0.1	0.1	0.1
Mass diffusion coefficient ($\mu m^2 s^{-1}$)	0.6	14.5	14.5	14.5	14.5
Particle diameter (μm)	0.7	0.03	0.03	0.03	0.03
Length of repeating unit (μm)	6	0.5	0.5	0.5	0.5
Ratio of particle diameter to minimum pore diameter	0.44	0.3	0.3	0.3	0.3
Average Péclet number	4800	17	1.4	0.11	0.034
Period (s)	0.025	0.002	0.025	0.3	1

The flow through the girdle band pores, Table 4.2 Case 2, is characterised by a considerably smaller average Péclet number compared to that for a typical hydrodynamic drift ratchet, Table 4.2 Case 1. This means that diffusion is the dominant transport process at the smaller scale of the girdle band pores.

The results in Figure 4.7 show that there exists a Pe number that maximises drift velocity. Such a maximum is expected because in the limit of large Pe (vanishing diffusivity), fluid trajectories are fully reversible and there is no mechanism for particle transport across streamlines. Conversely, in the limit of vanishing Pe (large diffusivity) diffusion dominates over the advecting particle-wall interactions, leading to a largely uniform particle probability

distribution within the pore-space and no net drift (Schindler et al. (2007)). Thus, only at intermediate values of Pe can the drift mechanism impart significant net particle transport.

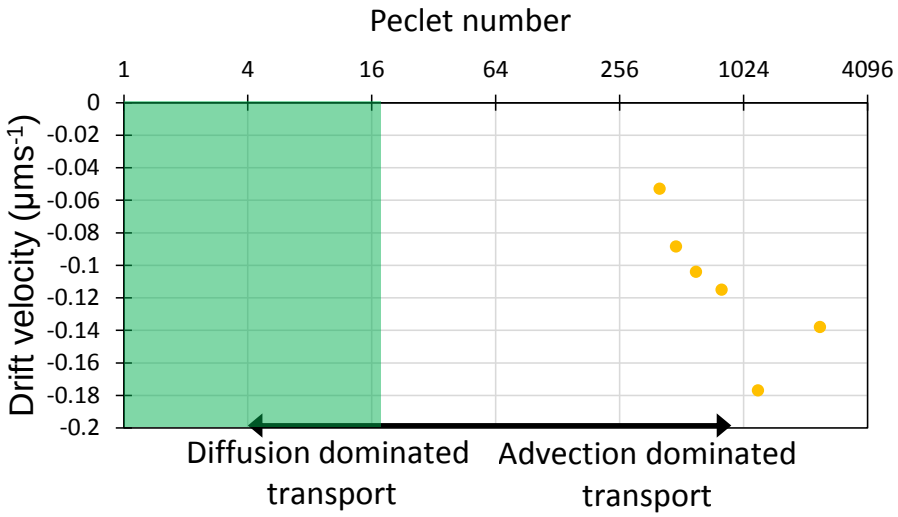

Figure 4.7 Relationship between the average Péclet number and the drift velocity in a drift ratchet. The simulations were conducted with a spatially variable mass diffusion coefficient and a fluid velocity field obtained using CFD. Green shaded area refers to the *Pe* range a diatom could experience.

From Figure 4.7 and Table 4.2 the range of Pe that occurs in a girdle band pore is several orders of magnitude smaller than that which gives rise to significant particle drift (note the logarithmic scale of the horizontal axis in Figure 4.7). These results indicate that under normal conditions in the upper ocean, mass diffusion within the girdle band pore is too large for diatoms to use the drift ratchet mechanism to sort and separate particles. This result leads to the natural question; if the Pe was increased in the case of a girdle band pore to the range experienced by a typical drift ratchet could particle drift be generated in the girdle band pores? This will be addressed in the next section by increasing the size of the girdle band pore to that of a typical drift ratchet.

4.5 Scaled Girdle Band Pore

To determine whether the effect of shape, as well as the scale of the girdle band pore, contributes to its inability to generate particle drift, girdle band pores upscaled to the size of a typical hydrodynamic drift ratchet pore, shown in Figure 4.2a and studied by Kettner et al. (2000), have been simulated.

Table 4.3 shows the parameters of the cases simulated to show whether the shape of the girdle band pore geometry is responsible for the lack of particle drift.

Table 4.3 Parameters used for the numerical simulation to find whether the girdle band pore geometry can act as a drift ratchet.

	Case 8	Case 9	Case 10	Case 11
Minimum pore diameter (μm)	1.58	1.6	1.2	1.6
Mass diffusion coefficient ($\mu m^2 s^{-1}$)	0.6	0.6	0.79	0.6
Particle diameter (μm)	0.7	0.7	0.53	0.7
Length of repeating unit (μm)	6	8	6	6
Ratio of particle diameter to minimum pore diameter	0.44	0.44	0.44	0.44
Average Péclet number	2407	5120	2407	2407
Period (s)	0.025	0.025	0.025	0.025
Number of fluid oscillations over t_{run}	4000	4000	4000	4000

In Case 9 the girdle band pore is upscaled so the minimum pore diameter matches that for the typical drift ratchet, while the pore in Case 10 is upscaled to match the length of their ratchet-shaped elements. As such the girdle band pores in Case 9 and 10 are upscaled by 16x and 12x their original size, respectively. A comparison between these cases was then completed with a symmetrical sinusoidal-walled pore, which is expected to have zero particle drift due to the absence of pore wall asymmetry along the axis of the pore. Numerical simulation parameters for Case 8 is that for a drift ratchet pore studied by Kettner et al. (2000). Case 9 is that for a girdle band pore scaled to the size of the pore in Case 8 so the minimum pore diameters are the same, and Case 10 is that for a girdle band pore scaled to the size of the pore in Case 8 so the length of a repeating asymmetric unit is the same. Case 11 is a sinusoidal-walled pore the same size as Case 8, but without the pore wall asymmetry.

As can be seen in Table 4.4 both scaled girdle band pores exhibit particle drift. This means that the girdle band pores are capable of acting as a hydrodynamic drift ratchet due to their shape, however, because of its size and single ratchet-shaped unit configuration it is

likely that it does not operate as a drift ratchet, discussed in Sections 4.4 and 4.3, respectively. Particle drift in a symmetrical sinusoidal pore was also simulated to validate the model as it is expected to be close to zero drift of particles due to the lack of asymmetry in the pore geometry. These simulations also include a spatially varying diffusion coefficient which is more indicative of a drift ratchet in the real-world.

Table 4.4 Drift velocity for the case of a scaled up girdle band pore.

	Case 8	Case 9	Case 10	Case 11
v_e (μms^{-1})	-0.18	0.3	0.41	-0.018

4.6 Hydrodynamic Immunity

As previously discussed in Chapter 2 the diatom frustule has many proposed functions including: increasing or decreasing sinking rates through the water column (Fisher (1995); Raven and Waite (2004); Waite et al. (1997)); providing defence against predators, parasites and pathogens (Hamm (2005); Raven and Waite (2004)); providing an acid-base buffer site for the catalysis of carbonic anhydrase (Milligan and Morel (2002); Morant-Manceau et al. (2007)); protecting sensitive organelles against damage from UV–A and UV–B exposure and scattering photosynthetic active radiation (De Tommasi et al. (2008); Fuhrmann et al. (2004); Hsu et al. (2012); Ingalls et al. (2010); Losic et al. (2009); Noyes et al. (2008); Yamanaka et al. (2008)). Other less familiar proposed functions include: countering the turgor pressure generated by the cell (Schmid (1994)); helping to facilitate reproduction processes (Round et al. (1990)) and acting as a passive barrier, controlling, sorting and separating matter like a filter (Losic et al. (2009)). Such functions provide the diatom with advantages so it can grow and survive in its environment. However, amid these proposed functions, the reason for the distinct shape of girdle band pores is still unknown.

The proposed hypothesis that girdle band pores operate as a hydrodynamic drift ratchet was originally suggested following the observation that they were geometrically similar and it was thought that this mechanism allowed the diatom to separate and control the transport of nutrients towards the frustule while keeping deleterious entities away. However, this analysis suggests that the girdle band pores do not operate as a hydrodynamic drift ratchet. This section proposes an alternate explanation for the girdle band pore shape, such that it allows the uptake of carbon dioxide into the frustule whilst excluding viruses and pathogens. According to Nagasaki (2008) the size of viruses that could infect diatoms range from 25 to 220nm. When compared to the minimum diameter of the girdle band pores of 100nm, a

chance remains that a virus could pass through the pores. Recent studies into the mechanics of diffusiophoresis in microchannels (Hoshyargar et al. (2016); Lin et al. (2016); Ma and Keh (2006)), and in particular studies involving dead-end channels (Chen and Xu (2017); Shin et al. (2016); Velegol et al. (2016)), have shown that significant flows can arise in dead-end microchannels under appropriate conditions. This study hypothesises that a significant recirculating flow as shown in Figure 4.8 occurs within the girdle band pore, as a result of diffusiophoresis, and this simultaneously promotes carbon dioxide transport through the frustule towards the cell, whilst excluding larger viruses and pathogens.

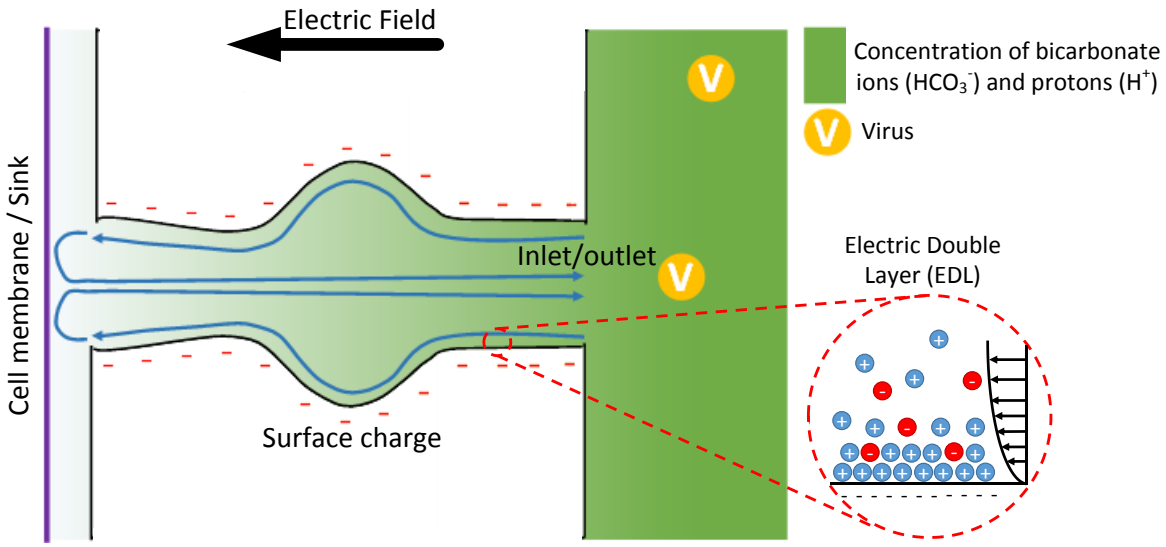

Figure 4.8 Schematic of generic diffusiophoresis case for a dead-end girdle band pore.

As illustrated by Figure 4.9, if the thickness of the inflow band (d), at the end of the girdle band pore that is open to the aquatic environment, is smaller than the diameter of a virus it is unlikely to enter the pore whilst still allowing the smaller bicarbonate ion species to enter the pore. These bicarbonate ions will be converted to carbon dioxide by an external carbonic anhydrase near the cell membrane, which will then diffuse across the cell membrane to be used for photosynthesis (Milligan and Morel (2002); Morant-Manceau et al. (2007); Tortell et al. (1997)).

Diffusiophoresis thought to be responsible for this “hydrodynamic immunity” is composed of four transport mechanisms; chemiosmosis, electroosmosis, electrophoresis and chemiphoresis. The latter two mechanisms directly affect the transport of surface charged particles in the pore, like a virus. While, the annulus inflow of fluid in the girdle band pore

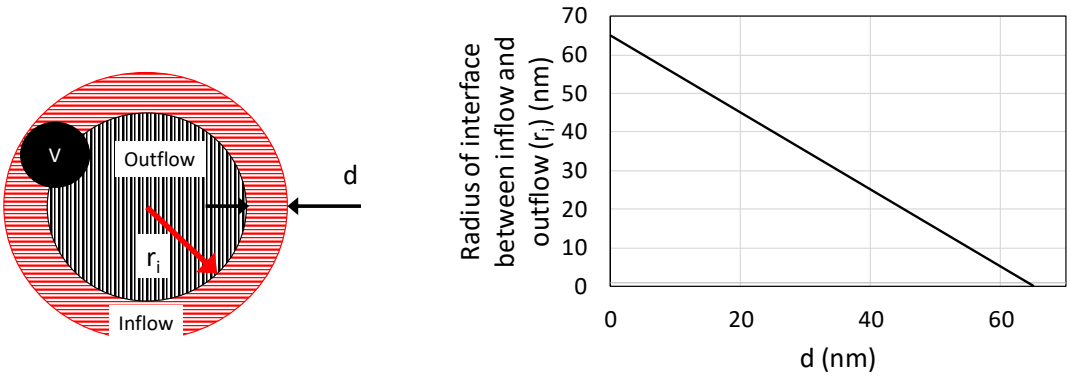

Figure 4.9 Schematic of the cross section of the inlet/outlet of the girdle band pore illustrated in Figure 4.8. Inflow is represented by the horizontal hatching, while outflow is represented by the vertical hatching.

shown in Figure 4.8 is driven by chemiosmosis and electroosmosis, which will be discussed further in the coming section.

As diatoms live in a soup of ions in the ocean, a high density of charged ions form an electric double layer (EDL) adjacent to the negatively charged amorphous silica of the girdle band pores shown in Figure 4.8. The thickness of this layer is characterised by the Debye length κ^{-1} (Schoch et al. (2008))

$$\kappa^{-1} = \sqrt{\frac{\varepsilon_r \varepsilon_0 k_B T}{\sum_i C_i^{\inf} (z_i e)^2}}. \tag{4.6}$$

Where ε_r is the dielectric constant of the fluid, ε_0 is the permittivity of a vacuum, k_B is the Boltzmann constant, T is the temperature, C concentration of ionic species, e is the charge of an electron and z is the valence of the ionic species. Under typical conditions in the upper ocean, it is estimated the thickness of the electric double layer to be order $\approx 1nm$, which is negligible with respect to the minimum pore radius of $50nm$ and therefore the EDL may be considered infinitesimal (Prieve et al. (1984)). Generally, an external electric field can interact with the EDL to generate fluid flow along a charged surface via electroosmosis. To my knowledge, diatoms do not actively generate an electric field, instead the diatom cell's consumption of ionic species produces a concentration gradient of ions which passively induces an electric field. This electric field is tangential to the concentration gradient and is driven by the difference in diffusion coefficients of two oppositely charged ion species, i.e. $D_+ \neq D_-$, diffusing down a concentration gradient while ensuring electroneutrality is satisfied (Chen and Xu (2017); Prieve and Roman (1987); Shin et al. (2016); Velegol et al.

(2016)). In diatoms, bicarbonate (HCO_{3-}) and protons (H^+) are expected to be the main ionic species to contribute to this electric field as they will be consumed at the cell membrane via conversion to carbon dioxide, and both have differing values for diffusivity.

Chemiosmosis is another mechanism responsible for fluid flow in the EDL, similar to electroosmosis, except the driving force is the change in EDL thickness as a result of the concentration gradient along the girdle band pore axis. A position along the chemical gradient with a higher concentration will have a thinner EDL (Chen and Xu (2017); Prieve and Roman (1987); Shin et al. (2016); Velegol et al. (2016)). Subsequent fluid slipping adjacent to the pore wall is caused by excess pressure in the double layer along the pore surface (Hoshyargar et al. (2016); Keh and Ma (2004)). As the girdle band pore is partially blocked by the cell membrane at one end, as depicted in Figure 4.8, the flow of water via electroosmosis and chemiosmosis creates an annulur inflow / outflow condition. The inflow travels along the surface of the girdle band pore towards the cell membrane and is forced back through the pore opening along its axis. Ultimately, it is the conclusion of this investigation that it is this flow condition that may help keep viruses out of the frustule.

Due to the effect of the concentration gradient induced electric field on the EDL, the equations governing Stokes flow are now,

$$\mu\nabla^2\boldsymbol{u} - \nabla p + \rho\boldsymbol{E} = 0 \tag{4.7}$$

$$\nabla\cdot\boldsymbol{u} = 0 \tag{4.8}$$

where $\rho = (C_+ - C_-)Ze$ is the local space charge density and based on Coulomb's law $\nabla\cdot E = 4\pi\rho/\varepsilon$ and $E = -\nabla\psi$ (Prieve and Roman (1987)). ε is the permittivity of the fluid and ψ the electrostatic potential (Prieve and Roman (1987)). These equations can be combined to form Poisson's equation

$$\nabla^2\boldsymbol{\psi} = 4\pi(C_+ - C_-)Ze/\varepsilon \tag{4.9}$$

The advection-diffusion equation is now,

$$\frac{\partial C_i}{\partial t} + \nabla\cdot\left(-D\nabla C - D\frac{Z_i e C_i}{kT}\nabla\psi + \boldsymbol{u}C\right) = R \tag{4.10}$$

$$D = \frac{2D_+D_-}{D_+ + D_-} \tag{4.11}$$

These partial differential equations can be used to resolve the electric double layer after applying appropriate boundary conditions, however this is numerically intensive for such a thin EDL. COMSOL approximates electroosmotic flow velocity near the wall as

$$u_{Electro} = -\frac{\varepsilon_r \varepsilon_0 \zeta}{\mu} \left(\boldsymbol{E} - (\boldsymbol{E} \cdot \boldsymbol{n}) \boldsymbol{n} \right) \tag{4.12}$$

where ε_r is the fluid dielectric constant, ε_0 is the permittivity of a vacuum, ζ is the surface zeta potential, μ is the dynamic viscosity of the fluid and $\boldsymbol{E}$ is the external electric field.

Equation 4.12 was used to determine the magnitude of electroosmosis in the girdle band pore and to what extent the magnitude of the electric field affects the thickness of the inflow area (d) (see Figure 4.9). Figure 4.10 shows that for an increase in electric field magnitude, the thickness of the inflow area stays constant. As previously mentioned, the smallest viruses expected to infect diatoms are of the order of $25nm$, therefore the $\approx 15nm$ thick inflow section in Figure 4.10 would be too small for a virus to enter the frustule. However it must be acknowledged that this simulation is valid where ion concentration gradient dependent electric fields are not considered. In reality, the diatom induces an electric field through the generation of a concentration gradient and future numerical models would have to capture this.

Interestingly, due to the shape of the girdle band pore, a recirculation region exists when experiencing electroosmotic flow, as can be seen in Figure 4.10. This is a result of the unique asymmetric shape of the girdle band pore, which could be a last line of defence to trap unwanted particles. However further work is required to clearly elucidate its function.

In order to assess the potential for diffusiophoresis within the girdle band pore, an order of magnitude analysis was conducted, in which the typical concentration gradient is determined for a diatom girdle band pore and subsequent magnitude of the electroosmotic flow. The uptake of ionic species by the diatom cell, whether nutrients for cell growth and repair, or bicarbonate ions to facilitate photosynthesis, generates a diffusion boundary layer around the cell. This boundary layer, that induces an electric field, extends from the cell surface through the girdle band pores and multiple cell radii into the cell's aquatic surroundings. The steady-state concentration profile for a spherical cell in a diffusion limited scenario is (Guasto et al. (2011); Karp-Boss et al. (1996); Musielak et al. (2009))

$$\frac{C - C_0}{C_{\text{inf}} - C_0} = \frac{[\frac{r_0}{r}(C_0 - C_{\text{inf}})] + C_{\text{inf}} - C_0}{C_{\text{inf}} - C_0} \tag{4.13}$$

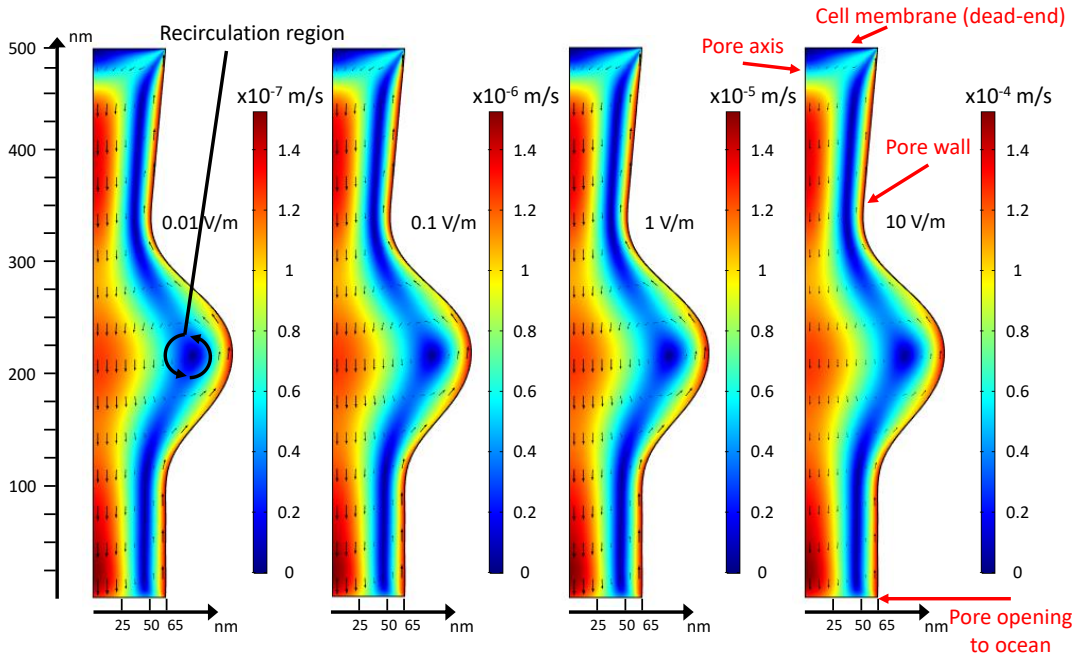

Figure 4.10 Fluid structure when osmotic flow is applied to a dead-end girdle band pore. From left to right the surface charge density is increased from 0.01 V/m to 10 V/m and applied to the pore wall.

where r_0 and r are the cell radius and radial position respectively and C, C_{inf} and C_0 respectively are the species concentration at arbitrary radial positions, in the bulk and at the cell surface (Jumars (1993)). The change in non-dimensional concentration over the thickness of a girdle band pore ($\approx 700nm$) is 1.4×10^{-2}. This could translate into a constant concentration gradient of $44kmol/m^4$ if the ambient ion concentration is $2.2mol/m^3$ and concentration at the cell surface is $0mol/m^3$ for the case of bicarbonate ions. Assuming an infinitesimal EDL, fluid flow via diffusiophoresis in an electrolyte solution with a concentration gradient on the order of $100kmol/m^4$ along a surface with a zeta potential magnitude of $\approx 25mV$, similar to the surface of a diatom girdle band pore, can provide flow at several micrometers per second (Keh and Ma (2004)). This study of flow magnitude means the girdle band pores could generate these flows with the concentration gradient they experience of $44kmol/m^4$, while having the capacity to ensure viruses do not enter the pore.

The remaining transport phenomena, electrophoresis and chemiphoresis, further dictate the movement of any charge particles in the pores, such as viruses. Fluid adjacent to the charged surface of the particle slips in a similar fashion to the movement of water adjacent to the pore wall via electroosmosis and chemiosmosis, however in the case of the particle the

change in momentum of the fluid around the particle generates a force on the particle in the opposite direction, termed electrophoresis and chemiphoresis. This needs to be taken into account when simulating a virus in a girdle band pore.

This section presented preliminary electoosmotic flow simulations through a diatom girdle band pore, see Figure 4.10. This qualitative analysis was completed as a proof-of-concept, to determine whether diffusiophoresis was a feasible mechanism to be used by the diatom frustule to decrease the likelihood of virus infection via the ratio of inflow to outflow area.

4.7 Summary of Findings

This chapter determined, through numerical analysis, that it is unlikely that the girdle band pores of the centric diatom *Coscinodiscus sp.* act as a hydrodynamic drift ratchet to separate nutrients from harmful particles such as pathogens, pollutants or poisons. A theory related to diffusiophoresis was proposed as a mechanism that the diatom frustule could use to achieve this prevention of infection from viruses whilst allowing nutrients to pass through to the cell. This novel separation mechanism was termed “hydrodynamic immunity”.

Throughout this investigation to determine whether a diatom girdle band pore is actually representative of a hydrodynamic drift ratchet there have been only two research papers which are related to experimental verification of the theoretical hydrodynamic drift ratchet separation mechanism. These studies were inconclusive to whether a hydrodynamic drift ratchet could be achieved in a real-world scenario. Due to the uncertainty surrounding these experiments it was decided to design and fabricate a novel hydrodyanmic drift ratchet experimental setup to measure whether unidirectional drift in these devices exist. This is covered in the next chapter.

Chapter 5

Experimental Realisation of a Drift Ratchet

This chapter presents results from experiments designed to demonstrate the hydrodynamic drift ratchet mechanism for the first time. While providing useful data, these results give inconclusive evidence of the presence of the drift ratchet phenomenon. However, potential improvements to the experimental procedure were discovered, which can be made in the future to finally conclusively determine whether the drift ratchet mechanism can be achieved in real-world separation devices. These improvements are discussed further in Chapter 6. For the experimental setup discussed herein, inspiration was taken from previous experimental drift ratchet papers (Kettner et al. (2000); Mathwig et al. (2011b); Matthias and Muller (2003)) with critical differences, with the main one being the ability to visualise particles during the ratcheting process. This gives improved quality of data and ease of post analysis. This novel drift ratchet device will be discussed further.

5.1 Experimental Setup and Procedure

This experiment involved injecting water or methanol with spherical fluorescent polystyrene microparticles into an in-house fabricated microfluidic chip. The fluid-particle mixture was pumped sinusoidally through the drift ratchet channels in the chip by the contraction and expansion of a piezoelectric disc mounted externally on the back of the silicon chip, as depicted in Figure 5.1. The frequency of the oscillation was $40Hz$ (Matthias and Muller (2003)). The size of the polystyrene microparticles used were $0.7\mu m$ in diameter, and their density was $1.01gcm^{-3}$. The fluid oscillation frequency and particle size were similar to that used by Matthias and Muller (2003), Mathwig et al. (2011b) and Kettner et al. (2000), and

simulations shown in Chapter 3.

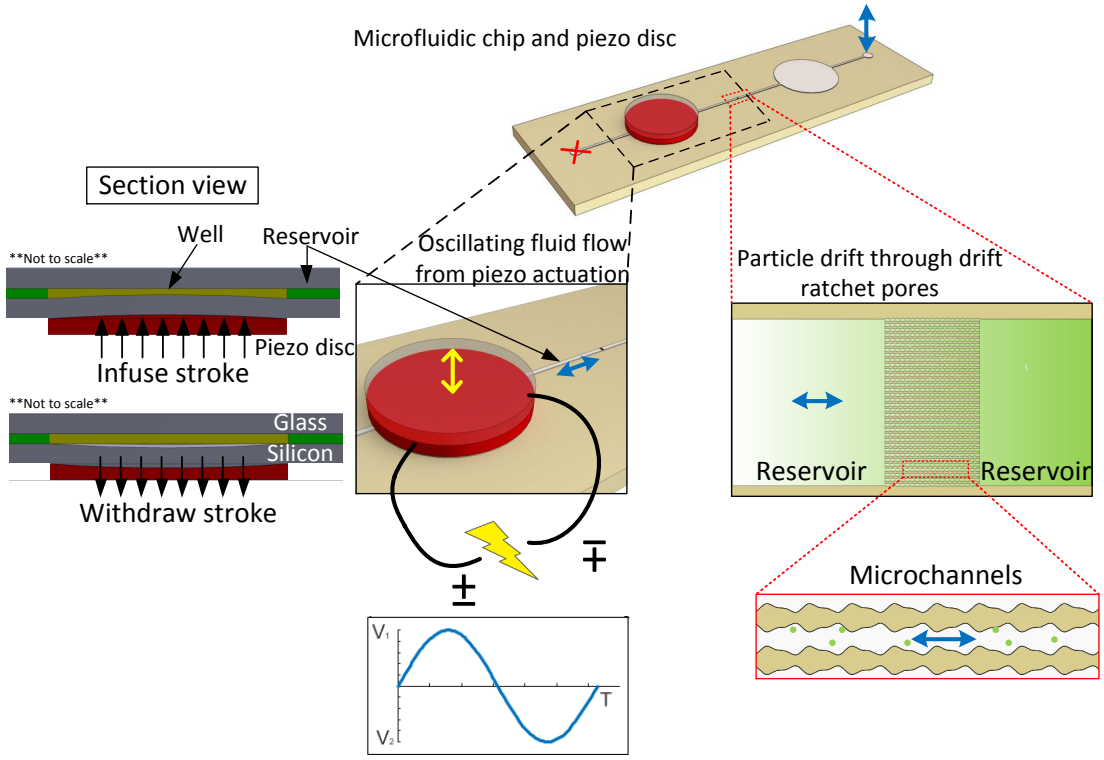

Figure 5.1 Overview of experimental procedure.

The microchannels tested were representative in shape and size of the drift ratchet membrane tested in Matthias and Muller (2003) and Mathwig et al. (2011b), except instead of an axisymmetric pore shape, a three-dimensional planar microchannel was fabricated and tested. The three-dimensional planar drift ratchet microchannel design was chosen to have the option to directly observe and quantify the particle position and particle-wall interactions responsible for this separation mechanism, to eventually improve the accuracy of numerical models as previously discussed in Section 3.1, Chapter 3. Additionally this tests whether a drift ratchet membrane could be fabricated using classic two-dimensional microfabrication techniques.

Figures 5.2 and 5.3 show the characterisation of the drift ratchet channels tested, using an optical profiler and Scanning Electron Microscopy (SEM), respectively.

A fluorescent microscope and camera were used to capture video of fluorescent microparticles moving through the drift ratchet channels under the influence of a symmetrically sinusoidal

oscillating fluid flow as shown in Figure 5.1. The focal plane at which the images were captured is half-way between the glass and the floor of the microchannels in the silicon wafer, i.e. the mid-plane of the channels.

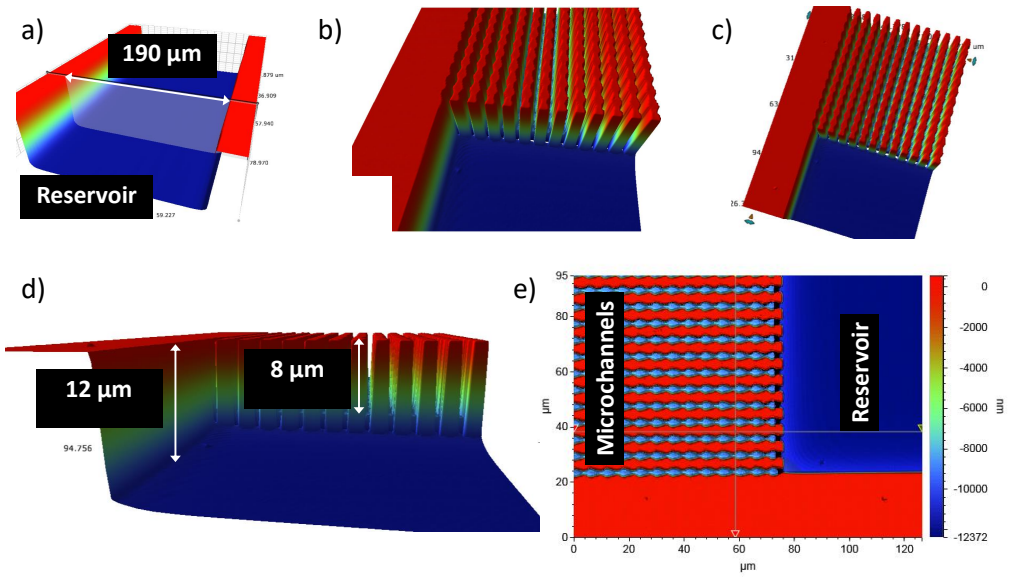

Figure 5.2 Optical profiler images of a quarter panel of the drift ratchet microchannels and reservoir either side of the drift ratchet channel bank.

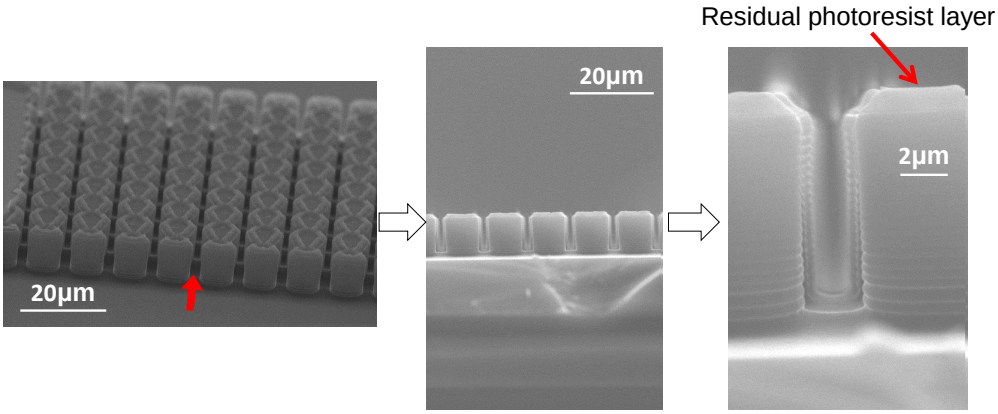

Figure 5.3 Scanning Electron Micrograph (SEM) of drift ratchet microchannels in a silicon wafer before being anodically bonded with glass to seal the channels. Disparity between the etch depth of the reservoir and drift ratchet microchannels is attributed to Deep Reactive Ion Etching (DRIE) lag.

Straight-walled channels were also fabricated and tested to ensure a control was established. Images of these straight channels, from an optical profiler, are shown in Figure 5.4.

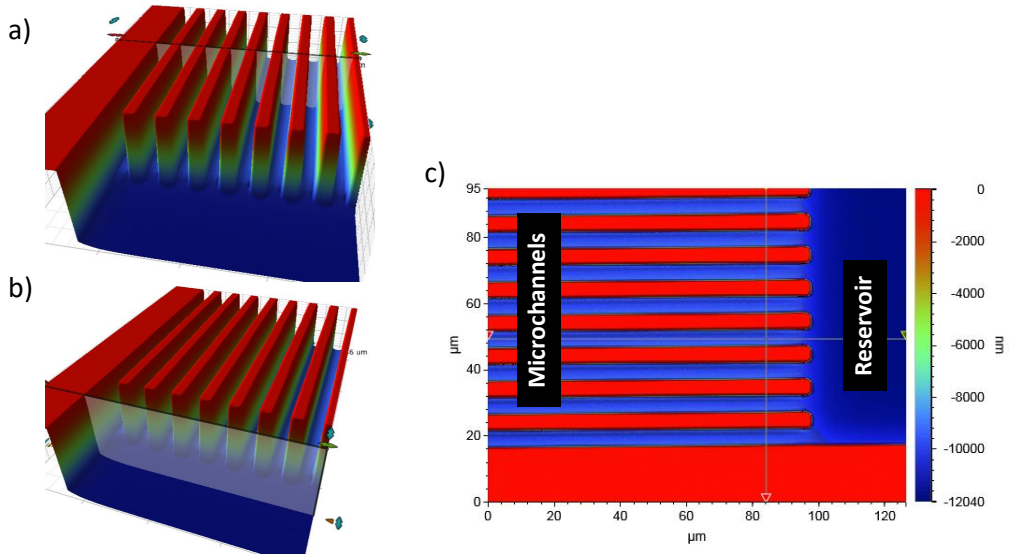

Figure 5.4 Optical profiler images of straight channels used as a control experiment.

Table 5.1 provides the main dimensions and characteristic features of the microfluidic channels experimentally tested.

Table 5.1 Parameters for the two microfluidic chips used for experiments.

	Straight-walled channels	Drift ratchet channels
Number of parallel microchannels	20	32
Number of repeating ratchet units in series	0	36
Max. channel width (μm)	5.5	4
Min. channel width (μm)	5.5	1.5
Channel depth (μm)	10	8.6
Width of reservoir (μm)	195.5	187.5
Height of reservoir (μm)	12	12.3
Channel description	Straight-walled channels to act as the control	Drift ratchet channels (Kettner et al. (2000); Matthias and Muller (2003)).

Initially, an experiment to validate the particle tracking procedure with Brownian motion within the microfluidic chip was conducted. The particle-water mixture was injected into the microfluidic chip. The setup was left to equilibrate to ensure minimal residual advection from the process of filling the microchannels. Without fluid oscillation, the fluorescent microparticles were tracked on a two-dimensional plane orthogonal to the cross-section of the microchannels, as illustrated in Figure 5.5. Conducting a particle tracking experiment with just pure particle Brownian motion present was used to validate the experimental setup by comparing the particle averaged displacement from experimental results to a theoretical predicted average particle displacement due to Brownian motion. These results are further discussed in Section 5.2.

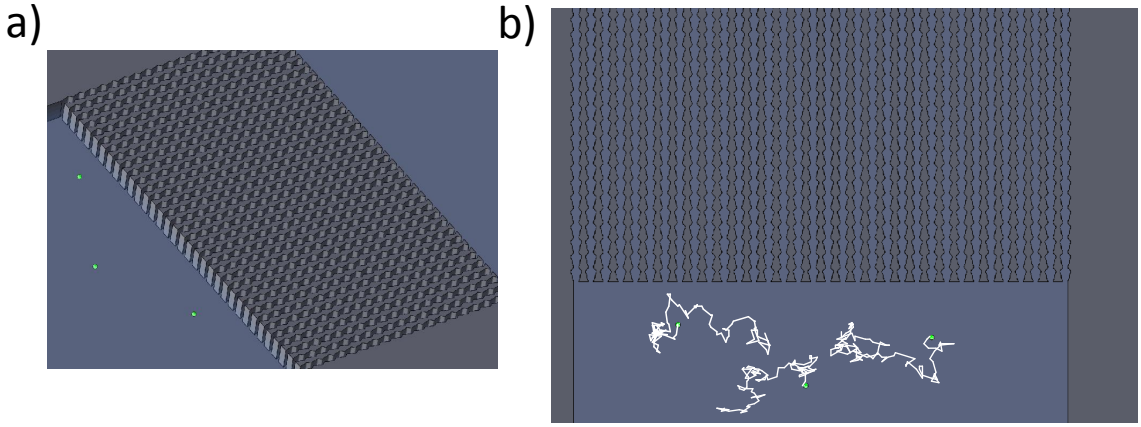

Figure 5.5 a) Schematic of bank of drift ratchet channels with small microparticles in the reservoir b) Top view of a) showing how the microparticles were tracked in two or one dimensions.

After Brownian motion validation, similar particle tracking experiments were conducted applying an oscillating fluid flow to microparticles inside straight-walled channels as well as drift ratchet channels.

5.1.1 Fabrication of Microfluidic Chip

Previous experiments concerning drift ratchets (Mathwig et al. (2011b); Matthias and Muller (2003)) used a photo-electrochemical etching technique (Mathwig et al. (2011a); Matthias et al. (2004a,b, 2005)) to form a silicon membrane containing highly parallel repeatable axisymmetric asymmetric pores to represent drift ratchet pores. The advantage of their method is that you can create drift ratchet membranes with many pores parallel to each other. The drawback from a research standpoint is that monitoring of the behaviour of microparticles within a ratchet pore and their interaction with the walls is impossible. As a result of this, three-dimensional planar drift ratchet microchannels have been etched into a $520\mu m$ thick silicon wafer using Deep Reactive Ion Etching (DRIE). The etched silicon wafer is then anodically bonded to a glass wafer to seal the microchannels. This fabrication method allows us to image the microparticles through the glass in the two end reservoirs as well as inside the drift ratchet microchannels. The microfluidic chip fabrication is illustrated in Figure 5.6.

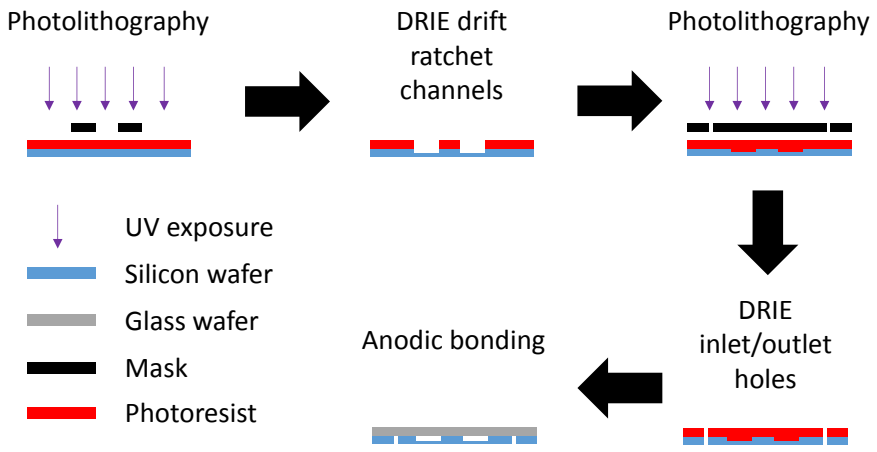

Figure 5.6 Fabrication process for the drift ratchet microchannels and inlet/outlet ports for the microfluidic chip.

Photolithography #1

To form the microchannels for the experiments, the mask shown in Figure 5.7 was patterned onto a 4 inch $\langle 100 \rangle$ silicon wafer. The photoresist, AZ5214E, was spun onto the silicon wafer to a thickness of approximately $2\mu m$, after which a hotplate softbake was undertaken for $50s$ at $110^{\circ}C$. AZ refers to the company, AZ Electronic Materials, that develops the photoresists.

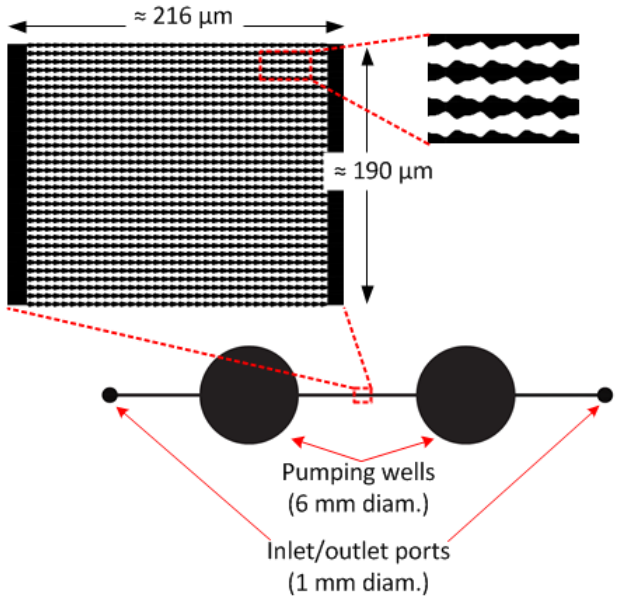

Figure 5.7 Mask pattern used for photolithography. The larger circles are the pumping wells where an externally mounted piezo disc oscillates the flow through the microchannels. The smaller holes are the inlet/outlet ports for the fluid.

Then the coated wafer was exposed to UV light in an MA6 mask aligner for $1.6s$ with the mask pattern illustrated in Figure 5.7. The now exposed wafer undergoes a further image reversal bake on the hotplate for $2min$ at $120°C$, before two UV light flood exposures each for $3.2s$ with a minute break in between. Finally, the exposed wafer was developed in AZ MIF726 until the pattern was clear on its surface ($\approx 30s$).

Deep Reactive Ion Etching (DRIE) #1

The exposed silicon pattern on the 4 inch silicon wafer was then etched using the Deep Reactive Ion Etcher (DRIE) (PlasmaPro 100 Estrelas - Oxford). The parameters for the dry etch are found in Table 5.2.

The deposition and etch stages of the dry etch procedure defined in Table 5.2 are repeated 20 times to etch to a depth of $\approx 10\mu m$. After the dry etch, a descuming process is completed to remove the residual photoresist. The parameters for this process are provided in Table 5.3.

Table 5.2 Parameters used for the first dry etch ($10\mu m$ etch) using deep reactive ion etching (DRIE).

	Time (s)	Chamber Pressure (mTorr)	RF Power (W)	ICP Power (W)	Gases (sccms)
Strike	5	0	50	1000	C_4F_8 - 50 SF_6 - 1
Deposition	6	0	15	1500	C_4F_8 - 150 SF_6 - 1
Etch	8	0	30	2000	C_4F_8 - 1 SF_6 - 150

Table 5.3 Parameters used for the descuming process to remove residual photoresist after the etching stage.

	Time (s)	Chamber Pressure (mTorr)	RF Power (W)	ICP Power (W)	Gases (sccms)
Strike	-	8	-	-	O_2 - –
Clean	300	8	50	1500	O_2 - 100

Photolithography #2

After the $10\mu m$ deep pattern etch is completed, AZ9260 photoresist is spun onto the etched silicon wafer to a depth of $\approx 10\mu m$. The coated wafer is then baked on a hotplate for $165s$ at $110^{\circ}C$ before being exposed to UV light under an MA6 mask aligner for $\approx 100s$ with the mask illustrated in Figure 5.8.

Figure 5.8 Mask pattern used for photolithography of the inlet/outlet ports is shown in black. This mask was aligned with the existing pattern from the first etch, shown in grey.

The mask is aligned to the already etched inlet/outlet ports in the silicon wafer. After exposure, the coated wafer is developed in AZ400K diluted with 4 parts deionized water until the pattern is visible on the surface of the wafer.

Deep Reactive Ion Etching (DRIE) #2

The parameters for the final deep reactive ion etch are tabulated below.

Table 5.4 Parameters used for the final dry etch (through wafer etch) using deep reactive ion etching (DRIE).

	Time (s)	Chamber Pressure (mTorr)	RF Power (W)	ICP Power (W)	Gases (sccms)
Strike	5	0	50	1000	C4F8 - 50 SF6 - 1
Deposition	6	0	15	1500	C4F8- 150 SF6 - 1
Etch	8	0	30	2000	C4F8 - 1 SF6 - 150

The deposition and etch stages of the dry etch procedure above are repeated 250 and 135 times respectively to etch all the way through the 520μm thick silicon wafer. After the dry etch, a descuming process is completed to remove the residual photoresist. The parameters for this process are provided in Table 5.5.

Table 5.5 Parameters used for the descuming process to remove residual photoresist after the etching stage.

	Time (s)	Chamber Pressure (mTorr)	RF Power (W)	ICP Power (W)	Gases (sccms)
Strike	5	0	50	1000	C4F8 - 50 SF6 - 1
Deposition	6	0	15	1500	C4F8- 150 SF6 - 1
Etch	8	0	30	2000	C4F8 - 1 SF6 - 150

Anodic bonding

Anodic bonding is required to seal the silicon microchannels, after which the only access to the microchannels will be through the inlet / outlet holes etched in the previous processing step. Before anodic bonding is completed between a 4 inch glass wafer and the etched silicon wafer, both substrates need to be cleaned thoroughly using the standard RCA1 and RCA2 cleaning procedure. RCA1 involves treating the substrates with a 5:1:1 mixture of water,

ammonium hydroxide and hydrogen peroxide at a temperature of $70°C$ for 20 minutes. This is to clean the substrate of any organic material. RCA2 involves treating the substrates with a 5:1:1 mixture of water, hydrochloric acid and hydrogen peroxide at a temperature of $70°C$ for 20 minutes. The acronym RCA refers to RCA Laboratories that has developed the cleaning procedures.
After RCA cleaning has been completed, both the glass and silicon wafers are anodically bonded together. The parameters used for anodic bonding were as follows:

- Chamber pressure was $5 \times 10^{-3} mbar$
- Temperature of the top and bottom plates were $385°C$
- Tool pressure was $2000 mbar$
- Voltage applied between plates was $-1000V$.

The etched 4-inch silicon wafer was placed underneath the 4-inch glass wafer inside the anodic bonder processing chamber.

5.1.2 Sizing of Silicon Wafer Pumping Wells

To sinusoidally pump the microparticle-fluid mixture back and forth symmetrically through the drift ratchet channels, a $6.4mm$ diameter piezo disc (PSI-5A-4E Piezo Systems Inc) was fixed onto the back of the etched well using electrical conductive epoxy as illustrated in Figure 5.9.

An AC voltage is applied to the piezo disc which then contracts or extends, based on the polarity of the voltage, exerting a force on the backside of the silicon warping it and displacing a fixed volume of fluid from the well, shown in Figure 5.1. To size the wells to account for the 1x scaled microchannels, the volume of fluid displaced from the well must be equivalent to the volume of one repeating microchannel unit summed across the bank of parallel microchannels. To calculate the volume of fluid displaced by the flexing of the backside of the silicon it was modelled as a circular plate with a fixed edge and a constant distributed force applied to it from the piezo disc. This problem has the following analytical solution for the vertical displacement, w, of a radial slice of this flexing plate (Ventsel and Krauthammer (2001)).

$$w = \left(\frac{-q}{64D}\right)\left(r_{well}^2 - r^2\right)^2 \tag{5.1}$$

Here $D = \frac{Et^3}{12(1-\nu^2)}$, E is the elastic modulus of silicon, ν is Poisson's ratio, r is the radila

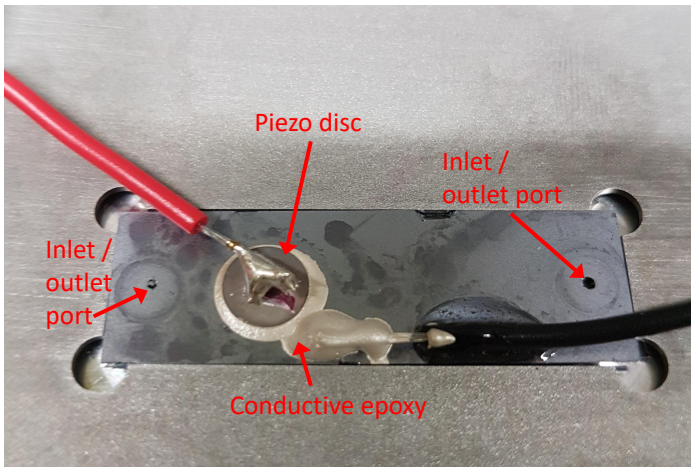

Figure 5.9 Photo of the microfluidic chip loaded into the aligner plate in the experimental setup shown in Figure 5.10. The conductive epoxy is a standard silver two-part epoxy sourced from RS online.

positon, and t and r_{well} are the thickness and radius of the backside of the silicon well, respectively. This solution is revolved around its axis to determine the change in volume of the well when the plate flexes. The constant distributed load applied by the piezo disc, q, is equal to the following expression (Piezo Systems Inc),

$$q = \left(\frac{V}{t}\right) d_{33} E_{piezo} \tag{5.2}$$

where, V, d_{33} and E_{piezo} are the applied voltage, piezoelectric "d_{33}" parameter (strain produced / electric field applied) and electric field , respectively.

Using this method the wells for the 1x scaled microchannels were calculated to be $2mm$ in diameter. This corresponds to an applied voltage of $2.4V$. The wells were designed to be $6mm$ in size to account for any discrepancies.

5.1.3 Experimental Apparatus

The experimental setup consisted of the microfluidic chip and supplementary equipment to assist with imaging of microparticles in the chip and pumping the fluid-particle mixture into the microfluidic chip. The composition of the experimental apparatus used, is described in Figure 5.10 along with an illustration of how fluorescence microscopy was used to image the microparticles. The microfluidic experimental setup described in Figure 5.10 was inspired by that from Sinclair (2012).

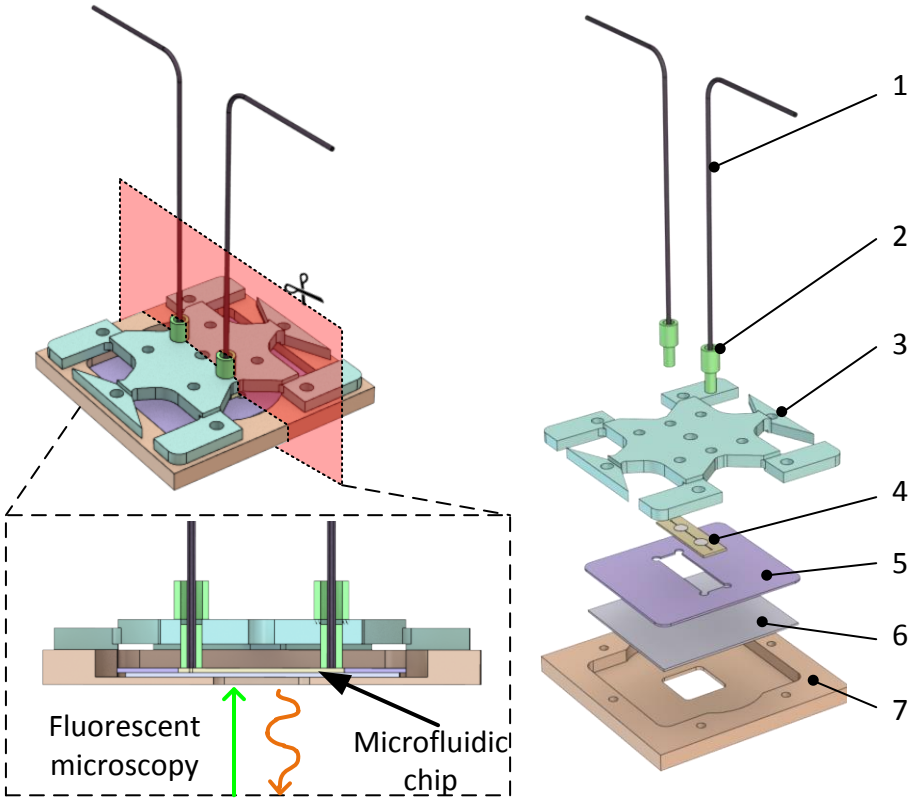

Figure 5.10 Experimental setup. 1. PEEK tubing, 2. PEEK connectors with ferrules, 3. Aluminium top plate, 4. Microfluidic chip and piezo disc assembly, 5. Aluminium aligner, 6. Glass plate and 7. Aluminium base plate.

PEEK tubing, PEEK connectors with ferrules (including inline filters) were sourced from Upchurch Scientific (IDEX Health & Science). The piezo discs were sourced from Piezo Systems Inc. All other parts were manufactured in-house; including the aluminium base and

top plate, aligner and the microfluidic chip. Technical engineering drawings for the aligner, base plate and top plate are included in Appendix C.

5.2 Particle Behaviour

Particle tracking of pure diffusion was completed to validate experiments by comparing the root mean square (R.M.S) of the total two dimensional displacement of 20 particles against the theoretical expression for Brownian motion displacement, Equation 5.3. These results are presented in Figure 5.11b. The results validate Brownian motion, with an almost average particle displacement of $0\mu m$, shown in Figure 5.11a. The disparity between the measured mean particle displacement and $0\mu m$ is due to the low number of particles. Increasing the number of particle would increase its statistical significance. Measuring more particles was not practically achievable due to the inherent difficulties encountered during experimentation.

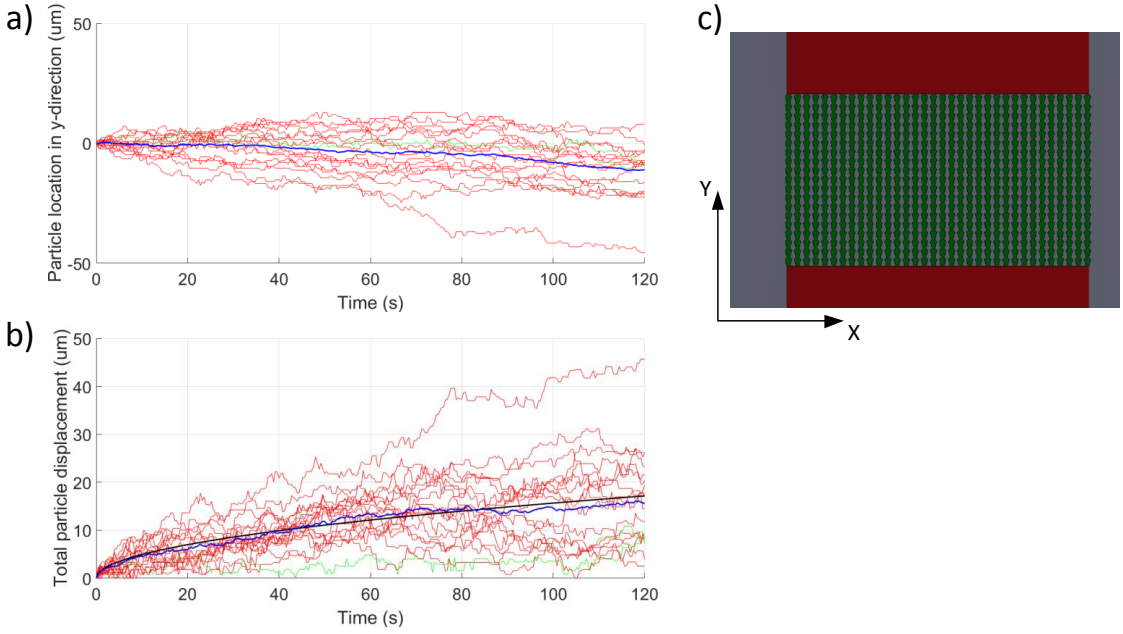

Figure 5.11 Tracking of 20 particles during pure diffusion in DI water. a) Plot of particle position with respect to the axis of the channels (Red and green lines). Particle average of these displacements (Thick blue line) b) Plot of R.M.S particle displacement over time (Red and green lines). Particle average of these displacements (Thick blue line). Theoretical expression described by Equation 5.3 (Thick black line). c) Top view schematic of channels and reservoirs defining the coordinate system. Red shaded areas are reservoirs. Green shaded areas are channels.

The particle averaged R.M.S displacement value which correlates to the theoretical values is described by the following expression (black line in Figure 5.11b),

$$L_{R.M.S} = \sqrt{4D_{fs}\Delta t}. \tag{5.3}$$

$L_{R.M.S}$ is the total R.M.S displacement over two dimensions, while D_{fs} is the free-space diffusion coefficient and Δt is the time step.

5.2.1 Straight-walled Channels

Microparticles were then oscillated in straight-walled channels at a frequency of $40Hz$, to ensure there was no drift predicted by simulation results. Particle tracking was completed as a control experiment. Figure 5.12 shows the displacement of 20 particles in the y-direction over 2 minutes, where the direction is defined along the axis of the pores, shown in Figure 5.12.
It was expected that the results for the straight-walled case would resemble that for the case of solely Brownian motion, i.e. without fluid oscillation. However, as can be seen in Figure 5.12 unidirectional fluid advection is present in the reservoirs and the channels. This could be attributed to many sources:

- If there is a small leak for the fluid to evaporate from, it will cause a hydrostatic pressure driven advection. However, this was not observed during particle tracking for the purely diffusion case which indicates that it is unlikely the cause of the advection.

- There was a possibility that the movement of the piezo disc on the back of the silicon wafer is not a symmetric process and that a certain stroke, either the withdraw or infuse stroke, is different to its reciprocal. There was a chance to offset the applied AC voltage supplied to the piezo disc to possibly negate this effect but it did not have an effect on the advection. It has been recommended to use a vibrometer in future work to measure the piezo disc oscillation, in Chapter 6.

- Residual pressure from the filling stage. This was ruled out as the pumping equipment used to fill the chip was disconnected and the system was closed off and allowed to settle before conducting any experiments.

- Thermophoresis could be responsible, however measures were taken to ensure a temperature controlled environment. Saying that, the operation of the piezo disc might have generated heat which could influence the motion of the particles.

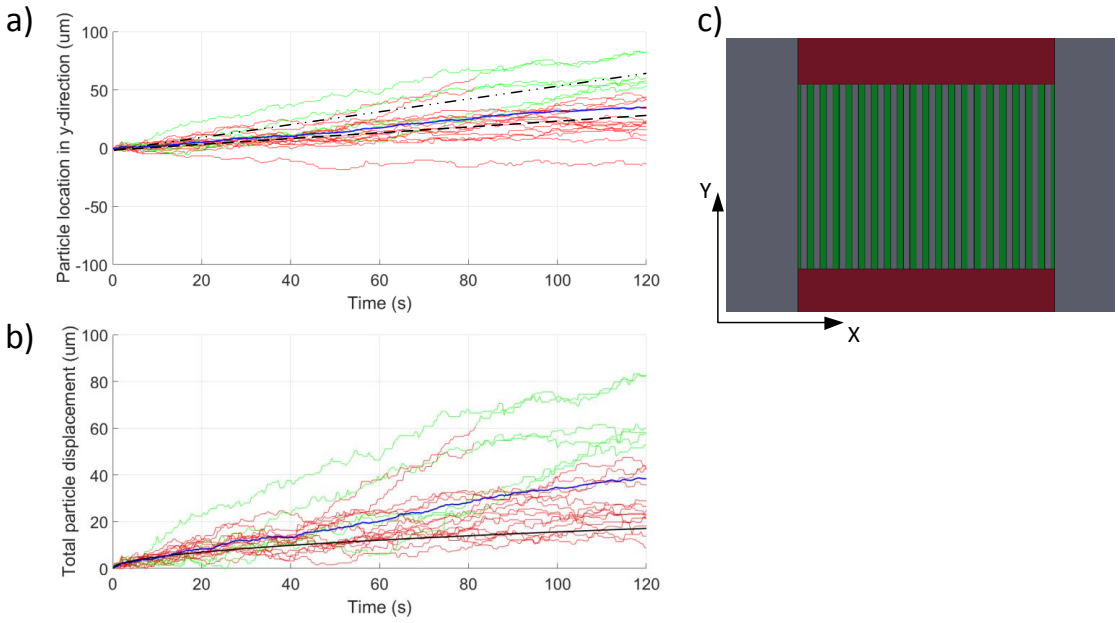

Figure 5.12 Tracking of 20 particles during fluid oscillations in straight-walled channels in DI water. a) Plot of particle position with respect to the axis of the channels (Red and green lines). Particle average of these displacements (Thick blue line). Average drift of particles within the reservoir (Dashed - Black line). Average drift of particles within the channels (Double dot dashed - Black line). b) Plot of R.M.S particle displacement over time (Red and green lines). Particle average of these displacements (Thick blue line). Theoretical expression described by Equation 5.3 (Thick black line). c) Top view schematic of channels and reservoirs defining the coordinate system. Red shaded areas are reservoirs. Green shaded areas are channels.

Figure 5.12 shows that the magnitude of particle advection or drift for the straight-walled case is different when the particles were present in the reservoir compared to when they were in the straight-walled channels. The advection of particles is associated with bulk fluid advection because it was determined that the ratio of particle velocities in the channels and in the reservoirs is similar to the ratio of the cross-sectional areas of the reservoir to that of the channels, depicted in Figure 5.13. From Figure 5.12a the average drift of particles within the reservoir (Dashed - Black line) and channels (Double dot dashed - Black line) was calculated. This ratio was then compared to the ratio of cross-sectional areas for these two regions. Based on conservation of mass these ratios should be the same if fluid advection is present.

$$\frac{A_1}{A_2} \approx \frac{V_2}{V_1}. \tag{5.4}$$

$$\frac{V_2}{V_1} = \frac{25/125}{60/120} = 0.42. \tag{5.5}$$

$$\frac{A_1}{A_2} = \frac{20 \times (5.5 \times 10)}{12 \times 195.5} = 0.48. \tag{5.6}$$

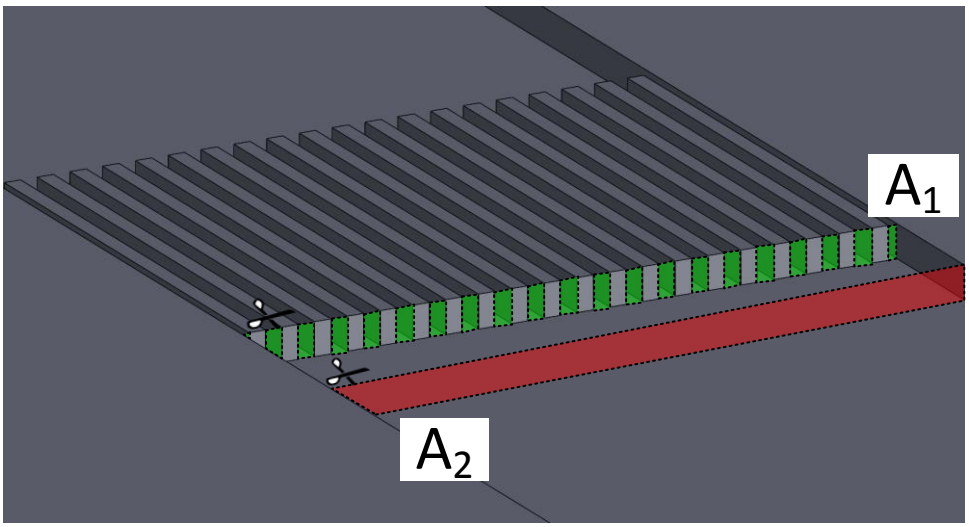

Figure 5.13 Oblique schematic view of the channels and reservoir and associated cross-sectional areas; A_1 (green shaded) and A_2 (red shaded), respectively.

If this advection through the channels is known from Equation 5.4 and assuming the net displacement over many instances of particles must be zero during symmetric fluid oscillation in straight pores then this could potentially be subtracted from the drift velocity measured in the case of the drift ratchet channels, leaving the drift velocity due to particle interaction with the asymmetric pore walls.

5.2.2 Drift Ratchet Channels

During tracking of oscillating particles within the drift ratchet channels, a similar fluid advection was experienced to that in the straight-walled case, shown in Figure 5.14. As can be seen, the particles inside the channels (green lines) drift at a higher velocity than those in the reservoir (red lines).

Similar to the method explained in the previous section the area ratio was used to calculate the bulk advection of fluid in the channels, knowing the fluid advection in the reservoir from

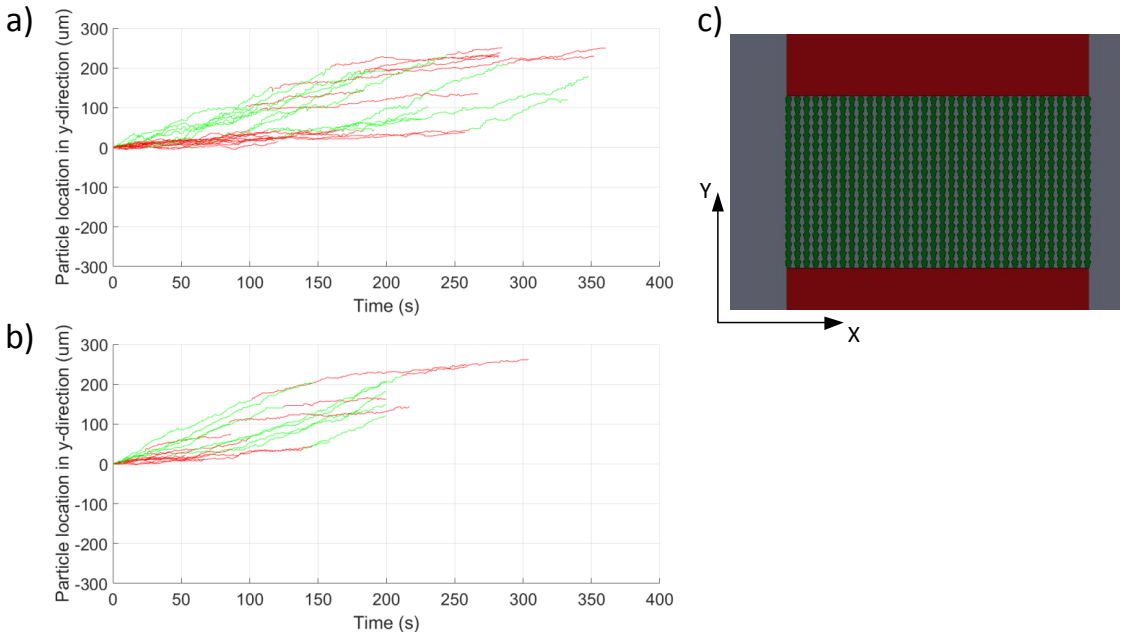

Figure 5.14 Plot of particle displacements over time along the axis of the channels, while in the reservoir (Red lines) and in the channels (Green lines). Parameters used for these experiments include; the same sized drift ratchet channels as studied by Kettner et al. (2000) and Matthias and Muller (2003), microparticles radius was $0.35\mu m$, fluid oscillation frequency of $40Hz$, fluid temperature of $293K$, type of fluid was methanol and dynamic viscosity of methanol was $0.54 \times 10^{-3} Pa.s$. a) 2x amplitude fluid oscillations. b) 1x amplitude fluid oscillations. c) Top view schematic of channels and reservoirs defining the coordinate system. Red shaded areas are reservoirs. Green shaded areas are channels.

tracking results. Table 5.6 shows the drift velocity of particles resulting from drift ratcheting, and calculated using the above method.

Table 5.6 Particle drift results from drift ratchet channel experiments processed from Figure 5.14. Particle drift is calculated along the y-axis (along axis of the drift ratchet channels).

	Measured particle drift velocity (μms^{-1})		Fluid advection (μms^{-1})	Particle drift velocity by subtracting fluid advection (μms^{-1})
	Reservoir	Channels	Channels	Channels
1x amplitude	-0.39 $\pm$0.15	-1.23 $\pm$0.2	-1.48	0.34
2x amplitude	-0.31 $\pm$0.12	-1.08 $\pm$0.19	-1.55	0.31

The "fluid advection" value in Table 5.6 refers to the adjusted value taking into account the cross-sectional area. The ratio of reservoir to microchannel cross-sectional areas is 4.8 for the drift ratchet channels. This factor was multiplied by the measured particle drift velocity in the reservoir to calculate the value for "Fluid advection". The values calculated without the fluid advection term, in Table 5.6, are different when compared to values obtained from numerical simulations which are presented in the last column in Table 5.7. The bulk fluid advection is thought to affect the interaction between microparticles and the asymmetric pore walls to an extent that diminishes the drift ratcheting mechanism. Consequently, numerical simulations accounting for bulk fluid advection superimposed onto the fluid oscillations were conducted to observe this effect. The results are provided in Figure 5.15, Figure 5.16 and Table 5.7.

The simulations are similar to those set up in Chapter 3 where the behaviour of Brownian particles is superimposed with fluid advection. However, to better represent the experimental channels being three-dimensional planar drift ratchet channels, the simulations modelled a quasi three-dimensional planar channel. The channels in the simulations did not represent axisymmetric pores but instead represented the experimental drift ratchet channels without a floor or ceiling bounding the channel. In other words, the particles were unbound in the direction perpendicular to the two-dimensional drift ratchet shape.

Figures 5.15 and 5.16 compares the case where fluid advection is superimposed onto the fluid oscillations to that where the fluid advection is omitted. The drift velocity presented in Table 5.7 shows that the drift ratcheting mechanism is diminished by bulk fluid advection. This indicates that advection must be mitigated in experiments to demonstrate whether the drift ratchet mechanism is generated in real-world scenarios.

Table 5.7 Particle drift results from drift ratchet numerical simulations representative of the experiments. The magnitude of advection was chosen to be $\approx 3\mu ms^{-1}$ as this was reflective of the order of magnitude experienced in experiments ($1-5\mu ms^{-1}$).

	Pure advection and diffusion (μms^{-1})	Pure advection, fluid oscillation and diffusion (μms^{-1})	Particle drift velocity (μms^{-1})	Particle drift velocity (fluid oscillation and diffusion) (μms^{-1}) (without advection)
1x amplitude	-3.01	-3.18	-0.17	-0.26
2x amplitude	-3.01	-3.1	-0.09	0.19

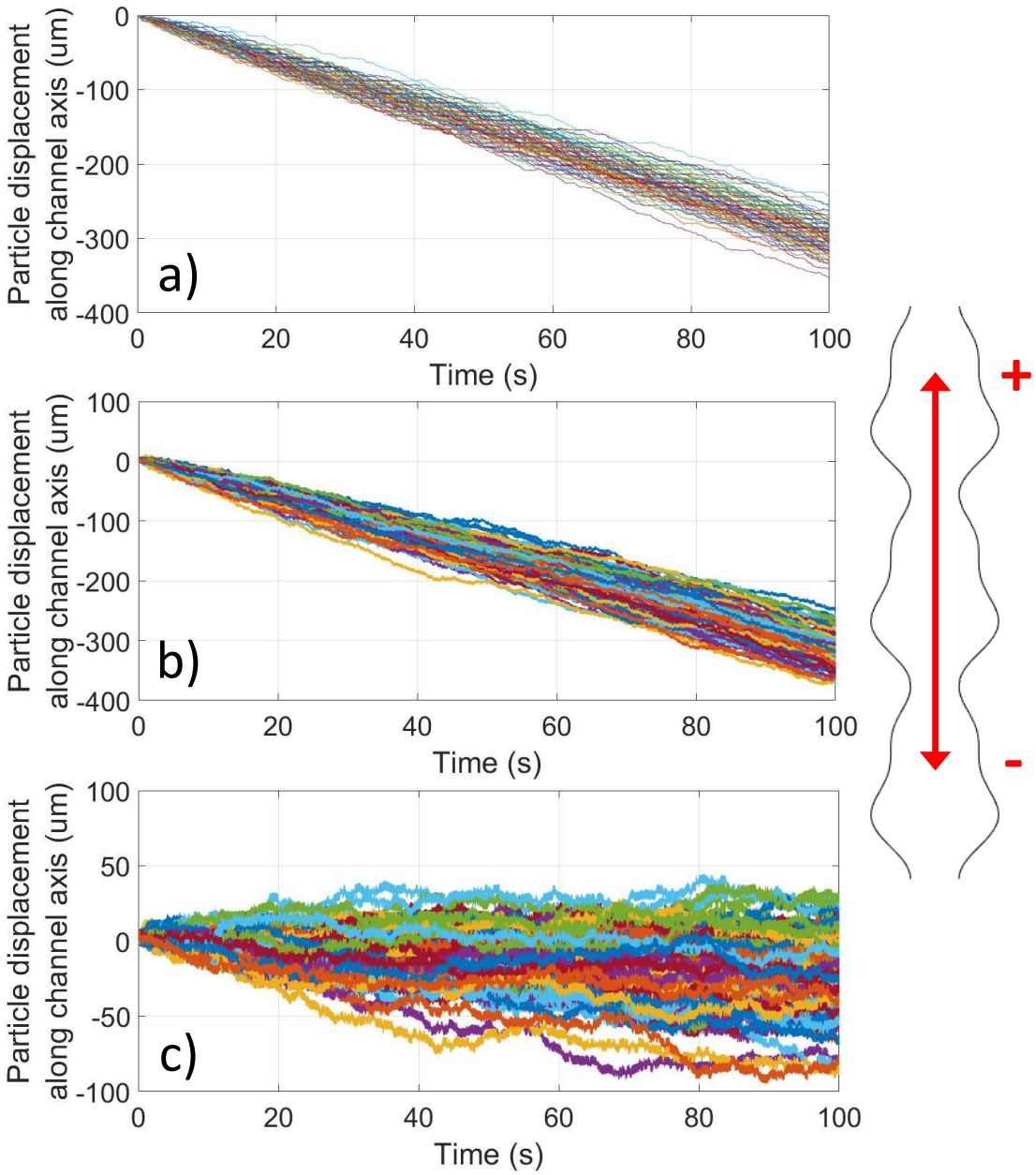

Figure 5.15 Plots 100 of particle displacements over time from numerical simulations. Simulations used the following conditions depending on whether they included fluid advection or oscillations. The same sized drift ratchet channels as studied by Kettner et al. (2000) and Matthias and Muller (2003), microparticles radius was $0.35\mu m$, fluid oscillation frequency of $40Hz$ and 1x amplitude, fluid temperature of $293K$, fluid dynamic viscosity was $0.5 \times 10^{-3} Pa.s$. a) Bulk fluid advection and diffusion. b) Bulk fluid advection, fluid oscillations and diffusion. c) Fluid oscillations and diffusion, representative of a drift ratchet.

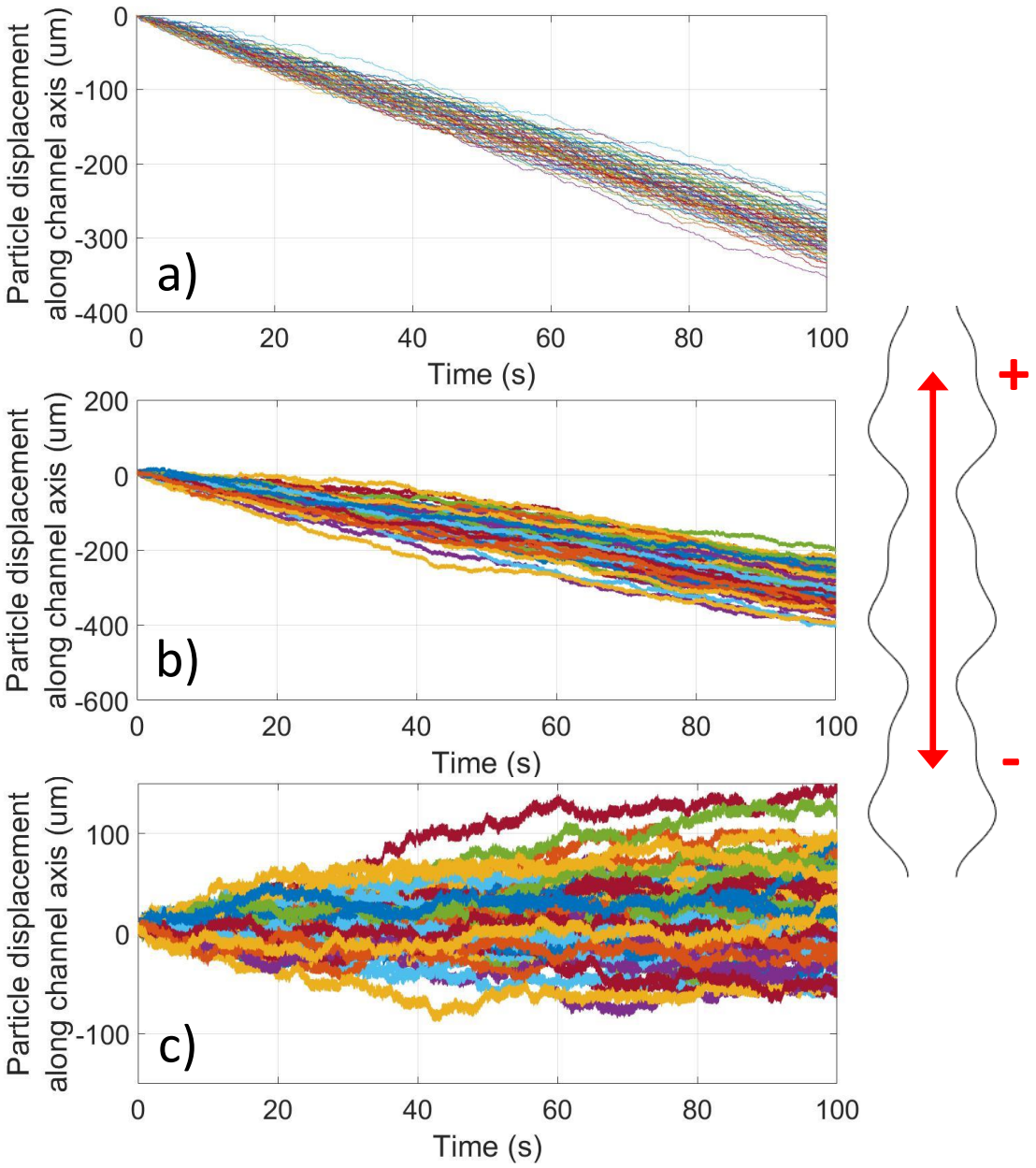

Figure 5.16 Plots of 100 particle displacements over time from numerical simulations. Simulations used the following conditions depending on whether they included fluid advection or oscillations. The same sized drift ratchet channels as studied by Kettner et al. (2000) and Matthias and Muller (2003), microparticles radius was $0.35\mu m$, fluid oscillation frequency of $40Hz$ and 2x amplitude, fluid temperature of $293K$, fluid dynamic viscosity was $0.5 \times 10^{-3} Pa.s$. a) Bulk fluid advection and diffusion. b) Bulk fluid advection, fluid oscillations and diffusion. c) Fluid oscillations and diffusion, representative of a drift ratchet.

5.3 Experimental Uncertainty

Uncertainty analysis involves the evaluation of errors associated with the experimental procedures, measurements and equipment. This is used to determine a range of values within which the true value measured, will lie (Coleman and Steele (2009)).

5.3.1 Experimental Uncertainty Theory

Estimation of experimental uncertainty in the following sections is based on the works by Coleman and Steele (2009) and Stern et al. (1999). When a parameter is measured during experimental work there is a difference when compared to the true value of that parameter. This variation can be attributed to systematic error and random error. Systematic error does not vary while measurements are being taken, while random error does vary. For the case of finding the total uncertainty, U_r, associated with a multiple variable function such as, $r = r(X_1, X_2, X_3, X_4, ..., X_n)$, the root sum of squares is used,

$$U_r^2 = B_r^2 + P_r^2. \tag{5.7}$$

Where, B_r is the bias (systematic) error and P_r is precision (random) error.
The bias error used in Equation 5.7 is calculated by,

$$B_r^2 = \sum_{i=1}^{J} \left(\frac{\partial r}{\partial X_i} \right)^2 B_{X_i}^2. \tag{5.8}$$

Where, $B_{X_i}^2$ are the systematic standard uncertainties.
Likewise, the precision error can be calculated using,

$$P_r^2 = \sum_{i=1}^{J} \left(\frac{\partial r}{\partial X_i} \right)^2 P_{X_i}^2. \tag{5.9}$$

Where, $P_{X_i} = tS_{X_i}$, S_{X_i} are the standard deviations for the measurement of each X_i variable, while t is the statistical coverage factor. Occasionally, when X_i variables have the same time-varying error source, then the precision error can be estimated by,

$$P_r = tS_r \tag{5.10}$$

and used directly in Equation 5.7.

5.3.2 Microchannel and Reservoir Cross-Section Measurement Uncertainty

The depth and width of the microchannels and reservoirs were measured using an optical profiler and scanning electron microscope. The uncertainty in measuring these dimensions was estimated to be within $\pm 0.5 \mu m$.

5.3.3 Camera Time Resolution Uncertainty

The resolution of the frame rate of the camera used to image the fluorescent particles provided the bias error associated with timing of the frames from the video. This bias error was $\pm 10 ns$, and was provided by the manufacturer LaVision. The time between frames in the particle tracking videos was $0.4 s$.

5.3.4 Image Processing Uncertainty

Individual particles were manually tracked. This position was then stored and a plot of particle displacement with respect to time generated. The accuracy of a mouse click to the correct location of the particle was calculated to be within 4 pixels of where the particle centre was located. A single pixel represents $0.4 \mu m$ in a single image, meaning the maximum bias error associated with tracking of the particle using this method is $\pm 1.6 \mu m$ for particle tracking in one-dimension and $\pm 2.26 \mu m$ for the total displacement over two-dimensions. The average total displacements along the y-axis in Figure 5.14 across individual particles were; $134.76 \mu m$ and $37.9 \mu m$ for the 1x amplitude case for particles inside the microchannels and reservoir, respectively. While for the 2x amplitude case the displacements were; $148.65 \mu m$ and $37.63 \mu m$ for particles inside the microchannels and reservoir, respectively.

5.3.5 Particle Drift Velocity Uncertainty

Random Brownian motion is an inherent and critical component of the drift ratchet mechanism. As such, the standard deviations of the spread of individual particle drift velocities will not be included in the error here. However, they have been given in Table 5.6. Therefore, the main bias errors associated with these experiments are the processing of the images during particle tracking and the time resolution of the fluorescent camera. Considering the above information, the equation for particle drift velocity, v_{drift}, only has 2 variables to consider for bias error. The initial and final y-position of a particle in a given video frame, y_2 and y_1, respectively, and the timing accuracy of the camera, Δt. The error associated with the

positions of y_2 and y_1 can be transferred to a single variable, the displacement difference, Δy, by doubling the error associated with a single y-position.

$$v_{drift} = \frac{\Delta y}{\Delta t} \tag{5.11}$$

Thus the total uncertainty of the drift velocity is given by,

$$U^2_{v_{drift}} = \left(\frac{\partial v_{drift}}{\partial \Delta y}\right)^2 U^2_{\Delta y} + \left(\frac{\partial v_{drift}}{\partial \Delta t}\right)^2 U^2_{\Delta t} \tag{5.12}$$

$$\left(\frac{U_{v_{drift}}}{v_{drift}}\right)^2 = (1)^2 \left(\frac{U_{\Delta y}}{\Delta y}\right)^2 + (1)^2 \left(\frac{U_{\Delta t}}{\Delta t}\right)^2. \tag{5.13}$$

While, Table 5.8 provides the percentage error associated with the drift velocity in measurements for the 1x and 2x amplitudes and in the reservoirs and the microchannels.

Table 5.8 Percentage error in the particle drift velocity due to errors in determining particle centre position and camera timing resolution.

	Drift velocity uncertainty (%)	
	Reservoir	Channels
1x amplitude	±8.4	±2.4
2x amplitude	±8.5	±2.1

5.4 Channel Fouling

As can be seen in Figure 5.17, particle fouling in the drift ratchet experiments was a problem during the filling stage of the experimental process.

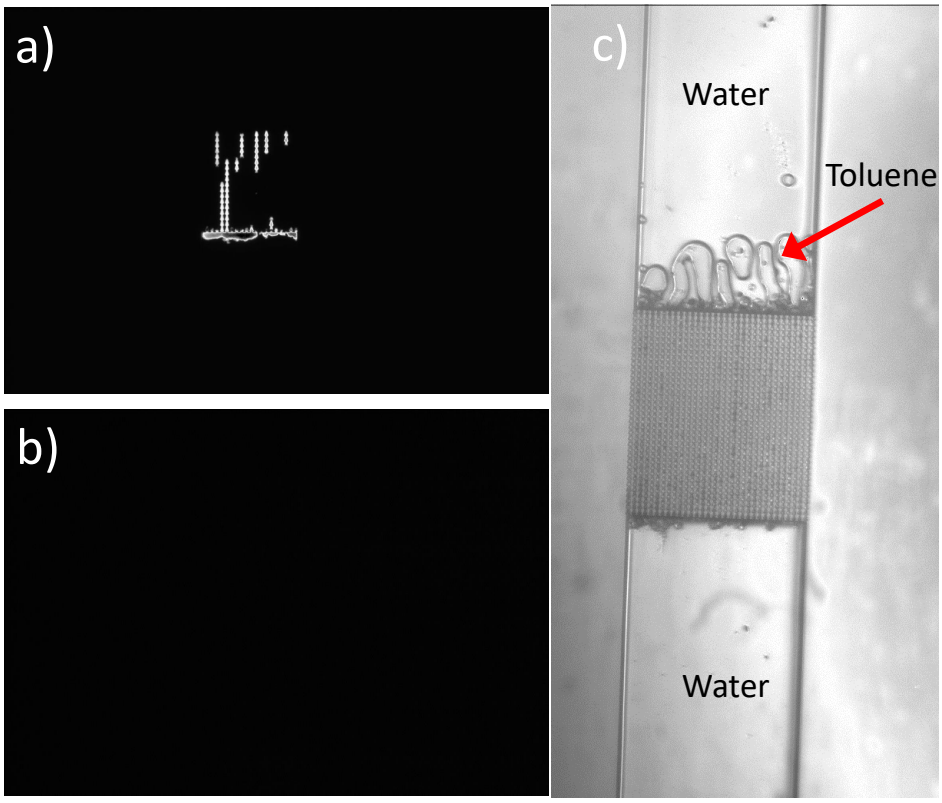

Figure 5.17 Fluorescent image of microparticle fouling in drift ratchet microchannel array. Microparticle diameter of $0.7\mu m$ and a minimum channel diameter of $3\mu m$ in this case. b) Fluorescent image of the same drift ratchet array after cleaning with toluene. c) Light microscopy image of immiscible toluene with water stuck at the exit of the drift ratchet channel array.

As a result of the trouble experienced in the filling stage a cleaning procedure was developed to ensure reusability of the microfluidic chips.

Cleaning procedure:

- Acetone or IPA were not used to clean out polystyrene microparticles from channels. If these solutions were used, channels were flushed with DI water before using them. Acetone and IPA were believed to melt the polystyrene microparticles instead of completely dissolving them. This then increased the likelihood of fouling.
- Used toluene and chloroform to dissolve fouled microparticles.

- Used DI water to flush before injecting particle solution to prevent subsequent dissolving of microparticles.

However, as can be seen in Figure 5.17c the toluene was difficult to remove from the microchannels as it is immiscible with DI water. Ethanol was then used as an intermediate flushing solution to remove the toluene and the water was then used to remove the ethanol.

5.5 Summary of Findings

This chapter has demonstrated the fabrication of a novel hydrodynamic drift ratchet device using conventional microfabrication techniques such as deep reactive ion etching (DRIE) and anodic bonding. This unique drift ratchet channel design allowed the observation of the interactions between oscillating microparticles and the asymmetric pore wall of the drift ratchet. However, time constraints and equipment availability did not allow the quantification of these interactions. This work can be completed in future work and the information obtained could be used to improve hydrodynamic drift ratchet numerical simulations. This work also lead to the discovery that bulk fluid advection can diminish the drift ratchet mechanism and is unwanted in experiments. Improvements to negate bulk fluid advection and fouling of this drift ratchet design will be further discussed in Chapter 6.

Chapter 6

Conclusions and Perspective

6.1 Key Findings

This research found that it is unlikely that the girdle band pores of the diatom species, *Coscinodiscus sp.*, act as a hydrodynamic drift ratchet, and therefore do not use this as a mechanism to separate nutrients from harmful particles found in their marine environment. This is due to the small size of the girdle band pores where diffusion becomes too dominant a transport mechanism, diminishing the drift ratchet mechanism. This investigation also highlighted that the small number of repeating ratchet units in series with one another has an effect on particle drift. As such, the 1-2 girdle band pore units in series would not be able to generate the particle drift of a hydrodynamic drift ratchet.

Although the theory of whether a girdle band pore uses the drift ratchet mechanism was disproved, this work proposes an alternative theory on how diatoms get that edge over their more motile competitors in their ecosystem. Termed "Hydrodynamic Immunity" the theory offers diffusiophoresis as a mechanism to transport small nutrients and trace elements toward the cell while providing protection against larger particles such as pathogens, pollutants and poisons. Figures 4.8, 4.9 and 4.10 illustrate the suggested workings of "Hydrodynamic Immunity".

As a part of this work comparing the girdle band pore to a hydrodynamic drift ratchet, a numerical model was developed to describe the behaviour of a microparticle within a previously studied hydrodynamic drift ratchet pore. This model was also used to demonstrate the dynamic similarity of a hydrodynamic drift ratchet, highlighting the important dimensionless numbers in Chapter 3. This can be used to design future hydrodynamic drift ratchet experiments as well as comparing results from dynamically similar experiments.

Finally, this research demonstrated the fabrication of a novel hydrodynamic drift ratchet microfluidic device. This showed that conventional microfabrication techniques such as

photolithography, deep reactive ion etching and anodic bonding can be used in the fabrication of these microfluidic devices. Results from the experiments were inconclusive as to whether the system developed was working as a hydrodynamic drift ratchet. The results were promising but even minuscule amounts of bulk flow had the effect of reducing the drift. Future experiments need to ensure that undesirable bulk fluid advection is eliminated.

6.2 Recommendations for Future Work

1. More particles are needed to be tested in the drift ratchet experiments to get an improved ensemble average for the particle drift.

2. There is a need to better understand the effect of the natural forcings characteristic of the ocean environment on the dead-end flow through the girdle band pore generated by diffusiophoresis, i.e. can natural fluctuations cause mixing between the inflow and outflow of the diffusiophoretic flow.

3. While the planar three-dimensional pores studied in experiments detailed in Chapter 5 are a useful research tool, an axisymmetric pore would be a more effective drift ratchet due to the absence of flat pore walls. As such, there is the potential to use a Nanoscribe to either 3D print full or half axisymmetric drift ratchet pores such as the half pore shown in Figure 6.1.

   The three-dimensional planar pores do serve the purpose of being able to quantify the interactions between the pore walls and microparticles which is the event that is responsible for the rectification of particles and could be used to improve future numerical models. However, as Figure 6.1 shows, future work is required to optimise the settings to ensure smoother walls.

4. To reduce the likelihood of fouling during the stage of filling up the microfluidic chip a number of design changes could be implemented:

   - Introduce more or deeper pores into the drift ratchet membrane in the microfluidic chip shown in Figure 5.7. This will reduce the velocity of the fluid-particle mixture during filling preventing clumping and crowding of particles entering the bank of pores during filling.
   - Introduce a smoother entry into and out of the drift ratchet pores to ensure there are no recirculation regions during the high velocity filling of the microfluidic chip. Figure 6.2 shows a possible inlet design.

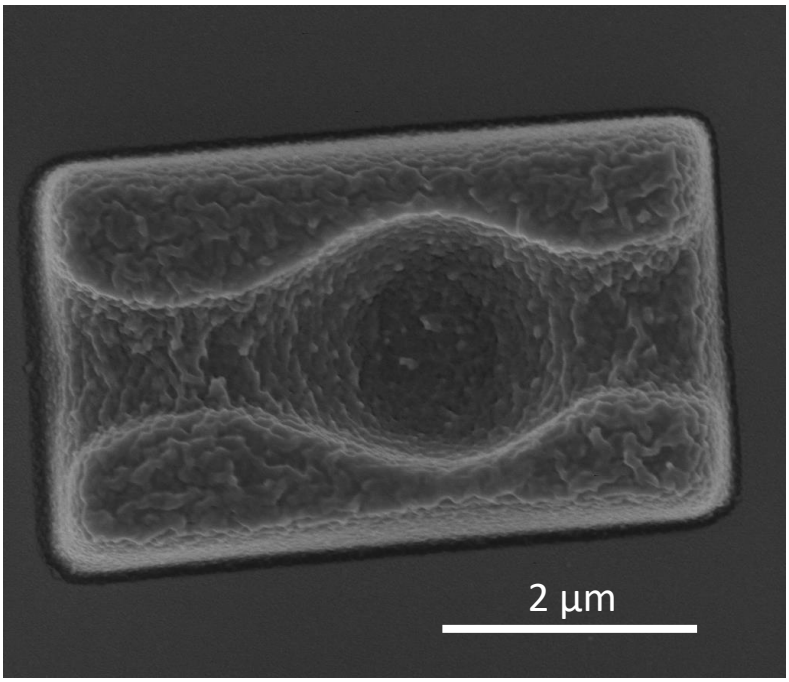

Figure 6.1 Scanning electron micrograph of nanoscribed diatom girdle band pore - half profile (Top view).

- Alter the pH of the fluid to prevent the aggregation of microparticles and subsequent blocking of channels.

5. Use a vibrometer to measure displacement of the piezo disc to ensure the oscillation of the fluid is symmetric.

6. Use a heat sink / thermal imaging camera to test for thermophoresis to check whether this is responsible for the bulk fluid advection which has an effect on the drift ratchet mechanism.

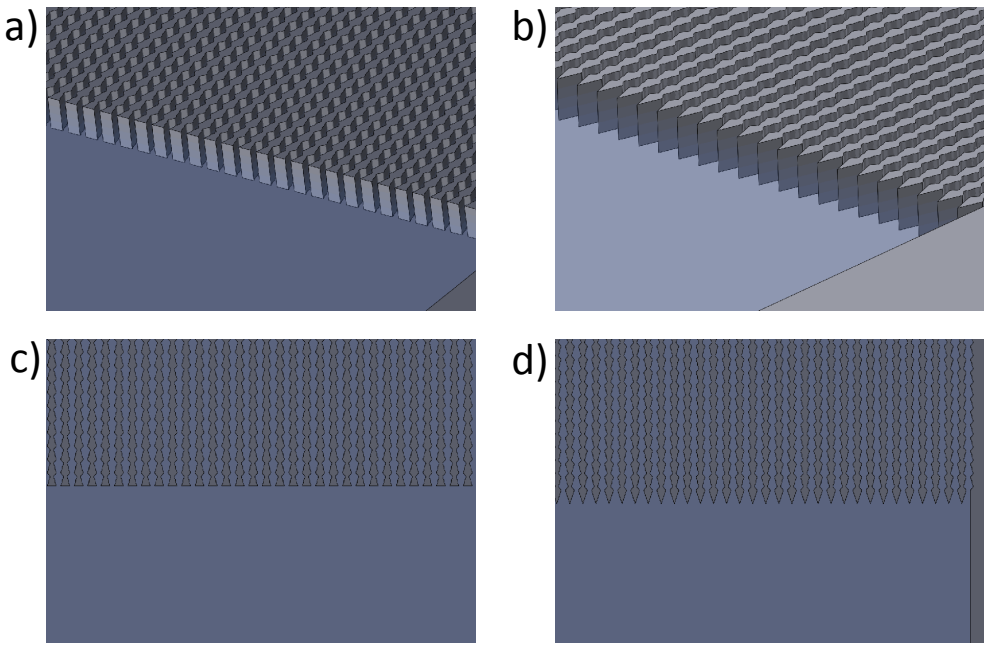

Figure 6.2 a) and c) Isometric and top view schematic of the original entry/exit to the drift ratchet pore bank, respectively. b) and d) Isometric and top view schematic of the new proposed entry/exit to the drift ratchet pore bank, respectively.

References

Ai, B.-q. and Liu, L.-g. (2008). A channel brownian pump powered by an unbiased external force. *The Journal of chemical physics*, 128(2):024706.

Aksnes, D. and Egge, J. (1991). A theoretical model for nutrient uptake in phytoplankton. *Marine ecology progress series. Oldendorf*, 70(1):65–72.

Alford, M. H. (2003). Redistribution of energy available for ocean mixing by long-range propagation of internal waves. *Nature*, 423(6936):159–162.

Alford, M. H., Peacock, T., MacKinnon, J. A., Nash, J. D., Buijsman, M. C., Centuroni, L. R., Chao, S.-Y., Chang, M.-H., Farmer, D. M., Fringer, O. B., et al. (2015). The formation and fate of internal waves in the south china sea. *Nature*, 521(7550):65–69.

Alvain, S., Moulin, C., Dandonneau, Y., and Loisel, H. (2008). Seasonal distribution and succession of dominant phytoplankton groups in the global ocean: A satellite view. *Global Biogeochemical Cycles*, 22(3):n/a–n/a. GB3001.

Anderson, L. W. J. and Sweeney, B. M. (1978). Role of inorganic ions in controlling sedimentation rate of a marine centric diatom ditylum brightwelli1,2. *Journal of Phycology*, 14(2):204–214.

Armbrust, E. (2009). The life of diatoms in the world's oceans. *Nature*, 459(7244):185–192.

Azam, F. and Malfatti, F. (2007). Microbial structuring of marine ecosystems. *Nature Reviews Microbiology*, 5(10):782–791.

Balasubramanian, A. K., Soni, K. A., Beskok, A., and Pillai, S. D. (2007). A microfluidic device for continuous capture and concentration of microorganisms from potable water. *Lab Chip*, 7:1315–1321.

Ban, S., Burns, G., Castel, J., Chaudron, Y., Christou, R., Escribano, R., Umani, S., Gasparini, S., Ruiz, F., Hoffmeyer, M., Lanora, A., Kang, H., Laabir, M., Lacoste, A., Miralto, A., Ning, X., Poulet, S., and Smetacek, V. (1999). Diatoms and the ocean carbon cycle. *Protist*, 150(1):25–32.

Barron, W. C., Young, J. A., Munson, R. E., et al. (1982). New concept-high density brine filtration utilizing a diatomaceous earth filtration system. In *SPE Formation Damage Control Symposium*. Society of Petroleum Engineers.

Batchelor, G. (1959). Small-scale variation of convected quantities like temperature in turbulent fluid part 1. general discussion and the case of small conductivity. *Journal of Fluid Mechanics*, 5(01):113–133.

Berg, H. and Purcell, E. (1977). Physics of chemoreception. *Biophysical Journal*, 20(2):193–219.

Bhardwaj, P., Bagdi, P., and Sen, A. K. (2011). Microfluidic device based on a micro-hydrocyclone for particle-liquid separation. *Lab Chip*, 11:4012–4021.

Bhatta, H., Enderlein, J., and Rosengarten, G. (2009a). Fluorescence correlation spectroscopy to study diffusion through diatom nanopores. *Journal of Nanoscience and Nanotechnology*, 9(11):6760–6766.

Bhatta, H., Kong, T.-K., and Rosengarten, G. (2009b). Diffusion through diatom nanopores. *Journal of Nano Research*, 7:69–74.

Blanchet, A., Dolbeault, J., and Kowalczyk, M. (2009). Stochastic stokes' drift, homogenized functional inequalities, and large time behavior of brownian ratchets. *SIAM Journal on Mathematical Analysis*, 41(1):46–76.

Boyd, C. M. and Gradmann, D. (1999a). Electrophysiology of the marine diatom coscinodiscus wailesii i. endogenous changes of membrane voltage and resistance. *Journal of experimental botany*, 50(333):445–452.

Boyd, C. M. and Gradmann, D. (1999b). Electrophysiology of the marine diatom coscinodiscus wailesii iii. uptake of nitrate and ammonium. *Journal of experimental botany*, 50(333):461–467.

Brenk, M., Bungartz, H.-J., Mehl, M., Muntean, I., Neckel, T., and Weinzierl, T. (2008). Numerical simulation of particle transport in a drift ratchet. *SIAM Journal on Scientific Computing*, 30(6):2777–2798.

Brenner, B., Hostetter, T., and Humes, H. (1978). Glomerular permselectivity: barrier function based on discrimination of molecular size and charge. *The American journal of physiology*, 234(6):F455–460.

Burada, P. S., Hanggi, P., Marchesoni, F., Schmid, G., and Talkner, P. (2009). Diffusion in confined geometries. *ChemPhysChem*, 10(1):45–54.

Carbajal-Tinoco, M. D., Lopez-Fernandez, R., and Arauz-Lara, J. L. (2007). Asymmetry in colloidal diffusion near a rigid wall. *Phys. Rev. Lett.*, 99:138303.

Cardenas, M. (2008). Three-dimensional vortices in single pores and their effects on transport. *Geophysical Research Letters*, 35(18).

Cermeño, P., Dutkiewicz, S., Harris, R., Follows, M., Schofield, O., and Falkowski, P. (2008). The role of nutricline depth in regulating the ocean carbon cycle. *Proceedings of the National Academy of Sciences of the United States of America*, 105(51):20344–20349.

Chen, C.-C., Chen, Y.-A., Liu, Y.-J., and Yao, D.-J. (2014). A multilayer concentric filter device to diminish clogging for separation of particles and microalgae based on size. *Lab Chip*, 14:1459–1468.

CHEN, H., LIU, Y., ZHANG, H., YU, L., ZHU, Y., and LI, D. (2010). Separation and manipulation of rare-earth oxide particles by dielectrophoresis. *Chinese Journal of Chemical Engineering*, 18(6):1034 – 1037.

Chen, T. and Xu, C. (2017). Control-oriented modeling of colloid transport by solute gradients in dead-end channels. *Asia-Pacific Journal of Chemical Engineering*, 12(2):247–258. APJ-16-0407.R1.

Cheri, M. S., Latifi, H., Khashei, H., and Seresht, M. J. (2014). Focusing and continuous separation of microparticles by insulator-based dielectrophoresis (idep) in stair-shaped microchannel. *ELECTROPHORESIS*, 35(24):3523–3532.

Choi, E., Kim, B., and Park, J. (2009). High-throughput microparticle separation using gradient traveling wave dielectrophoresis. *Journal of Micromechanics and Microengineering*, 19(12):125014.

Coleman, H. W. and Steele, W. G. (2009). *Experimentation, validation, and uncertainty analysis for engineers*. John Wiley & Sons.

Conkright, M. E., Locarnini, R. A., Garcia, H. E., O'Brien, T. D., Boyer, T. P., Stephens, C., and Antonov, J. I. (2002). *World Ocean Atlas 2001: Objective analyses, data statistics, and figures: CD-ROM documentation*. US Department of Commerce, National Oceanic and Atmospheric Administration, National Oceanographic Data Center, Ocean Climate Laboratory.

De Tommasi, E., De Stefano, L., Rea, I., Moretti, L., De Stefano, M., and Rendina, I. (2008). Light micro-lensing effect in biosilica shells of diatoms microalgae. volume 6992.

Denman, K. and Gargett, A. (1995). Biological-physical interactions in the upper ocean: The role of vertical and small scale transport processes. *Annual Review of Fluid Mechanics*, 27(1):225–255.

Edwards, K. F., Thomas, M. K., Klausmeier, C. A., and Litchman, E. (2012). Allometric scaling and taxonomic variation in nutrient utilization traits and maximum growth rate of phytoplankton. *Limnology and Oceanography*, 57(2):554–566.

Eijkel, J. C. and van den Berg, A. (2005). Nanofluidics: what is it and what can we expect from it? *Microfluidics and Nanofluidics*, 1(3):249–267.

Eijkel, J. C. T. and van den Berg, A. (2006). The promise of nanotechnology for separation devices – from a top-down approach to nature-inspired separation devices. *ELECTROPHORESIS*, 27(3):677–685.

Eppley, R., Holmes, R., and Strickland, J. (1967). Sinking rates of marine phytoplankton measured with a fluorometer. *Journal of Experimental Marine Biology and Ecology*, 1(2):191–208.

Eppley, R. W., Rogers, J. N., and McCarthy, J. J. (1969). Half-saturation constants for uptake of nitrate and ammonium by marine phytoplankton1. *Limnology and Oceanography*, 14(6):912–920.

Eppley, R. W. and Thomas, W. H. (1969). Comparison of half-saturation constants for growth and nitrate uptake of marine phytoplankton 2. *Journal of Phycology*, 5(4):375–379.

Çetin, B., Özer, M. B., and Solmaz, M. E. (2014). Microfluidic bio-particle manipulation for biotechnology. *Biochemical Engineering Journal*, 92:63 – 82. Advances in Bioprocess Technology.

Falkowski, P. G. (1975). Nitrate uptake in marine phytoplankton: Comparison of half-saturation constants from seven species1. *Limnology and Oceanography*, 20(3):412–417.

Farrah, S., Preston, D., Toranzos, G., Girard, M., Erdos, G., and Vasuhdivan, V. (1991). Use of modified diatomaceous earth for removal and recovery of viruses in water. *Applied and Environmental Microbiology*, 57(9):2502–2506.

Ferrari, R. and Wunsch, C. (2009). Ocean circulation kinetic energy: Reservoirs, sources, and sinks. *Annual Review of Fluid Mechanics*, 41(1):253–282.

Fisher, A. E. (1995). *The Relationship Between Irradiance (quantity, Quality and Photoperiod), Sinking Rate and Carbohydrate Content in Two Marine Diatoms*. PhD thesis, University of British Columbia.

Fuhrmann, T., Landwehr, S., El Rharbl-Kucki, M., and Sumper, M. (2004). Diatoms as living photonic crystals. *Applied Physics B: Lasers and Optics*, 78(3-4):257–260.

Gavis, J. (1976). Munk and riley revisited: Nutrient diffusion transport and rates of phytoplankton growth. *Journal of Marine Research*, 34(2):161–179.

Gemmell, B. J., Oh, G., Buskey, E. J., and Villareal, T. A. (2016). Dynamic sinking behaviour in marine phytoplankton: rapid changes in buoyancy may aid in nutrient uptake. *Proceedings of the Royal Society of London B: Biological Sciences*, 283(1840).

Golshaei, B. and Najafi, A. (2015). Rectified motion in an asymmetric channel the role of hydrodynamic interactions with walls. *Physics Review E*, 91(2).

Goodrich, J., Sanderson, S., Batjakas, I., and Kaufman, L. (2000). Branchial arches of suspension-feeding oreochromis esculentus: Sieve or sticky filter? *Journal of Fish Biology*, 56(4):858–875.

Gradmann, D. and Boyd, C. (2000). Three types of membrane excitations in the marine diatom coscinodiscus wailesii. *Journal of Membrane Biology*, 175(2):149–160.

Gradmann, D. and Boyd, C. M. (1999a). Electrophysiology of the marine diatom coscinodiscus wailesii ii. potassium currents. *Journal of experimental botany*, 50(333):453–459.

Gradmann, D. and Boyd, C. M. (1999b). Electrophysiology of the marine diatom coscinodiscus wailesii iv: types of non-linear current-voltage-time relationships recorded with single saw-tooth voltage-clamp experiments. *European Biophysics Journal*, 28(7):591–599.

Gregg, M. C. (1973). The microstructure of the ocean. *Scientific American*, 228:64–77.

Grenvall, C., Augustsson, P., Matsuoka, H., and Laurell, T. (2008). Multiple node ultrasonic standing wave separation in microchannels improves lipid discrimination from complex bio-suspensions. In *The Proceedings of the MicroTAS Conference*.

Gross, F. and Zeuthen, E. (1948). The buoyancy of plankton diatoms: a problem of cell physiology. *Proceedings of the Royal Society of London. Series B-Biological Sciences*, 135(880):382–389.

Guasto, J., Rusconi, R., and Stocker, R. (2011). Fluid mechanics of planktonic microorganisms. *Annual Review of Fluid Mechanics*, 44:373–400.

Hale, M. and Mitchell, J. (2001a). Functional morphology of diatom frustule microstructures: Hydrodynamic control of brownian particle diffusion and advection. *Aquatic Microbial Ecology*, 24(3):287–295.

Hale, M. and Mitchell, J. (2001b). Motion of submicrometer particles dominated by brownian motion near cell and microfabricated surfaces. *Nano Letters*, 1(11):617–623.

Hale, M. and Mitchell, J. (2002). Effects of particle size, flow velocity, and cell surface microtopography on the motion of submicrometer particles over diatoms. *Nano Letters*, 2(6):657–663.

Hamm, C. (2005). The evolution of advanced mechanical defenses and potential technological applications of diatom shells. *Journal of nanoscience and nanotechnology*, 5(1):108–119.

Hamm, C., Merkel, R., Springer, O., Jurkojc, P., Maiert, C., Prechtelt, K., and Smetacek, V. (2003). Architecture and material properties of diatom shells provide effective mechanical protection. *Nature*, 421(6925):841–843.

Happel, J. and Brenner, H. (2012). *Low Reynolds number hydrodynamics: with special applications to particulate media*, volume 1. Springer Science and Business Media.

Harrison, P., Parslow, J., and Conway, H. (1989). Determination of nutrient uptake kinetic parameters: a comparison of methods. *Marine ecology progress series. Oldendorf*, 52(3):301–312.

Herringer, J. W., Lester, D. R., Dorrington, G. E., Rosengarten, G., and Mitchell, J. G. (2017). Hydrodynamic drift ratchet scalability. *AIChE Journal*, 63(6):2358–2366.

Hill, P. (1992). Reconciling aggregation theory with observed vertical fluxes following phytoplankton blooms. *Journal of Geophysical Research*, 97(C2):2295–2308.

Hochella Jr., M., Lower, S., Maurice, P., Penn, R., Sahai, N., Sparks, D., and Twining, B. (2008). Nanominerals, mineral nanoparticles, and earth systems. *Science*, 319(5870):1631–1635.

Hoshyargar, V., Nezameddin Ashrafizadeh, S., and Sadeghi, A. (2016). Diffusioosmotic flow in rectangular microchannels. *ELECTROPHORESIS*, 37(5-6):809–817.

Hsu, S.-H., Paoletti, C., Torres, M., Ritchie, R., Larkum, A., and Grillet, C. (2012). Light transmission of the marine diatom coscinodiscus wailesii. volume 8339.

Ingalls, A., Whitehead, K., and Bridoux, M. (2010). Tinted windows: The presence of the uv absorbing compounds called mycosporine-like amino acids embedded in the frustules of marine diatoms. *Geochimica et Cosmochimica Acta*, 74(1):104–115.

Iranifam, M. (2013). Analytical applications of chemiluminescence-detection systems assisted by magnetic microparticles and nanoparticles. *TrAC Trends in Analytical Chemistry*, 51:51 – 70.

Islam, N., Bradshaw-Hajek, B., Miklavcic, S., and White, L. (2015). The onset of recirculation flow in periodic capillaries: Geometric effects. *European Journal of Mechanics - B/Fluids*, 53:119 – 128.

Jeffery, G. B. (1922). The motion of ellipsoidal particles immersed in a viscous fluid. *Proceedings of the Royal Society of London A: Mathematical, Physical and Engineering Sciences*, 102(715):161–179.

Jimenez, M. and Bridle, H. L. (2015). Angry pathogens, how to get rid of them: introducing microfluidics for waterborne pathogen separation to children. *Lab Chip*, 15:947–957.

Jimenez, M., Miller, B., and Bridle, H. L. (2017). Efficient separation of small microparticles at high flowrates using spiral channels: Application to waterborne pathogens. *Chemical Engineering Science*, 157:247 – 254. 12th International Conference on Gas-Liquid and Gas-Liquid-Solid Reactor Engineering.

Jubery, T. Z., Srivastava, S. K., and Dutta, P. (2014). Dielectrophoretic separation of bioparticles in microdevices: A review. *ELECTROPHORESIS*, 35(5):691–713.

Jumars, P. A. (1993). *Concepts in Biological Oceanography: An Interdisciplinary Primer*. Oxford University Press.

Jumars, P. A., Deming, J. W., Hill, P. S., Karp-Boss, L., Yager, P. L., and Dade, W. B. (1993). Physical constraints on marine osmotrophy in an optimal foraging context. *Aquatic Microbial Ecology*, 7(2):121–159.

Jung and Kwak, H.-Y. (2007). Separation of microparticles and biological cells inside an evaporating droplet using dielectrophoresis. *Analytical Chemistry*, 79(13):5087–5092. PMID: 17523596.

Kamykowski, D. and Zentara, S.-J. (1985). Nitrate and silicic acid in the world ocean: patterns and processes. *Mar. Ecol. Prog. Ser*, 26(1-2):47–59.

Karp-Boss, L., Boss, E., Jumars, P., et al. (1996). Nutrient fluxes to planktonic osmotrophs in the presence of fluid motion. *Oceanography and Marine Biology*, 34:71–108.

Karp-Boss, L. and Jumars, P. A. (1998). Motion of diatom chains in steady shear flow. *Limnology and Oceanography*, 43(8):1767–1773.

Keh, H. J. and Ma, H. C. (2004). Diffusioosmosis of electrolyte solutions in fine capillaries. *Colloids and Surfaces A: Physicochemical and Engineering Aspects*, 233(1):87 – 95.

Kettner, C., Reimann, P., Hänggi, P., and Müller, F. (2000). Drift ratchet. *Physical Review E*, 61(1):312.

Khashan, S. A., Dagher, S., Alazzam, A., Mathew, B., and Hilal-Alnaqbi, A. (2017). Microdevice for continuous flow magnetic separation for bioengineering applications. *Journal of Micromechanics and Microengineering*, 27(5):055016.

Kim, S. and Karrila, S. J. (2013). *Microhydrodynamics: principles and selected applications*. Courier Dover Publications.

Kiørboe, T. (1993). Turbulence, phytoplankton cell size, and the structure of pelagic food webs. *Advances in Marine Biology*, 29(C):1–72.

Kiørboe, T. (2008). *A mechanistic approach to plankton ecology*. Princeton University Press.

KoehlI, M., Jumars, P. A., and Karp-Boss, L. (2003). Algal biophysics.

Kolmogorov, A. (1941). *Dokl. Akad. Nauk SSSR*, 30:301–305.

Kolmogorov, A. N. (1991). Dissipation of energy in the locally isotropic turbulence. *Proceedings of the Royal Society of London A: Mathematical, Physical and Engineering Sciences*, 434(1890):15–17.

Kondratyev, S., Urbano, J. M., and Vorotnikov, D. (2016). On the bulk velocity of brownian ratchets. *SIAM J. Math. Analysis*, 48:950–980.

Kooistra, W. H., Gersonde, R., Medlin, L. K., and Mann, D. G. (2007). Chapter 11 - the origin and evolution of the diatoms: Their adaptation to a planktonic existence. In Falkowski, P. G. and Knoll, A. H., editors, *Evolution of Primary Producers in the Sea*, pages 207 – 249. Academic Press, Burlington.

Kucki, M. and Fuhrmann-Lieker, T. (2012). Staining diatoms with rhodamine dyes: control of emission colour in photonic biocomposites. *Journal of The Royal Society Interface*, 9(69):727–733.

Lazier, J. and Mann, K. (1989). Turbulence and the diffusive layers around small organisms. *Deep Sea Research Part A, Oceanographic Research Papers*, 36(11):1721–1733.

Lewin, J. (1961). The dissolution of silica from diatom walls. *Geochimica et Cosmochimica Acta*, 21(3-4):182–198.

Lin, C.-Y., Chen, F., Yeh, L.-H., and Hsu, J.-P. (2016). Salt gradient driven ion transport in solid-state nanopores: the crucial role of reservoir geometry and size. *Phys. Chem. Chem. Phys.*, 18:30160–30165.

Liu, C., Stakenborg, T., Peeters, S., and Lagae, L. (2009). Cell manipulation with magnetic particles toward microfluidic cytometry. *Journal of Applied Physics*, 105(10):102014.

Losic, D., Mitchell, J., and Voelcker, N. (2009). Diatomaceous lessons in nanotechnology and advanced materials. *Advanced Materials*, 21(29):2947–2958.

Losic, D., Pillar, R., Dilger, T., Mitchell, J., and Voelcker, N. (2007a). Atomic force microscopy (afm) characterisation of the porous silica nanostructure of two centric diatoms. *Journal of Porous Materials*, 14(1):61–69.

Losic, D., Rosengarten, G., Mitchell, J., and Voelcker, N. (2006). Pore architecture of diatom frustules: Potential nanostructured membranes for molecular and particle separations. *Journal of Nanoscience and Nanotechnology*, 6(4):982–989.

Losic, D., Short, K., Mitchell, J., Lal, R., and Voelcker, N. (2007b). Afm nanoindentations of diatom biosilica surfaces. *Langmuir*, 23(9):5014–5021.

Ma, H. C. and Keh, H. J. (2006). Diffusioosmosis of electrolyte solutions in a fine capillary slit. *Journal of Colloid and Interface Science*, 298(1):476 – 486.

Makhnovskii, Y. A., Zitserman, V. Y., and Antipov, A. E. (2012). Directed transport of a brownian particle in a periodically tapered tube. *Journal of Experimental and Theoretical Physics*, 115(3):535–549.

Marañón, E. (2015). Cell size as a key determinant of phytoplankton metabolism and community structure. *Annual Review of Marine Science*, 7(1):241–264. PMID: 25062405.

Marbà, N., Duarte, C. M., and Agustí, S. (2007). Allometric scaling of plant life history. *Proceedings of the National Academy of Sciences*, 104(40):15777–15780.

Martens, S., Schmid, G., Schimansky-Geier, L., and Hänggi, P. (2011). Biased brownian motion in extremely corrugated tubes. *Chaos*, 21(4).

Martens, S., Schmid, G., Straube, A., Schimansky-Geier, L., and Hanggi, P. (2013). How entropy and hydrodynamics cooperate in rectifying particle transport. *European Physical Journal: Special Topics*, 222(10):2453–2463.

Martínez-García, S. and Karl, D. M. (2015). Microbial respiration in the euphotic zone at station aloha. *Limnology and Oceanography*, 60(3):1039–1050.

Mathwig, K., Geilhufe, M., Müller, F., and Gösele, U. (2011a). Bias-assisted koh etching of macroporous silicon membranes. *Journal of Micromechanics and Microengineering*, 21(3):035015.

Mathwig, K., Mueller, F., and Goesele, U. (2011b). Particle transport in asymmetrically modulated pores. *New Journal of Physics*, 13.

Matthias, S., Müller, F., Jamois, C., Wehrspohn, R., and Gösele, U. (2004a). Large-area three-dimensional structuring by electrochemical etching and lithography. *Advanced Materials*, 16(23-24):2166–2170.

Matthias, S. and Muller, F. (2003). Asymmetric pores in a silicon membrane acting as massively parallel brownian ratchets. *Nature*, 424(6944):53–57.

Matthias, S., Muller, F., Hillebrand, R., Schilling, J., and Gosele, U. (2004b). Three-dimensional silicon-based photonic crystals fabricated by electrochemical etching. In *First IEEE International Conference on Group IV Photonics, 2004.*, pages 168–170.

Matthias, S., Müller, F., Schilling, J., and Gösele, U. (2005). Pushing the limits of macroporous silicon etching. *Applied Physics A*, 80(7):1391–1396.

Mehl, M., Brenk, M., Bungartz, H.-J., Daubner, K., Muntean, I. L., and Neckel, T. (2008). An eulerian approach for partitioned fluid–structure simulations on cartesian grids. *Computational Mechanics*, 43(1):115–124.

Melkikh, A. and Bessarab, D. (2010). Model of active transport of ions through diatom cell biomembrane. *Bulletin of Mathematical Biology*, 72(7):1912–1924.

Menden-Deuer, S. and Lessard, E. (2000). Carbon to volume relationships for dinoflagellates, diatoms, and other protist plankton. *Limnology and Oceanography*, 45(3):569–579.

Miklasz, K. and Denny, M. (2010). Diatom sinking speeds: Improved predictions and insight from a modified stoke's law. *Limnology and Oceanography*, 55(6):2513–2525.

Milligan, A. and Morel, F. (2002). A proton buffering role for silica in diatoms. *Science*, 297(5588):1848–1850.

Mitchell, J., Okubo, A., and Fuhrman, J. (1985). Microzones surrounding phytoplankton form the basis for a stratified marine microbial ecosystem. *Nature*, 316(6023):58–59.

Mitchell, J. G., Seuront, L., Doubell, M. J., Losic, D., Voelcker, N. H., Seymour, J., and Lal, R. (2013). The role of diatom nanostructures in biasing diffusion to improve uptake in a patchy nutrient environment. *PloS one*, 8(5).

Mojica, K. D. A., van de Poll, W. H., Kehoe, M., Huisman, J., Timmermans, K. R., Buma, A. G. J., van der Woerd, H. J., Hahn-Woernle, L., Dijkstra, H. A., and Brussaard, C. P. D. (2015). Phytoplankton community structure in relation to vertical stratification along a north-south gradient in the northeast atlantic ocean. *Limnology and Oceanography*, 60(5):1498–1521.

Moore, J. and Villareal, T. (1996). Buoyancy and growth characteristics of three positively buoyant marine diatoms. *Marine Ecology Progress Series*, 132(1-3):203–213.

Morant-Manceau, A., Nguyen, T., Pradier, E., and Tremblin, G. (2007). Carbonic anhydrase activity and photosynthesis in marine diatoms. *European Journal of Phycology*, 42(3):263–270.

Morel, F. M., Hudson, R. J., and Price, N. M. (1991). Limitation of productivity by trace metals in the sea. *Limnology and Oceanography*, 36(8):1742–1755.

Motz, T., Schmid, G., Hänggi, P., Reguera, D., and Rubí, J. M. (2014). Optimizing the performance of the entropic splitter for particle separation. *The Journal of Chemical Physics*, 141(7).

Munk, W. H. and Riley, G. A. (1952). Absorption of nutrients by aquatic plants. *Marine Research*, 11:215–240.

Musielak, M., Karp-Boss, L., Jumars, P., and Fauci, L. (2009). Nutrient transport and acquisition by diatom chains in a moving fluid. *Journal of Fluid Mechanics*, 638:401–421.

Nagasaki, K. (2008). Dinoflagellates, diatoms, and their viruses. *Journal of Microbiology*, 46(3):235–243.

Nam, J., Lim, H., Kim, D., Jung, H., and Shin, S. (2012). Continuous separation of microparticles in a microfluidic channel via the elasto-inertial effect of non-newtonian fluid. *Lab Chip*, 12:1347–1354.

Nejad, H. R., Samiei, E., Ahmadi, A., and Hoorfar, M. (2015). Gravity-driven hydrodynamic particle separation in digital microfluidic systems. *RSC Adv.*, 5:35966–35975.

Ngomsik, A.-F., Bee, A., Draye, M., Cote, G., and Cabuil, V. (2005). Magnetic nano- and microparticles for metal removal and environmental applications: a review. *Comptes Rendus Chimie*, 8(6):963 – 970.

Noyes, J., Sumper, M., and Vukusic, P. (2008). Light manipulation in a marine diatom. *Journal of Materials Research*, 23(12):3229–3235.

Paasche, E. (1973). Silicon and the ecology of marine plankton diatoms. ii. silicate-uptake kinetics in five diatom species. *Marine Biology*, 19(3):262–269.

Pahlow, M., Riebesell, U., and Wolf-Gladrow, D. (1998). Impact of cell shape and chain formation on nutrient acquisition by marine diatoms. *Limnology and Oceanography*, 42(8):1660–1672.

Pasciak, W. J. and Gavis, J. (1974). Transport limitation of nutrient uptake in phytoplankton. *Limnol. Oceanogr*, 19(6):881–888.

Pascual García, C., Burchardt, A. D., Carvalho, R. N., Gilliland, D., C. António, D., Rossi, F., and Lettieri, T. (2014). Detection of silver nanoparticles inside marine diatom <italic>thalassiosira pseudonana</italic> by electron microscopy and focused ion beam. *PLoS ONE*, 9(5):e96078.

Perkins, G. and Jones, R. (1992). Hydrodynamic interaction of a spherical particle with a planar boundary: Ii. hard wall. *Physica A: Statistical Mechanics and its Applications*, 189(3–4):447 – 477.

Prakash, S., Piruska, A., Gatimu, E., Bohn, P., Sweedler, J., and Shannon, M. (2008). Nanofluidics: Systems and applications. *IEEE Sensors Journal*, 8(5):441–450.

Prieve, D. C., Anderson, J. L., Ebel, J. P., and Lowell, M. E. (1984). Motion of a particle generated by chemical gradients. part 2. electrolytes. *Journal of Fluid Mechanics*, 148:247–269.

Prieve, D. C. and Roman, R. (1987). Diffusiophoresis of a rigid sphere through a viscous electrolyte solution. *J. Chem. Soc., Faraday Trans. 2*, 83:1287–1306.

Raven, J. and Waite, A. (2004). The evolution of silicification in diatoms: Inescapable sinking and sinking as escape? *New Phytologist*, 162(1):45–61.

Reguera, D., Luque, A., Burada, P., Schmid, G., Rub, J., and Hanggi, P. (2012). Entropic splitter for particle separation. *Physical Review Letters*, 108(2).

Reid Jr, J. L. (1965). Intermediate waters of the pacific ocean. Technical report, DTIC Document.

Roberts, A. M. (1981). Hydrodynamics of protozoan swimming. *Biochemistry and physiology of protozoa*, 4:5–66.

Rosengarten, G. (2009). Can we learn from nature to design membranes? the intricate pore structure of the diatom. Number PART B, pages 1371–1378.

Round, F. E., Crawford, R. M., and Mann, D. G. (1990). *The diatoms: biology & morphology of the genera*. Cambridge University Press.

Sajeesh, P. and Sen, A. K. (2014). Particle separation and sorting in microfluidic devices: a review. *Microfluidics and Nanofluidics*, 17(1):1–52.

Salafi, T., Zeming, K. K., and Zhang, Y. (2017). Advancements in microfluidics for nanoparticle separation. *Lab Chip*, 17:11–33.

Schindler, M., Talkner, P., Kostur, M., and Hänggi, P. (2007). Accumulating particles at the boundaries of a laminar flow. *Physica A: Statistical Mechanics and its Applications*, 385(1):46 – 58.

Schmid, A.-M. (1994). Aspects of morphogenesis and function of diatom cell walls with implications for taxonomy. *Protoplasma*, 181(1-4):43–60.

Schoch, R., Han, J., and Renaud, P. (2008). Transport phenomena in nanofluidics. *Reviews of Modern Physics*, 80(3):839–883.

Schuler, P. F., Ghosh, M. M., and Gopalan, P. (1991). Slow sand and diatomaceous earth filtration of cysts and other particulates. *Water research*, 25(8):995–1005.

Seuront, L. (2005). Hydrodynamic and tidal controls of small-scale phytoplankton patchiness. *Marine Ecology Progress Series*, 302:93–101.

Shin, S., Um, E., Sabass, B., Ault, J. T., Rahimi, M., Warren, P. B., and Stone, H. A. (2016). Size-dependent control of colloid transport via solute gradients in dead-end channels. *Proceedings of the National Academy of Sciences*, 113(2):257–261.

Sinclair, Alexander, M. . M. E. F. o. E. U. (2012). Steady and oscillatory flow in the entrance region of microchannels.

Smayda, T. (1971). Normal and accelerated sinking of phytoplankton in the sea. *Marine Geology*, 11(2):105–122.

Smayda, T. J. (1970). The suspension and sinking of phytoplankton in the sea. *Marine Biology Annual Review*, 8.

Smayda, T. J. (1998). Patterns of variability characterizing marine phytoplankton, with examples from narragansett bay. *ICES Journal of Marine Science: Journal du Conseil*, 55(4):562–573.

Smetacek, V. (2000). The giant diatom dump. *Nature*, 406(6796):574–575.

Sournia, A. (1982). Form and function in marine phytoplankton. *Biological Reviews*, 57(3):347–394.

Srajer, J., Majlis, B., and Gebeshuber, I. (2009). Microfluidic simulation of a colonial diatom chain reveals oscillatory movement. *Acta Botanica Croatica*, 68(2):431–441.

Stern, F., Muste, M., Beninati, M.-L., and Eichinger, W. E. (1999). Summary of experimental uncertainty assessment methodology with example. Technical report, IIHR Report.

Stocker, R. (2012). Marine microbes see a sea of gradients. *Science*, 338(6107):628–633.

Stroock, A., Dertinger, S., Ajdari, A., Mezić, I., Stone, H., and Whitesides, G. (2002). Chaotic mixer for microchannels. *Science*, 295(5555):647–651.

Sunda, W. and Huntaman, S. (1997). Interrelated influence of iron, light and cell size on marine phytoplankton growth. *Nature*, 390(6658):389–392.

Swan, J. W. and Brady, J. F. (2011). The hydrodynamics of confined dispersions. *Journal of Fluid Mechanics*, 687:254–299.

Taylor, A. (2009). A fast na+/ca2+-based action potential in a marine diatom. *PLoS ONE*, 4(3).

Tennekes, H. and Lumley, J. L. (1972). *A first course in turbulence*. MIT press.

Tortell, P., Reinfelder, J., and Morel, F. (1997). Active uptake of bicarbonate by diatoms [8]. *Nature*, 390(6657):243–244.

Uz, B., Yoder, J., and Osychny, V. (2001). Pumping of nutrients to ocean surface waters by the action of propagating planetary waves. *Nature*, 409(6820):597–600.

Velegol, D., Garg, A., Guha, R., Kar, A., and Kumar, M. (2016). Origins of concentration gradients for diffusiophoresis. *Soft Matter*, 12:4686–4703.

Ventsel, E. and Krauthammer, T. (2001). *Thin plates and shells: theory: analysis, and applications*. CRC press.

Verdy, A., Follows, M., and Flierl, G. (2009). Optimal phytoplankton cell size in an allometric model. *Marine Ecology Progress Series*, 379:1–12.

Von Stosch, H.-A. (1981). Structural and histochemical observations on the organic layers of the diatom cell wall. In *Proceedings of the 6th Symposium of recent and fossil diatoms, Budapest 1980*, pages 231–248.

Waite, A., Fisher, A., Thompson, P., and Harrison, P. (1997). Sinking rate versus cell volume relationships illuminate sinking rate control mechanisms in marine diatoms. *Marine Ecology Progress Series*, 157:97–108.

Walsby, A. E. and Holland, D. P. (2006). Sinking velocities of phytoplankton measured on a stable density gradient by laser scanning. *Journal of The Royal Society Interface*, 3(8):429–439.

Wheeler, P. A., Glibert, P. M., and McCarthy, J. J. (1982). Ammonium uptake and incorporation by chesapeake bay phytoplankton: short term uptake kinetics.

Williams, R. G. and Follows, M. J. (2011). *Ocean dynamics and the carbon cycle: Principles and mechanisms*. Cambridge University Press.

Wischmeyer, A., Del Amo, Y., Brzezinski, M., and Wolf-Gladrow, D. (2003). Theoretical constraints on the uptake of silicic acid species by marine diatoms. *Marine Chemistry*, 82(1-2):13–29.

Yamanaka, S., Yano, R., Usami, H., Hayashida, N., Ohguchi, M., Takeda, H., and Yoshino, K. (2008). Optical properties of diatom silica frustule with special reference to blue light. *Journal of Applied Physics*, 103(7).

Yang, W., Lopez, P. J., and Rosengarten, G. (2011). Diatoms: Self assembled silica nanostructures, and templates for bio/chemical sensors and biomimetic membranes. *Analyst*, 136(1):42–53.

Yu, M., Falconer, J., and Noble, R. (2008). Characterizing nonzeolitic-pores in mfi membranes. *Industrial and Engineering Chemistry Research*, 47(11):3943–3948.

Zarzar, L. D., Sresht, V., Sletten, E. M., Kalow, J. A., Blankschtein, D., and Swager, T. M. (2015). Dynamically reconfigurable complex emulsions via tunable interfacial tensions. *Nature*, 518(7540):520–524.

Zhang, B., Ren, T.-R., Song, B.-A., and Wang, Q.-X. (2013). Fabrication of monodisperse silica microspheres using synechocystis cell as a template. *Materials Chemistry and Physics*, 138(2):762 – 766.

Zhang, C., Khoshmanesh, K., Mitchell, A., and Kalantar-zadeh, K. (2010). Dielectrophoresis for manipulation of micro/nano particles in microfluidic systems. *Analytical and Bioanalytical Chemistry*, 396(1):401–420.

Appendix A

Table A.1 Concentration ranges of critical ionic species in areas known for phytoplankton growth at depths within the mixed layer.

	Silicate	Phosphate	Nitrite	Nitrate	Ammonium	Notes
Mitchell et al. (2013)	0.4–1.7	0–0.9	0.11–0.35	1–7.8	-	($\mu molL^{-1}$) Direct samples measured over a horizontal area 45x45cm
Mojica et al. (2015)	-	0.01–0.028	0.06–0.1		0.05–0.09	($\mu molL^{-1}$) Direct measurements taken in the Northeast Atlantic Ocean
Reid Jr (1965)	-	0–3.25	-	-	-	($\mu molL^{-1}$) TransPacific profile from Japan to North America.
Smayda (1998)	-	0.11	-	0.4	-	($\mu molL^{-1}$) Mean annual water column concentrations in lower Narragansett Bay
Conkright et al. (2002)	1–80	0–2.6	-	1–34	-	($\mu molL^{-1}$) Global annual mean sea surface concentrations

Table A.2 General dimensions of the architecture of the frustules of the two centric diatom species (*Coscinodiscus sp.* and *Thalassiosira eccentrica*) (Losic et al. (2009, 2006)).

Centric diatom species	Structures	Single pore evaluation			Porosity (%)
		Minimum diameter (nm)	Maximum diameter (nm)	Length/ Thickness (nm)	
Coscinodiscus sp.	Entire frustule (varies between cells)	60	150	1000	-
	Cribellum pores (External)	45 ± 9	45 ± 9	≈ 50	7.5 ± 1.2
	Cribrum pores (Mid)	192 ± 35	192 ± 35	≈ 200	25.2 ± 2.5
	Foramen pores (Internal)	1150 ± 130	1150 ± 130	-	35 ± 3
	Aereoli	2000	2000	≈ 800	Same as foramen
	Girdle band pores	100	250	500 each repeating unit	32 ± 5
Thalassiosira eccentrica	Entire frustule (varies between cells)	30	50	1000	-
	Internal pores	43 ± 6	43 ± 6	-	10 ± 2.5
	Foramen pores (Internal)	770 ± 38	770 ± 38	-	35 ± 3
	Aereoli	1000	1000	700	Same as Foramen
	Girdle band pores	100	250	500 each repeating unit	-

Table A.3 Comparison of drift ratchet parameters studied by previous researchers to the characteristics of a girdle band pore.

Source	Kettner et al. (2000)	Matthias and Muller (2003)	Brenk et al. (2008)	Mathwig et al. (2011b)	Girdle band pores
Max. pore diameter (μm)	≈ 4	4.8	–	3.8	0.25
Min. pore diameter (μm)	≈ 1.5	2.5	1.0	2.0	0.1
Particle diameter (μm)	$0.2-1.2$	0.32 and 0.1	0.6	0.1, 0.3 and $0.5\mu m$	1×10^{-3}
Length of single repeating unit	6	8.4	–	$10-12\mu m$	0.5
Amplitude of fluid oscillation	$3-15\mu m$	$0-4kPa$	$11kPa$	$0.4-6kPa$	Unknown
Frequency of fluid oscillation (Hz)	40 and 100	40	7000	40	Unknown

Appendix B

Table B.1 Parameters used for the different scaling cases for 1x amplitude

Pore scale	200%	150%	100%	80%	60%	40%	20%
$d_{min}(\mu\text{m})$	3.05	2.29	1.52	1.22	0.915	0.61	0.305
$D_{th}(m^2s^{-1})$	4.8×10^{-12}	2.7×10^{-12}	1.2×10^{-12}	7.7×10^{-13}	4.3×10^{-13}	1.9×10^{-13}	4.8×10^{-14}
$a(\mu\text{m})$	1.4	1.05	0.7	0.56	0.42	0.28	0.14
$L(\mu\text{m})$	12	9	6	4.8	3.6	2.4	1.2
$L^{-1}(\mu m^{-1})$	0.083	0.11	0.17	0.21	0.28	0.42	0.83
$v_{max}(\mu ms^{-1})$	5316	3988	2657	2126	1595	1063	532
Re	3.2×10^{-2}	1.8×10^{-2}	7.9×10^{-3}	5.1×10^{-3}	2.9×10^{-3}	1.3×10^{-3}	3.2×10^{-4}
α	0.46	0.46	0.46	0.46	0.46	0.46	0.46
Re_p	6.8×10^{-3}	3.8×10^{-3}	1.7×10^{-3}	1.1×10^{-3}	6.1×10^{-4}	2.8×10^{-4}	6.8×10^{-5}
Pe	13329	13329	13329	13329	13329	13329	13329
St	0.023	0.023	0.023	0.023	0.023	0.023	0.023
$T(s)$	0.025	0.025	0.025	0.025	0.025	0.025	0.025
β	11.1	11.1	11.1	11.1	11.1	11.1	11.1

Appendix C

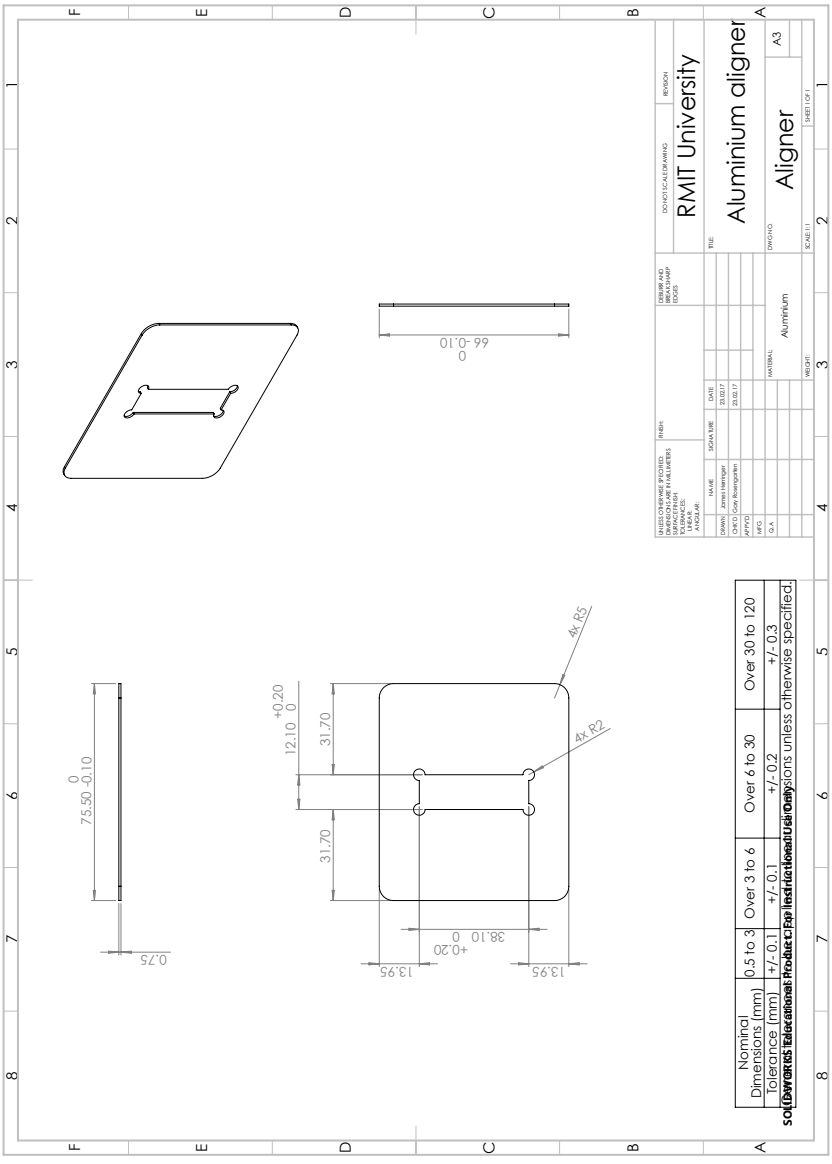
RMIT University
Aluminium aligner
Aligner
A3
Aluminium
4x R5
4x R2
31.70
31.70
12.10 +0.20 0
75.50 -0.10 0
66 -0.10 0
38.10 +0.20 0
13.95
13.95
0.75
Nominal Dimensions (mm) | 0.5 to 3 | Over 3 to 6 | Over 6 to 30 | Over 30 to 120
Tolerance (mm) | +/- 0.1 | +/- 0.1 | +/- 0.2 | +/- 0.3
Do not scale drawing
Remove all burrs and sharp edges
Unless otherwise specified:
Dimensions are in millimeters
Surface finish:
Tolerances:
Linear:
Angular:
Material:
Finish:
Name
Date
Drawn
Checked
Eng Approval
Mfg Approval
Comments:
Title:
Dwg No.
Size
Weight:
Sheet 1 of 1

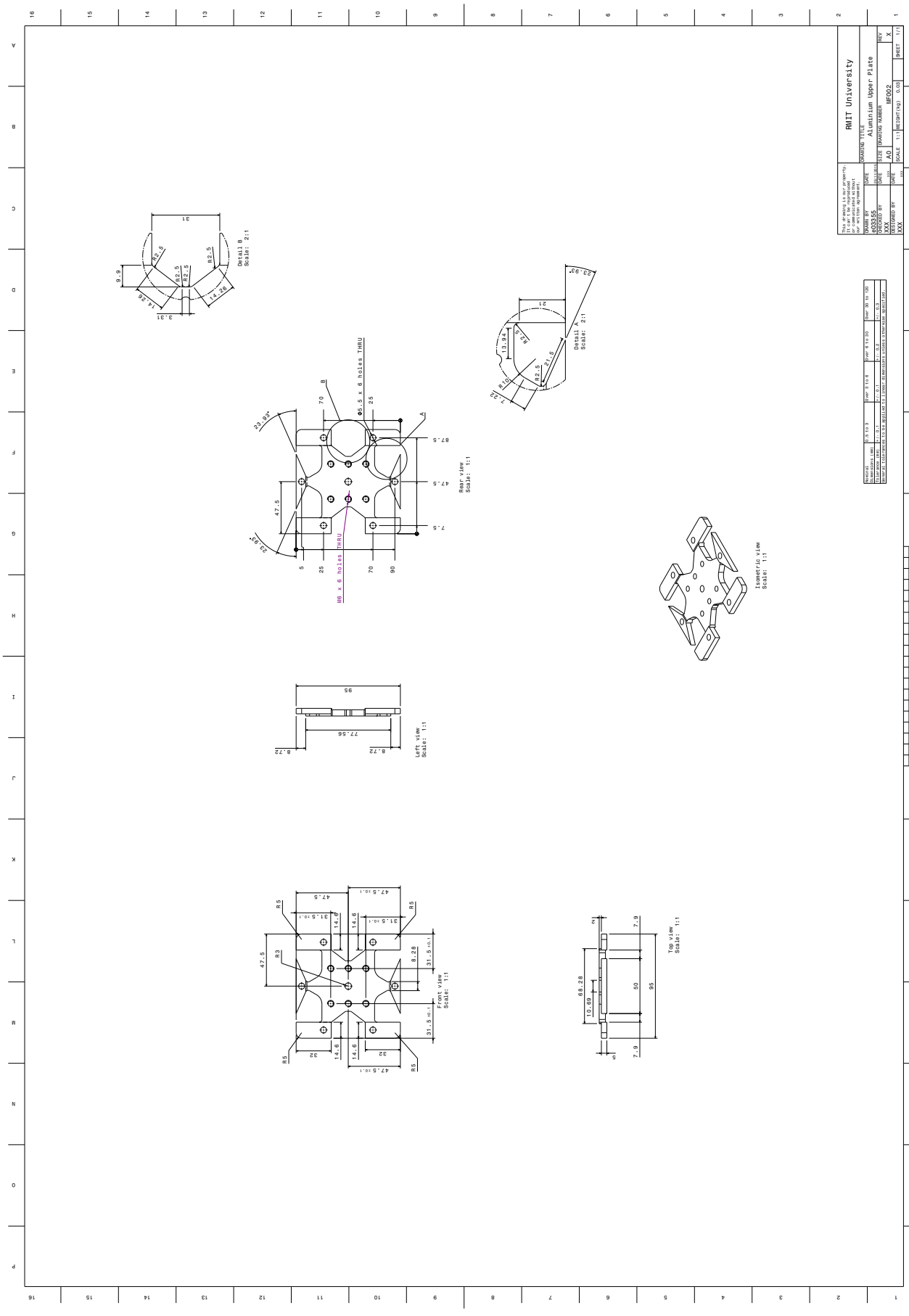
RMIT University
Aluminium Upper Plate
DF002
A0
Detail B
Scale: 2:1
Detail A
Scale: 2:1
Rear view
Scale: 1:1
Left view
Scale: 1:1
Front view
Scale: 1:1
Top view
Scale: 1:1
Isometric view
Scale: 1:1
M6 x 6 holes THRU

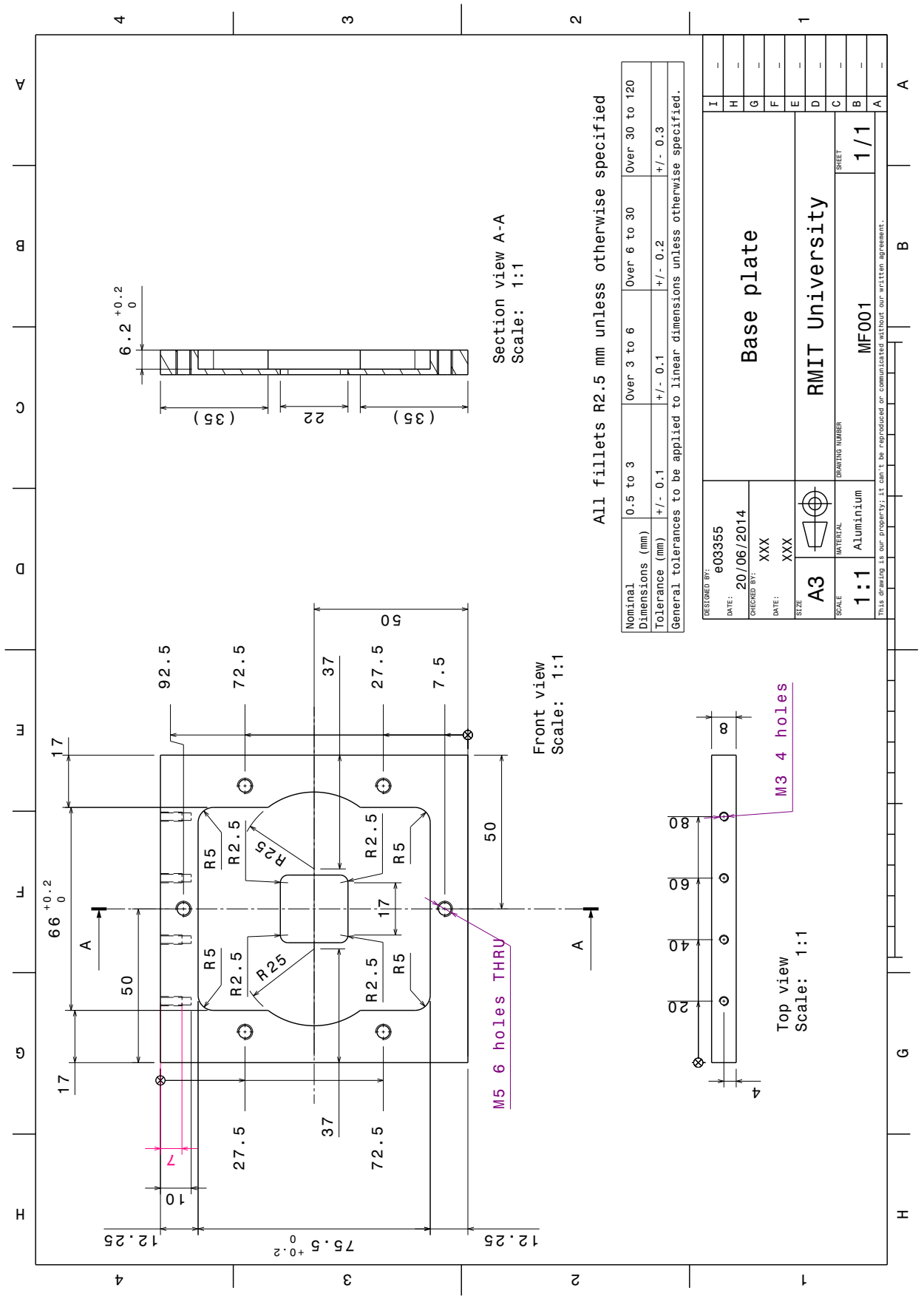
All fillets R2.5 mm unless otherwise specified
Nominal Dimensions (mm) | 0.5 to 3 | Over 3 to 6 | Over 6 to 30 | Over 30 to 120
Tolerance (mm) | +/- 0.1 | +/- 0.1 | +/- 0.2 | +/- 0.3
General tolerances to be applied to linear dimensions unless otherwise specified.
Section view A-A
Scale: 1:1
Front view
Scale: 1:1
Top view
Scale: 1:1
M5 6 holes THRU
M3 4 holes
Base plate
RMIT University
MF001
A3
1:1
Aluminium
1/1
e03355
20/06/2014
XXX
XXX
This drawing is our property; it can't be reproduced or communicated without our written agreement.